THE UNIVERSITY OF CALGARY

VESSEL-EDGE CONTRAST IN MAGNETIC RESONANCE ANGIOGRAPHY

by

H. Mathura

A THESIS

SUBMITTED TO THE FACULTY OF GRADUATE STUDIES IN

PARTIAL FULFILLMENT OF THE REQUIREMENTS FOR

THE DEGREE OF MASTER OF SCIENCE

DEPARTMENT OF PHYSICS AND ASTRONOMY

CALGARY ALBERTA

January, 1995

THE UNIVERSITY OF CALGARY

FACULTY OF GRADUATE STUDIES

The undersigned certify that they have read, and recommend to the Faculty of Graduate Studies for acceptance, a thesis entitled, "Vessel-Edge contrast in Magnetic Resonance Angiography," submitted by H. Mathura in partial fulfillment of the requirements for the degree of Master of Science.

Supervisor, Dr. L. J. Hahn

Department of Radiological Sciences and Diagnostic Imaging, Foothills Hospital

---

Dr. C. J. Bland

Department of Physics and Astronomy

Dr. A. P. Crawley

Department of Radiological Sciences and Diagnostic Imaging, Foothills Hospital

---

Dr. M.R. Smith

Department of Electrical and Computer Engineering

9 January 95

Date

ABSTRACT

Clinical techniques used to image flow in magnetic resonance angiography (MRA) rely on time-of-flight (TOF) or phase contrast (PC) methods [5]. However due to the presences of slow moving spins and large velocity gradients at the vessel boundary, both these methods show a decrease in signal, resulting in over-estimation of any stenosis present. As the goal of the clinical examination is to detect and measure stenoses, the use of MRA in the diagnosis of vascular disease is limited.

The aim of this project is to optimize the MR contrast at the vessel boundary and compare the performance of the TOF and PC (complex subtraction (CS) and phase subtraction (PS)) methods. This was performed for parabolic flow perpendicular to the slice, using a spoiled flow compensated gradient echo sequence for TOF with a bipolar gradient added for PC, an echo time (TE) of 25 ms and a repetition time (TR) of 50 ms.

Computer simulations of the vessel boundary contrast for a 2D slice were performed and the simulation results for the contrast-to-noise ratio (CNR), the optimal tip angle and optimal flow encode phase were compared to data obtained experimentally using a flow phantom (images acquired on a 1.5 T magnet). The velocity range examined was 0 - 100 cm/s (average velocity) in the simulations, and 2 - 81 cm/s in the experiments.

Results obtained showed that at high velocities TOF performed better than CS, whereas at low velocities the reverse was true. Overall the best contrast was obtained with PS. The agreement of the experimental results with the simulated optimal CNR was good.

Experimentally the mean optimal flow encoding phase of the peak velocity obtained for CS was $150^0 \pm 17^0$, while for PS it was $310^0 \pm 18^0$. The optimal experimental tip angle was determined to be around 112^0 for TOF, 115^0 for CS and 118^0

for PS for the upper range of the average velocity ($v > 30$ cm/s). The disagreement between the experimental and the simulated results is attributed to the systematic error from the steady state effect on the slice profile as the $TR >> T_1$.

ACKNOWLEDGEMENTS

I take this opportunity to acknowledge the input and guidance of Dr. A. P. Crawley on this project.

I would like thank:

Dr. L. J. Hahn, my interim supervisor, for his help and support. The Swerhones-Damini and David for programming tips as well as for personal support in general throughout this project.

The staff of the MRI Centre at the Foothills Hospital (Donna, Ian, Jean, Pierre, Rick, Theresa, Tammy, Wanda and the others) for allowing me to have the graveyard shift.

Ken Botts, the GE support engineer for his prompt assistance with some of the technical problems that occurred on the Signa and Byron Draudson for his assistance in problems that occurred in the computer systems network.

Ingrid Koslowsky for the loan of the vacuum filtering equipment as well as her assistance in the purchasing of glycerol for the experiments.

The staff of the T.B.C.C. machine shop for helping in my vain attempts at trying to get the UHDC flow simulator to work.

K. V. Slater for the use of ladders to perform the gravity feed experiments.

Dr. C. J. Bland for assistance in obtaining an extension to allow this project to be completed.

Special thanks to Evelyn Dolen, for so many countless things - driving me around to get items like tubing, clamps, etc., transporting the ladders to and from the hospital and for many comforting pots of tea.

I dedicate this thesis to

Basso, Winston, Ric and Tricia

with love and thanks.

TABLE OF CONTENTS

LIST OF FIGURES

CHAPTER 1

INTRODUCTION

1.1 Development of Magnetic Resonance Imaging

The phenomenon of nuclear magnetic resonance (NMR) was independently observed from hydrogen nuclei by Bloch and co-workers at Stanford and by Purcell at Harvard in 1946 [42]. NMR quickly became an invaluable tool in the area of spectroscopy. In 1974, Lauterbur produced the first 2D proton magnetic resonance image of a live animal. This was the starting point which enabled the production of the first human images by Damadian in 1977 [17]. All this work culminated in a branch of NMR known as magnet resonance imaging (MRI) which was introduced clinically in 1981.

With its high soft tissue contrast and multiplanar imaging capabilities, MRI has found a place in diagnostic imaging, where it has proven itself superior to other imaging modalities in some areas such as in the diagnosis of disorders of the central nervous system. MRI is non-invasive and this, combined with its flexibility, offsets the disadvantages of acoustic noise due to varying gradients; potential dangers of electromagnetic radiation to biological tissues, such as the heating effect of the radio frequency pulse [42]; and high cost. During the last two decades or so its use has grown as research and new technology have overcome some its limitations, while clinical investigations have demonstrated the types of diagnostic information that can be obtained from the images.

The clinical goal in diagnostic angiography is to detect and quantify any vessel narrowing present. MRI offers the possibility of a non-invasive method of vascular imaging since it is inherently sensitive to flow. A number of imaging techniques [38, 42] have been proposed in this area, some of which are in use clinically. Currently the

techniques used to image flow exploit two processes: one is the enhancement of the longitudinal magnetization from blood flowing into the image slice and is referred to as time- of-flight (TOF), the other is the phase accrued by protons as they flow along an applied magnetic field gradient, which is referred to as phase-contrast (PC). The images produced are very sensitive to flow but are not specific enough as they tend to over-estimate any decreases in the inner diameter of the vessel present. Therefore the current use of magnetic resonance (MR) in angiography is limited.

1.2 Objective of thesis

The aim of this thesis is to optimize the MR contrast at the vessel boundary obtainable from currently available techniques (the TOF and PC methods). Computer simulations of the boundary contrast for a vessel were performed, with parabolic flow perpendicular to the imaged slice. The results are compared to experimental measurements obtained from a flow phantom. The overall goal is to compare the performance of the two methods and in so doing provide a general range of the parameters that should be used to generate an MR image in which the boundary contrast is optimized. The boundary contrast is examined for a range of velocities that are of interest for in-vivo imaging.

1.3 Overview of thesis

Presented in chapter 2 of this work are the basic principles of NMR as well as an introduction to MRI. This is mainly concerned with the way in which an image is generated, rather than a discussion of instrumentation or alternative image reconstruction techniques. A comparative review of the various diagnostic modalities

that are used in the field of head and neck angiography is discussed in chapter 3. Also presented is a synopsis of the importance of angiography, which shows why good vessel boundary contrast is necessary in magnetic resonance angiography (MRA). An additional purpose of this chapter is to indicate the uses of the different methods available in MRA and in so doing demonstrate more of the clinical potential of MRI.

The physical basis underlying the TOF and PC methods as well as the pulse sequences that are utilized in MRA is given in the chapter 4. The computer simulation model as well as a description of the algorithms are also provided. The experimental setup, data analysis and results are discussed in chapter 5. It should be noted that this investigation pertains to a 2D slice, but can also be applied to a 3D volume. The results are summarized in the last chapter, where some conclusions are drawn from the present work and future work is proposed.

CHAPTER 2

MAGNETIC RESONANCE IMAGING

The theory of NMR is described in sections 2.1 and 2.2 of this chapter. A detailed description of the theory can be found in any one of the following references: Abragam, 1961 [1], Dixon and Ekstrand, 1982 [11], Farrar and Becker, 1971 [20] and Stark and Bradley, 1992 [42].

Provided in section 2.3 is a condensed review of the principles of MRI, complied from King and Moran, 1984 [27] and Stark and Bradley, 1992 [42]. Some aspects of MRI that are of concern to this thesis are described in sections 2.4 and 2.6. The source materials for these sections are Stark and Bradley, 1992 [42], Edelman and Hessellink, 1990 [17] and the Signa Applications guide, Volume 2, 1990 [45].

2.1 Basic NMR Theory

NMR is a phenomenon exhibited by nuclei that possess a magnetic moment $\vec{\mu}$ and angular momentum $\vec{J}$, by virtue of having an odd number of protons and/or neutrons. These vectors are related through

$$\vec{\mu} = \gamma \vec{J} = \gamma \hbar \vec{I} = \frac{\gamma h}{2\pi} \vec{I} \qquad 2.1$$

where $\vec{I}$ is the dimensionless angular momentum operator, h is Planck's constant and γ is the gyromagnetic ratio.

If the nucleus is placed in a static magnetic field $\vec{B} = (0,0,B_0)$, the energy of the magnetic moment is given by the Hamiltonian

$$H = -\vec{\mu} \bullet \vec{B}_0 = -\gamma \hbar B_0 I_z \qquad 2.2$$

Since I_z is quantized, this results in 2I+1 eigenvalues of the Hamiltonian. These are given by

$$E_m = -\gamma \hbar B_0 m \qquad 2.3$$

with m = -I, -I+1, ..., I. The energy difference ΔE between adjacent states is given by

$$\Delta E = \gamma \hbar B_0 \qquad 2.4$$

In NMR experiments, transitions between adjacent states are induced by the application of a suitable alternating magnetic field or radio frequency (rf), $\vec{B}_1 = B_1 \cos \omega t \, \hat{x}$, applied perpendicular to $\vec{B}_0$. Hence a perturbation term

$$H' = -\gamma \hbar B_1 I_x \cos \omega t \qquad 2.5$$

is added to eq. 2.2. As ω approaches $\Delta E/\hbar$, state transitions occur due to exchange of energy between the spins and the perturbing field. Hence from eq. 2.4, the frequency at which these transitions occur is given by $\omega = \omega_0 = \gamma B_0$, where ω_0 is called the Larmor angular frequency.

In the absence of a perturbing field, the Larmor frequency is the frequency at which the magnetic moment precesses about $\vec{B}_0$. In classical terms this precession can be thought of as being caused by a torque exerted by the static field.

In an NMR experiment, the observed signal is a composite of the contributions of an ensemble of nuclei. At thermal equilibrium, these nuclei are distributed among the various energy levels (see eq. 2.3), according to a Boltzmann distribution. The Boltzmann energy distribution favours the lower energy state. Consider protons as an example. In the lower energy state (m = +1/2), more of the spins are aligned with the field than in the upper energy state (m = -1/2) where the spins are oriented in the opposite direction. Hence there exists a net macroscopic magnetization, $\vec{M} = \sum_{i=1}^{N} \vec{\mu}_i$ parallel to $\vec{B}_0$. At thermal equilibrium $\vec{M}$ has a magnitude M_0 (see fig. 2.1).

In the laboratory (or fixed) frame, the motion of $\vec{M}$ in the presence of an applied alternating magnetic field can be described in terms of the Bloch equations.

$$\left[\frac{d\vec{M}}{dt}\right]_{fixed} = \gamma \vec{M} \times \vec{B} \qquad 2.6$$

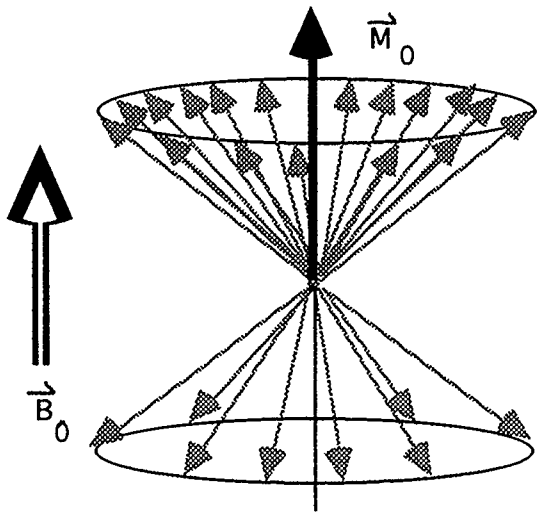

Figure 2.1 Macroscopic magnetization M_0 produced from the alignment of spins in the static field B_0.

where $\vec{B} = (B_x, B_y, B_z)$. The components of $\vec{B}$ in Cartesian co-ordinates are :

$$B_x = B_1 \cos\omega t, \quad B_y = - B_1 \sin \omega t, \quad B_z = B_0 \qquad 2.7$$

On substitution of eq. 2.7 into eq. 2.6, the differential eq. becomes

$$\frac{dM_x}{dt} = \gamma \left[M_y B_0 + M_z B_1 \sin \omega t \right] - \frac{M_x}{T_2} \qquad 2.8\ a$$

$$\frac{dM_y}{dt} = \gamma \left[M_z B_1 \cos \omega t - M_x B_0 \right] - \frac{M_y}{T_2} \qquad 2.8\ b$$

$$\frac{dM_z}{dt} = - \gamma \left[M_x B_1 \sin \omega t + M_y B_1 \cos \omega t \right] - \frac{M_z - M_0}{T_1} \qquad 2.8\ c$$

where the additional terms containing parameters T_1 and T_2 are added to account for relaxation effects (described in section 2.2).

In the study of the magnetization, $\vec{M}$, it is convenient to use a reference co-ordinate system that rotates about $\vec{B}_0$ at the same frequency as the magnetization. This frame is called the rotating frame with axes (x', y', z'= z). In the rotating frame the rate of change of $\vec{M}$ with time becomes

$$\left[\frac{d\vec{M}}{dt} \right]_{rot} = \left[\frac{d\vec{M}}{dt} \right]_{fixed} - \left[\vec{\omega} \times \vec{M} \right] \qquad 2.9$$

which on rearrangement and substitution of equation 2.6 is

$$\left[\frac{d\vec{M}}{dt} \right]_{rot} = \gamma \vec{M} \times \left[\vec{B} + \frac{\vec{\omega}}{\gamma} \right] \qquad 2.10\ a$$

In the presence of a $\vec{B}_1$ field, it becomes

$$\left[\frac{d\vec{M}}{dt} \right]_{rot} = \gamma \vec{M} \times \vec{B}_{eff} \qquad 2.10\ b$$

where

$$\vec{B}_{eff} = \vec{B}_0 + \frac{\vec{\omega}}{\gamma} + \vec{B}_1 \qquad 2.10\,c$$

From eq. 2.10b it is seen that in the rotating frame the magnetization precesses about $\vec{B}_{eff}$.

In the rotating frame if $\vec{B}_1 = 0$ and $\vec{B}_0 = -\frac{\vec{\omega}}{\gamma}$, then $\vec{B}_{eff}$ reduces to zero. In this case, the magnetization $\vec{M}$ is invariant in the frame. In the presence of $\vec{B}_1$, if $\vec{B}_0 = -\frac{\vec{\omega}}{\gamma}$ then $\vec{B}_{eff} = \vec{B}_1$. Therefore, from the Larmor relationship, $\vec{M}$ will rotate about the $\vec{B}_1$ field at angular velocity $\vec{\omega} = -\gamma\,\vec{B}_1$.

If the field $\vec{B}_1$ is applied in the form of a pulse of duration t_p, the magnetization will be tipped through an angle θ given by

$$\theta = \gamma\, B_1\, t_p \qquad 2.11$$

away from the z-axis. Assume that θ is such that $\vec{M}$ has non-zero components in the x'y' plane i.e. the transverse plane. Viewed in the stationary frame, the transverse magnetization is rotating in the xy plane. An EMF will therefore be induced in a receiver coil placed perpendicular to the xy plane, and will be proportional to the magnitude of the xy-component of the macroscopic magnetization $\vec{M}$ (see fig. 2.2). This signal decreases in time as the spins return to thermal equilibrium corresponding to the regrowth of M_z.

2.2 Relaxation Theory

The rate of relaxation of the macroscopic magnetization is due to a combination of two relaxation processes and hence is divided into two relaxation rates, $1/T_1$ and $1/T_2$.

T_1 processes arise from the absorption and stimulated emission of energy from spins during state transitions. Conservation of energy requires the surrounding medium or lattice to undergo a compensating change, hence T_1 is called the spin-lattice

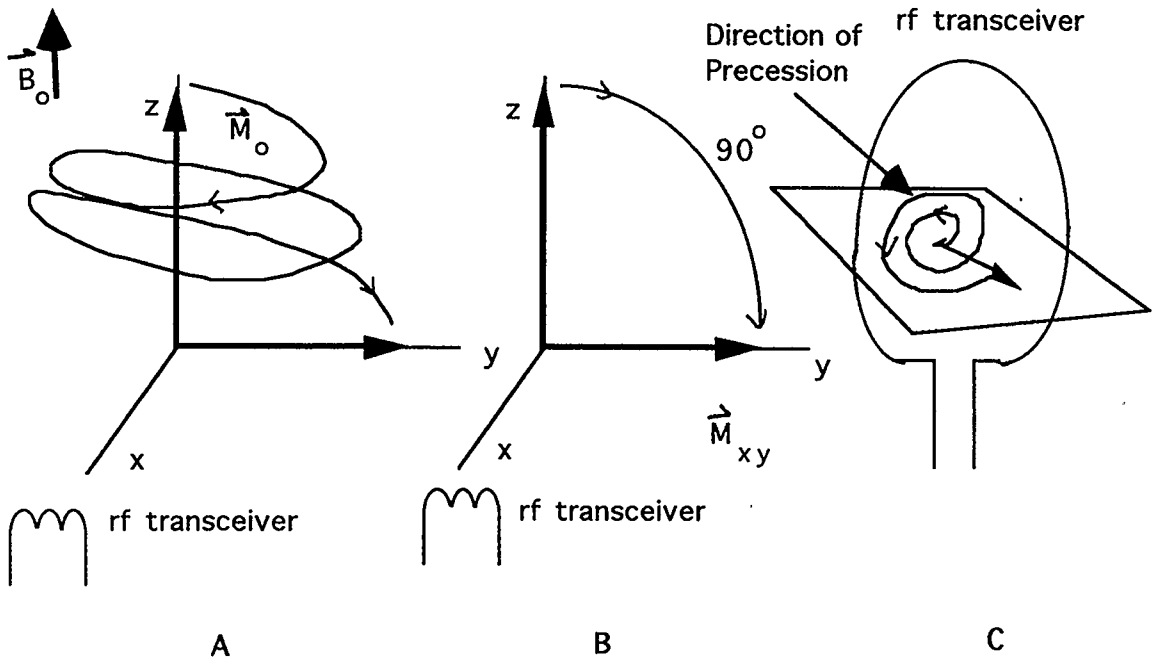

Figure 2.2 Production of MR signal

A. Application of the rf pulse to the macroscopic magnetization, viewed in the laboratory frame.

B. View of the magnetization in the rotating frame.

C. An EMF is induced in the RF receiver coil.during free precession of the magnetization in the xy plane

relaxation time, and it is a measure of the average lifetime of a spin state. These energy exchanges occur in order to bring the system to a state of thermal equilibrium, which was upset by the application of the perturbing rf field. Transitions result predominantly from dipole-dipole interactions for a spin 1/2 system. In the neighbourhood of a particular nucleus, thermal molecular motion causes rapidly fluctuating local magnetic fields. T_1 relaxation is responsible for the regrowth of the macroscopic magnetization along the z' axis, (the term $(M_Z - M_0/T_1)$ in eq. 2.8c). Hence it is also referred to as the longitudinal relaxation time.

In addition to energy exchange with the lattice, there are also interactions that occur between spins. Each nucleus experiences a local field, caused by the presence of neighbouring spins, which adds or subtracts from the static field causing variation in the Larmor frequency. Nuclei in stronger fields will have faster precession rates, i.e. a larger phase gain, compared to those in weaker fields. There is therefore a net dephasing of the xy-component of the magnetization. This process is described by the relaxation time T_2, the spin-spin or transverse relaxation time. T_2 is defined as the time required for the xy magnetization component to be reduced by a factor of e. If the static field is inhomogenous then the resulting T_2 is an apparent one, due to additional contributions to the dephasing from the static field, referred to as T_2^*.

To cancel the effect of an inhomogenous static field on T_2, a 90^0-τ-180^0 rf pulse sequence is applied to the sample, where τ is the wait time between the application of the 90^0 rf and the 180^0 rf. Application of the 90^0 rf pulse tips the longitudinal magnetization into the xy plane (see fig. 2.3). During the time τ the transverse magnetization dephases with an apparent relaxation time of T_2^*. The 180^0 rf pulse is applied next and reverses the phases of the spins. Hence the faster components of the dephasing magnetization now trail the slower components. This process ensures that the majority of spins are in phase at time 2τ, creating a spin echo (SE), when the faster

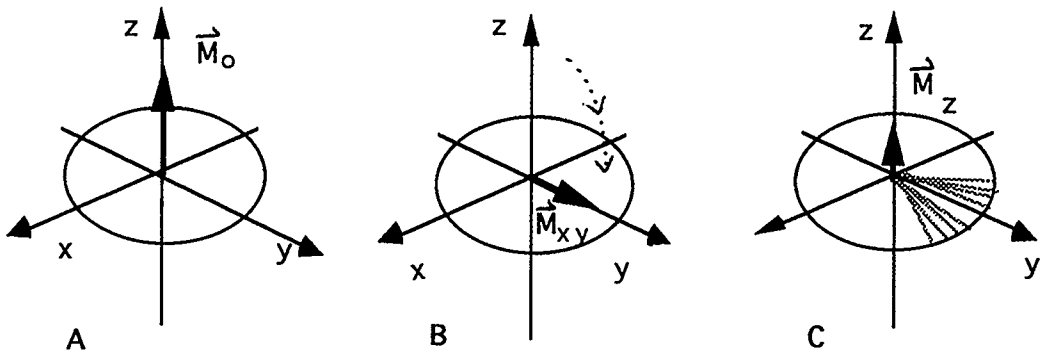

Figure 2.3 Magnetization behavior for a spin-echo pulse sequence.

A. Macroscopic magnetization, M_0, present prior to application of 90^0 rf pulse.

B. The 90^0 pulse nutates M_0 into the xy plane, longitudinal magnetization transformed into transverse magnetization.

C. Transverse magnetization dephases due to irreversible T_2 decay and other reversible decay processes.

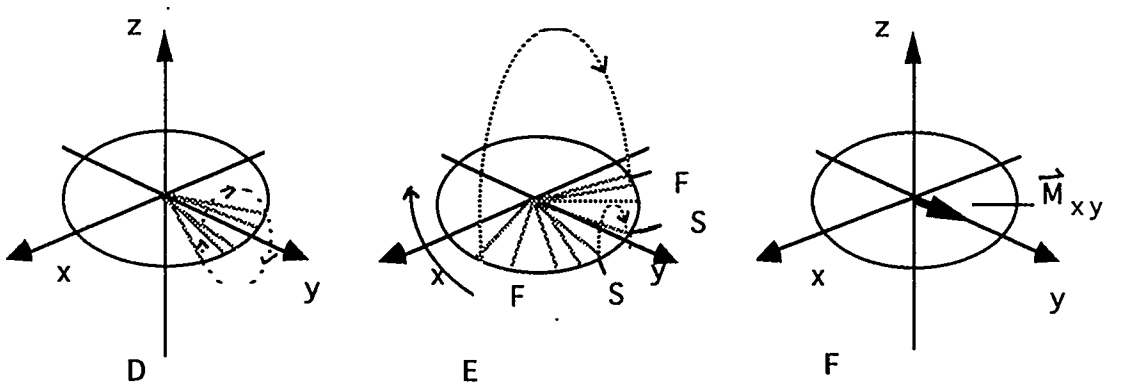

D. A 180^0 pulse is applied at time $t=\tau$ along the y-axis, which reverses the direction of all the components of the magnetization.

E. The effect of the 180^0 pulse is that the faster spins (F) now lag the slower spins, so rephasing occurs as the faster spins catch up.

F. The echo forms at $t = 2\tau$ - spins are in phase at this time.

spins catch up with the slower ones. At this time the dephasing caused by the magnetic field inhomogeneities is canceled.

Both T_1 and T_2 are dependent on the physical phase and molecular structure of the sample. Fig. 2.4 shows the dependence of T_1 and T_2 on viscosity. The T_1 curve increases at low viscosities because rapid tumbling motion decreases the chances of transitions. State transitions are induced if the frequency of random fluctuations in the local magnetic field match the resonance frequency of neighbouring nuclei. T_1 also increases at high viscosities as the slower motion of the nuclei reduces the number of possible interactions that they can make. The curve has a minimum at some medium viscosity.

T_2 interactions require that two nuclei be in close proximity long enough that their local fields interact to cause dephasing. Therefore T_2 decreases as the viscosity increases.

2.3 Magnetic Resonance Imaging Theory

Imaging requires a means of locating and differentiating the spins from different spatial positions, and a fast and efficient method of data accumulation and image reconstruction. For the resultant image to be useful, it must have adequate tissue contrast.

The body possesses a number of nuclear species that can exhibit resonance. The hydrogen nucleus is most commonly used in imaging, since it is present in the highest abundance in the body (water comprises approximately 85% of the human body by volume). Hence the bandwidth of the exciting rf pulse is usually centered on the resonance frequency of water protons.

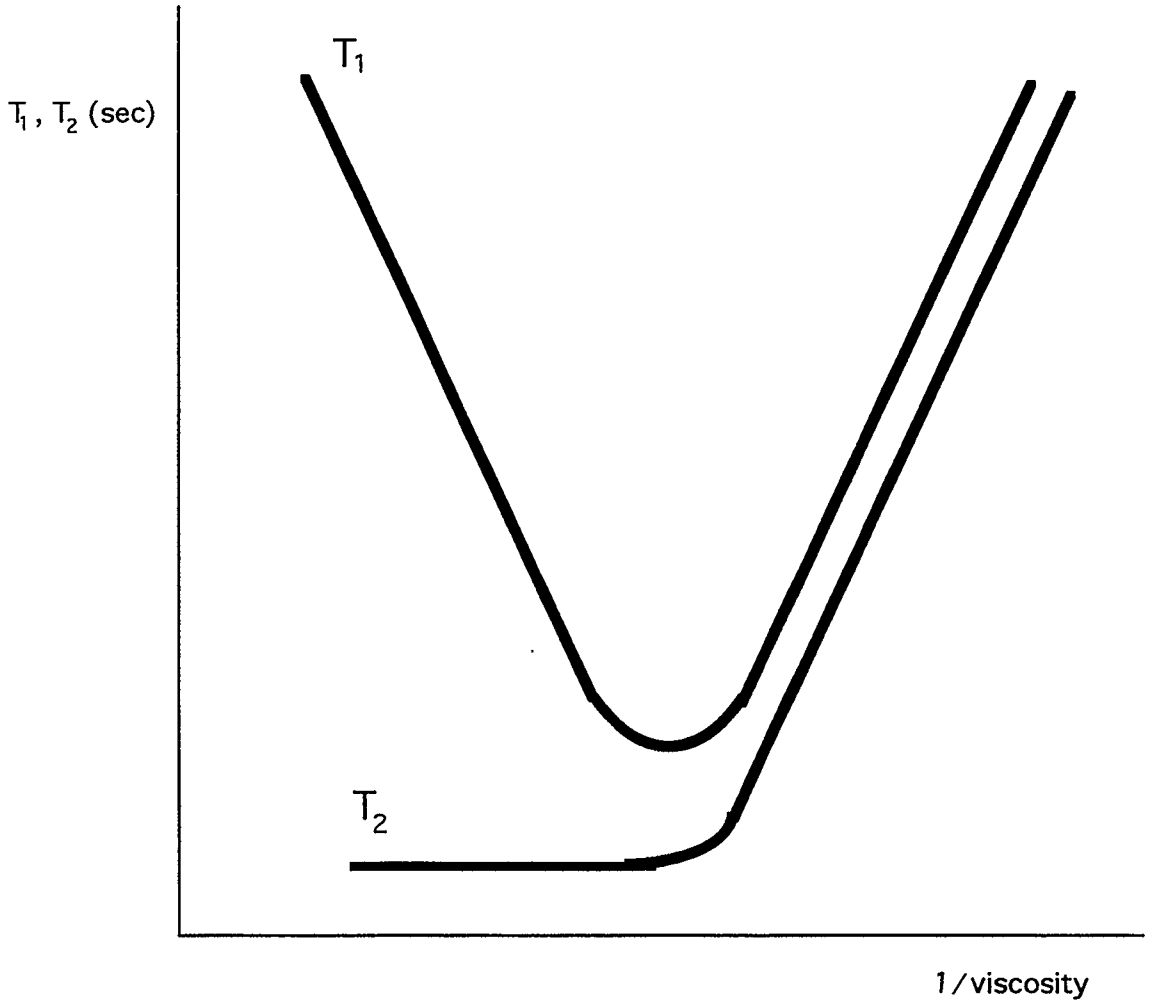

Figure 2.4 Relaxation time T_1, T_2 (sec) vs. 1/viscosity.

2.3.1 Spatial Localization

The angular frequency at which the nucleus rotates is directly related to the strength of the static magnetic field by the Larmor relationship. Hence spatial variation of the field would enable position determination of the nuclei, which is accomplished by the superposition of three orthogonal gradient fields, usually applied separately, on to the static field. Following the Cartesian convention, they are referred to as the G_x, G_y and the G_z imaging gradients. Their magnetic field contributions are directed along the same axis as the static field, whereas the Cartesian subscripts refer to the direction of the change in field strength. They are defined by the following equations

$$G_x = \frac{\partial B_0}{\partial x}, \quad G_y = \frac{\partial B_0}{\partial y}, \quad G_z = \frac{\partial B_0}{\partial z}. \qquad 2.12$$

where the physical axis of the static field can be defined to be in the x, y or z direction. In this thesis the direction of the static field is defined to be along the z direction.

2.3.1.1 Slice Selection

Slice selection is accomplished by the application of a field gradient, the slice select gradient, in the z direction perpendicular to the imaging plane so that

$$B(z) = B_0 + G_z z \qquad 2.13$$

Simultaneously an rf pulse is also applied. The application of the slice selective gradient (G_z) varies the Larmor frequencies of the nuclei as a function of position in the z direction. The rf pulse is shaped to contain within it a range of frequencies ($\omega_0 \pm \Delta\omega$), therefore it excites only the nuclei rotating at frequencies to be found within that bandwidth. The slice thickness is determined by the bandwidth of the frequency selective rf pulse and the amplitude of the slice selective G_z gradient.

However, in the presence of a field gradient there is an accumulation of phase shift given by

$$\varphi = \gamma G_z z t \qquad 2.14$$

where t corresponds to the second half of the rf pulse duration. To compensate for the additional phase imparted to the spins a negative G_z gradient is applied to rephase the spins (see fig. 2.5).

2.3.1.2 Phase Encoding

Phase encoding is performed by using a field gradient applied in the y direction, G_y, to produce a magnetic field

$$B(y) = B_0 + G_y y \qquad 2.15$$

Phase encoding is used to resolve the locations of the spins in the y direction.

An application of the G_y gradient, or phase encoding gradient, causes spins at different y locations to precess at different rates. After the gradient is turned off, the spins will again resonate at the same frequency, but will all have different phases.

To acquire a complete image the pulse sequence is repeated a number of times, and for each repetition, the phase encoding gradient is incremented by a fixed amount (see fig. 2.5). The explanation for this is given in section 2.3.2.

2.3.1.3 Frequency Encoding

The MR signal is collected during the application of a third field gradient, the G_x gradient, which is referred to as the read gradient. Position differentiation of the spins is accomplished because spins at different x locations will be rotating at different rates, due to the presence of the gradient. Therefore, the received signal is composed of a number of different frequencies. These frequencies correspond to the spatial locations of the spins along the x direction, hence the gradient is also called the frequency encoding gradient. The phase and frequency at time t of a spin at (x, y) is given by

$$\varphi_y = \gamma G_y t_y y \qquad 2.16\ a$$

$$\varphi_x = \gamma G_x t x \qquad 2.16\ b$$

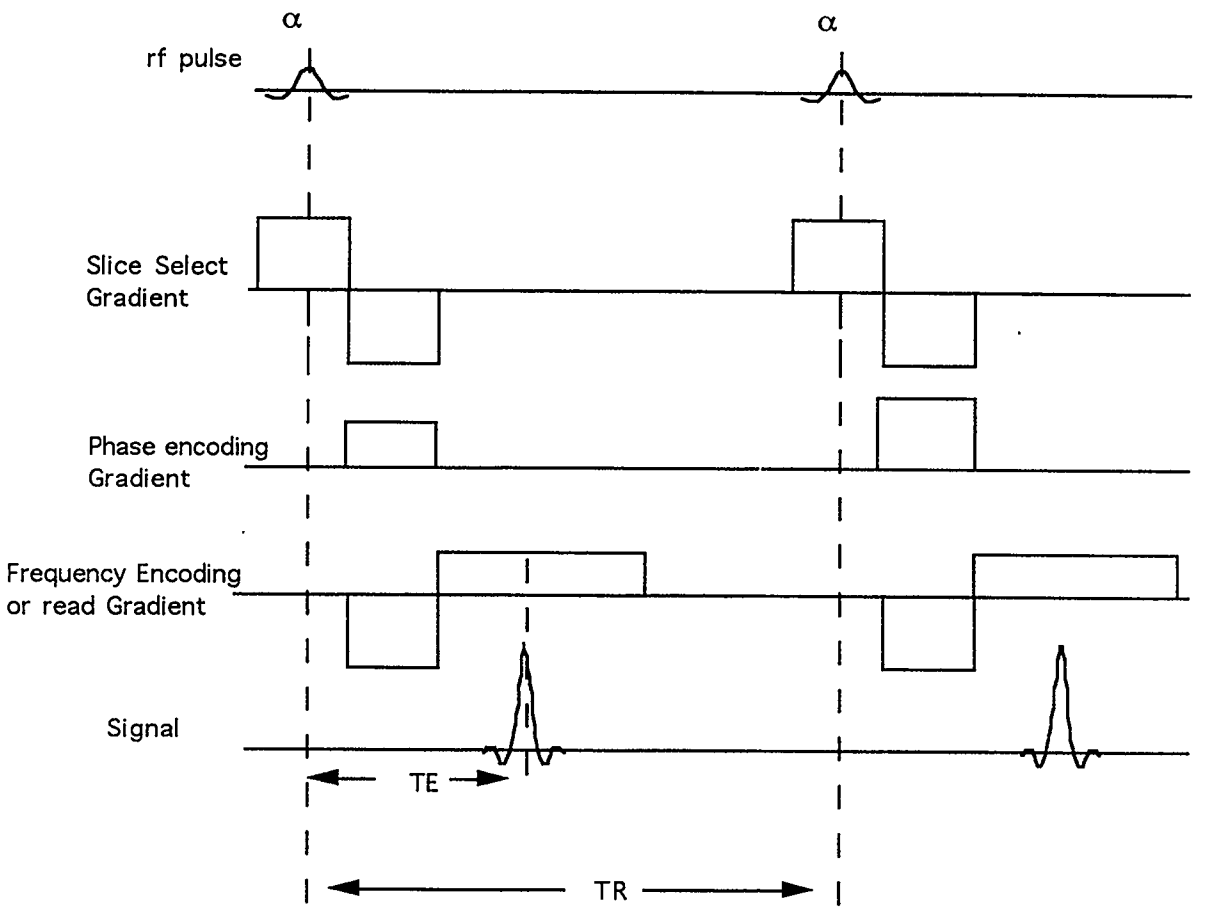

Figure 2.5 A pulse timing diagram for a gradient refocused echo (GRE). The slice is selected by the simultaneous application of the slice select or G_z gradient and the rf pulse (α). Spins are rephased by the negative lobe of the G_z gradient. Typically during this period the phase encode gradient G_y is pulsed and the dephasing portion of the read gradient G_x applied. Finally the signal is read in the presence of the rephasing portion of the read gradient and the sequence is repeated at t= TR when G_y is incremented.

The read gradient also has a compensatory rephasing portion. Since the negative lobe or the compensating portion of the gradient is applied first, then at the centre of the positive lobe, or the read portion, all spins are refocused so the resultant signal is largest at this time. The signal is called a gradient refocused echo signal, and the largest signal corresponds to the echo centre. A pulse timing diagram of a gradient refocused echo is shown in fig. 2.5. TR is the repetition time interval of the pulse sequence. The time interval between the centre of the rf pulse and the centre of the read gradient is referred to as the echo time TE.

2.3.2 Data Acquisition

Of the different strategies of data acquisition available, the one most commonly used for 2D imaging is the planar Cartesian collection method. In this method the data set is collected by varying the phase encoding gradient by a fixed increment (ΔG_y) 2n times, which basically corresponds to the number of rows in the image matrix.

For the first phase encoding step, at time t=0, defined as the time at the echo centre, the signal can be expressed as

$$S_{t=0} = \iint M_{xy}(x,y) \quad e^{i\gamma G_y t_y y} \; dx\,dy \qquad 2.17$$

where

M_{xy} is the xy magnetization component (which depends on a number of factors)

$e^{i\gamma G_y y t_y}$ refers to the total phase accumulation, which is expressed in complex notation since the signal is collected in quadrature i.e.. from two receiver channels that are 90^0 out of phase with each other.

As time evolves the spins become defocused due to the application of the G_x gradient and the signal can be written as

$$S(t) = \iint M_{xy}(x,y) \quad e^{i\gamma G_y y t_y} \quad e^{i\gamma G_x x t} \; dx\,dy \qquad 2.18$$

If the following definitions are made

$$k_x = \gamma\ G_x\ t \qquad\qquad k_y = \gamma\ G_y\ t_y \tag{2.19}$$

then the signal becomes

$$S(k_x,k_y) = \iint M_{xy}(x,y)\quad e^{i\,(k_x x\,+\,k_y y)}\ dx\,dy \tag{2.20}$$

The phase encoding gradient is incremented for the next acquisition, hence the phase shifts acquired by the spins will be different from the previous acquisition. The G_y gradient is incremented 2n times and one line of data is collected each time, corresponding to a different k_y. In this manner a data matrix is created with axes k_x, k_y, where k_y ranges from $-n\Delta k_y$ to $(n-1)\Delta k_y$, while k_x spans the spatial frequency range corresponding to the x direction (see fig. 2.6). Therefore k_x and k_y are measures of the phase advances or retardations that the spins experience in the x and y directions.

2.3.3 Image Reconstruction

From eq. 2.20 it can be seen that k_x, x and k_y, y are Fourier pairs. Hence a fast and efficient method of image reconstruction is to use a 2D-FFT, where the inverse transform is given by

$$S(x,y) = \iint S(k_x,k_y)\quad e^{i\,(k_x x\,+\,k_y y)}\ dk_x\ dk_y \tag{2.21}$$

The Nyquist relations which determine the sampling frequency and the increments in the G_y gradient are therefore dictated by L_x and L_y (dimensions of the field of view (FOV) in the x and y directions respectively). Here

$$\Delta k_x = \gamma\ G_x\ \Delta t = 2\pi\ /\ L_x \tag{2.22}$$

$$\Delta k_y = \gamma\ \Delta G_y\ t_y = 2\pi\ /\ L_y \tag{2.23}$$

The minimum FOV, in the y direction, that can be used by a particular data matrix is dictated by the maximum amplitude that the G_y gradient can attain. The smaller the pixel size needed the greater maximum gradient amplitude $n\Delta G_y$ required. The maximum amplitude of the gradient is limited by the available electronics, i.e. the

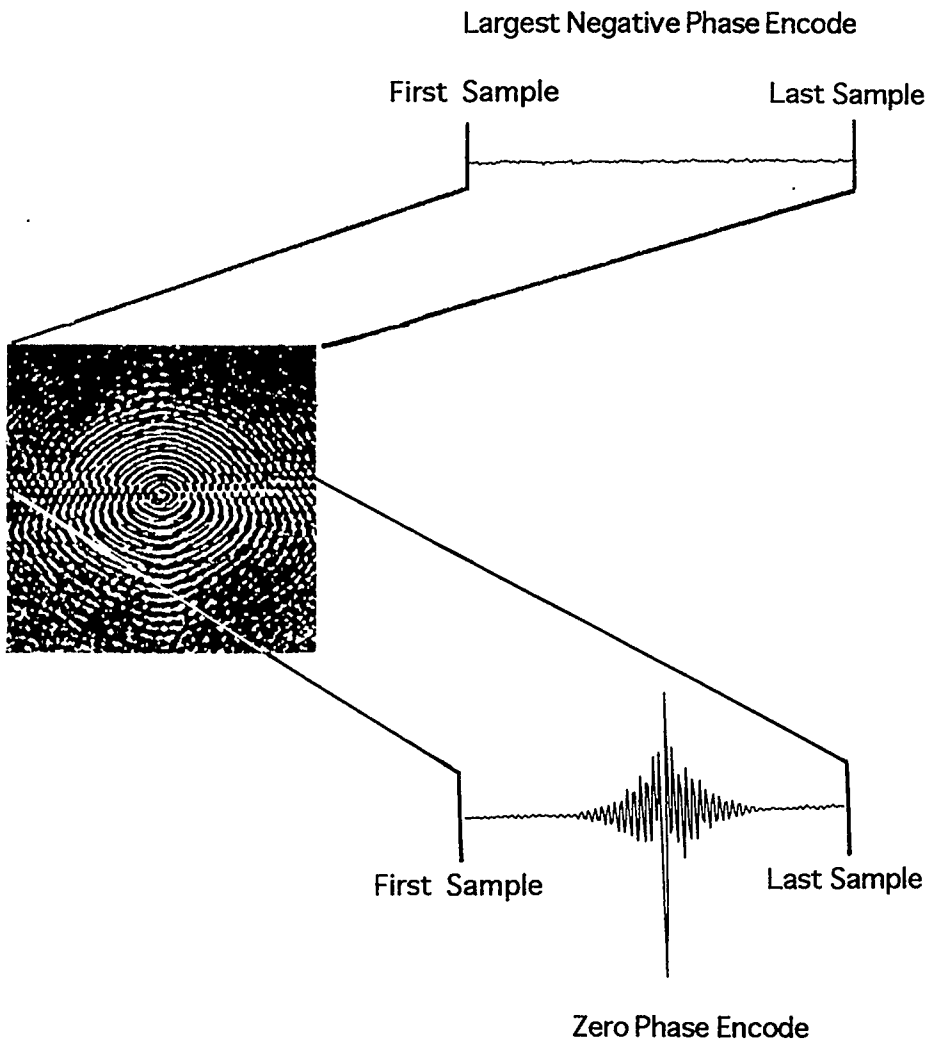

Figure 2.6 A raw data set viewed in k space. The first row corresponds to the largest negative phase encoding gradient, while the last row corresponds to the largest positive phase encoding gradient. The data in the centre row is obtained from the zero phase encode step, while that in the centre column corresponds to the echo centre (taken from Stark and Bradley, 1992, p.37 [42]).

gradient amplifiers of the system.

In the x direction, the proton linewidth is the limiting factor for spatial resolution once the available gradient strength is reached.

2.4 Signal-To-Noise Ratio

The signal-to-noise ratio (SNR) is defined as follows [42, 45 (Vol. 2)]

$$SNR = \frac{S}{\sigma} \qquad 2.24$$

where S is the signal intensity from the region of interest , and σ is the standard deviation of the signal obtained from a background region, i.e. from an airfilled region outside the sample boundary. This background region contains only noise.

In an MR image, the patient is the main source of noise arising mainly from radio frequency emissions due to Brownian motion of the molecules. The noise is accumulated from the part of the patient that lies within the reception field of the coil, not just from the slice being imaged, and it is white Guassian in nature. The noise can be minimized by using a smaller transceiver coil.

Other sources of noise include electrical resistance in the transceiver coil and noise in the preamplifier electronics. These sources of noise can be minimized by proper system design and construction. The inherent noise from the patient and the transceiver coil provide a lower limit to the noise that is present in the image.

Image quality is directly dependent on the SNR. The usefulness of the image is dependent on contrast (described in section 2.6) and on the spatial resolution. Image resolution is inversely proportional to voxel (volume element) size. However as the voxel size decreases the signal intensity within the voxel decreases, while the noise remains the same. One solution to the problem is signal averaging, which requires a repetition of the pulse sequence to generate additional data. Since the noise is

uncorrelated, averaging reduces the noise, hence the SNR in the resultant averaged image is increased by a factor of $\sqrt{N}$, where N is the number of averages performed. The penalty of averaging is the increase in scan time.

2.5 3DFT Imaging

In 2DFT imaging the excited volume is a single slice. Sequential slices are taken and stacked together to form a 3D image. In 3DFT image acquisition, data is acquired from the entire volume simultaneously. This is accomplished by using a slice selective rf pulse or a non-selective pulse to excite the whole volume. Position differentiation along the slice select direction is done by phase encoding in this direction as well as in of the G_y direction. The advantages of 3D over 2D are its ability to produced thinner contiguous slices, increased SNR for the same TR and number of slices, and the advantage of minimum cross-talk between slices. Multislab 3DFT acquisition is a combination of the 2D and 3D methods. The image volume is acquired by separately applying two or more single volumes, using thinner overlapping slabs to cover the total volume.

2.6 Contrast Phenomenology

The contrast in MR imaging is defined as the difference in signal between two different types of tissues present within the image. The definition of the contrast-to-noise ratio (CNR) between two tissue types follows from eq. 2.24 [42, 45 (vol.2)], and is written as

$$CNR = \frac{S_1 - S_2}{\sigma} \qquad 2.25$$

where S_1 and S_2 are the signal intensities from two regions of interest (ROI).

The signal acquired from a particular tissue is a function of the relaxation times

T_1 and T_2, and the proton density. The use of different pulse sequences will change the contrast obtainable between different tissue types, since the signal equation is different for the sequences. Two typical pulse sequences used are the gradient recall echo or GRE (see fig. 2.5) and the SE. The difference between the sequences is due to the SE's use of a 90^0-$(180^0)_n$ rf pulse sequence (a 90^0 pulse, followed at intervals of TE/2 by n 180^0 pulses, where n is the number of echo images required), while the GRE uses an α pulse (where α ranges from 0^0-90^0).

The signal equation obtained using a SE sequence is

$$S(M_0,TE,TR) = M_0 \left(1 - 2e^{-(TR - TE/2)T_1} + e^{-TR/T_1} \right) e^{-TE/T_2} \qquad 2.26$$

Recall that TR is the repetition time interval of the pulse sequence, and the time interval between the centre of the rf pulse and the centre of the read gradient is referred to as the echo time TE. Both these timing parameters are chosen by the operator.

The signal obtained using a GRE sequence, in which the transverse magnetization is destroyed, i.e. completely dephased, before repetition of the sequence is:

$$S(M_0,\alpha,TE,TR) = M_0 e^{-TE/T_2^*} \frac{\left[1 - e^{-TR/T_1} \right] \sin\alpha}{\left[1 - e^{-TR/T_1} \cos\alpha \right]} \qquad 2.27$$

The term $\sin\alpha$ determines the fraction of the steady-state longitudinal macroscopic magnetization that is tipped into the xy plane. Once the magnetization is tipped, relaxation occurs during TE, via mostly T_2 processes. Since differing tissue types have differing T_2 s, the TE can be used to control the signal from the various tissues types. Fig. 2.7a shows how the signal from two different types of tissues varies with time. The tissues have the same macroscopic magnetization but tissue 1 has a longer T_2 compared to tissue 2. The choice of TE will control the amount of contrast attained in the resultant image.

The T_1 contribution to the contrast is determined by the timing parameter TR, since this is the time during which the macroscopic magnetization regrows along the z

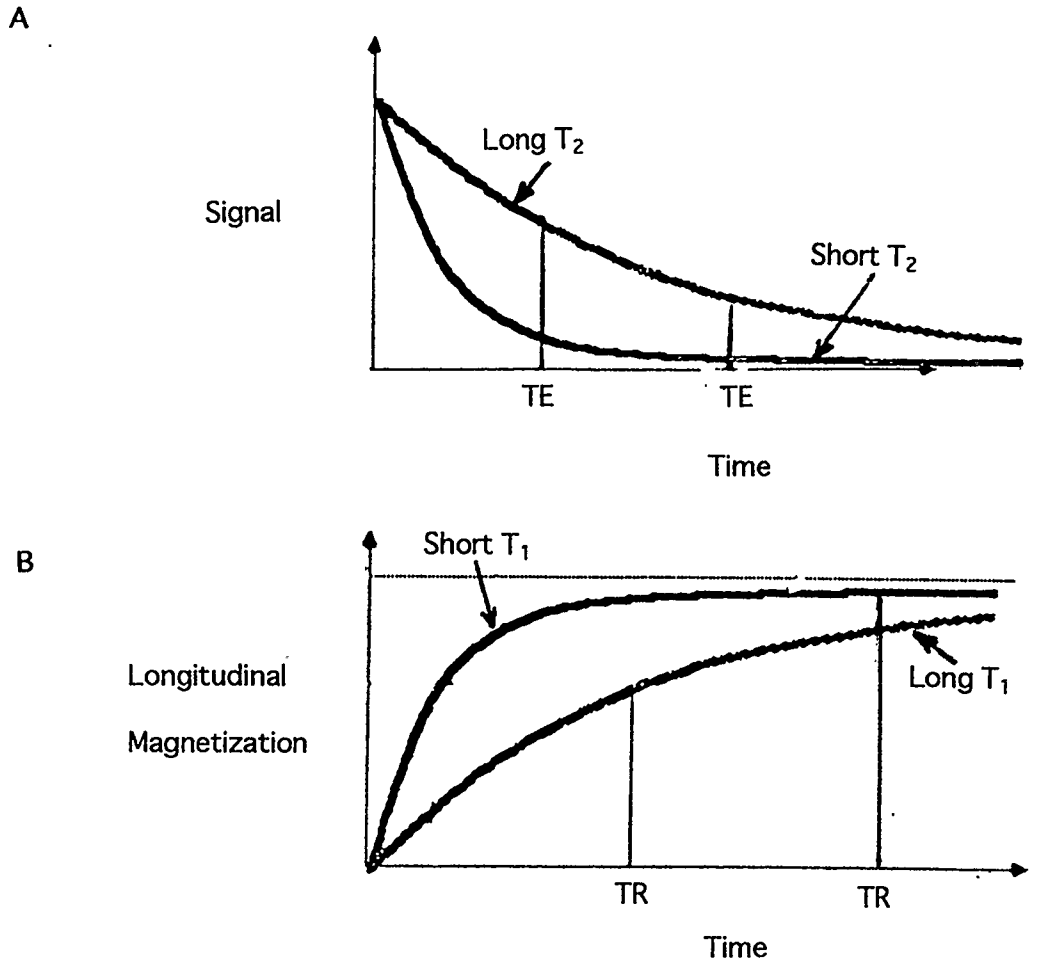

Figure 2.7 An example of how contrast between two tissues is controlled by using different values of the timing parameters in the pulse sequence.

A. This shows signal strength from the two tissues as a function of time. The choice of the shorter TE will result in better contrast in the image compared to a very long TE.

B. This shows the recovery of the longitudinal magnetization as a function of time. Here the use of the short TR will result in better contrast compared to the choice of the long TR, (taken from Edelman and Hessellink, 1990, p.12 [17]).

direction. The TR value used determines how much longitudinal magnetization is present to be tipped into the xy plane on application of the next rf pulse, i.e. how much recovery will have occurred. The longer the inherent T_1 of the tissue, the slower the recovery of the magnetization and the smaller the signal obtained. Fig. 2.7b depicts how the longitudinal magnetization between two tissue types recover as a function of time. As in the previous case the two tissues have the same macroscopic magnetization, but tissue 1 has a longer T_1 than tissue 2. The TR used controls the steady state magnetization attained. In GRE sequences the tip angle used determines the fraction of the steady state magnetization that is tipped into the xy plane.

The proton density present within the voxel controls the initial amount of macroscopic magnetization present and hence how much signal is received. The voxel dimensions can be changed by changing the slice thickness and/or the FOV used. This changes the macroscopic magnetization in the voxel.

The parameters TR, TE and α (for GREs) determine whether an image is T1-weighted, T2-weighted or proton density weighted. The choice of which weighting to use is dependent on the region that is imaged and what information is required from the image.

CHAPTER 3

COMPARISON OF ANGIOGRAPHIC METHODS

Diagnostic angiography is an invaluable aid used in the evaluation of diseases of the vascular system. It provides the specific morphologic information required in the planning of interventive action. The discussion here pertains to cerebral angiography, i.e. the blood vessels in the head and neck area (see fig. 3.1).

3.1 Vascular Diseases

Diseases of the vascular system [2, 47] include arteriosclerosis, which is characterized by the deposition of complex lipid, i.e. plaque, on the vessel wall. This can result in vessel narrowing or stenosis, with possible complication of thrombus formation, ulceration leading to embolism (obstruction of flow by the blood clot), and arteriosclerosis aneurysms (sac formation on the artery wall). Plaque appears mostly at branch points and one area where it is commonly found is the carotid bifurcation.

Embolism and aneurysms, with the accompaniment of thrombus may be caused by other factors, such as structural weakness in the vessel wall. This also usually occurs at vascular branch points, hence the carotid artery is a prime location for disease formation. A large percentage of aneurysms are found in the circle of Willis (see fig. 3.1). Vascular malformations, such as arteriovenous malformation (AVM) also disrupt the blood flow and can lead to vessel dissection, i.e. longitudinal division of the artery wall creating a "flap" that can totally occlude the vessel or deviate the flow into the vessel wall creating a "false" aneurysm or hematoma.

Diagnostic angiograms are currently made using x-rays, ultrasound and MRI. Screening is performed for interruptions in blood flow, which are classified as:

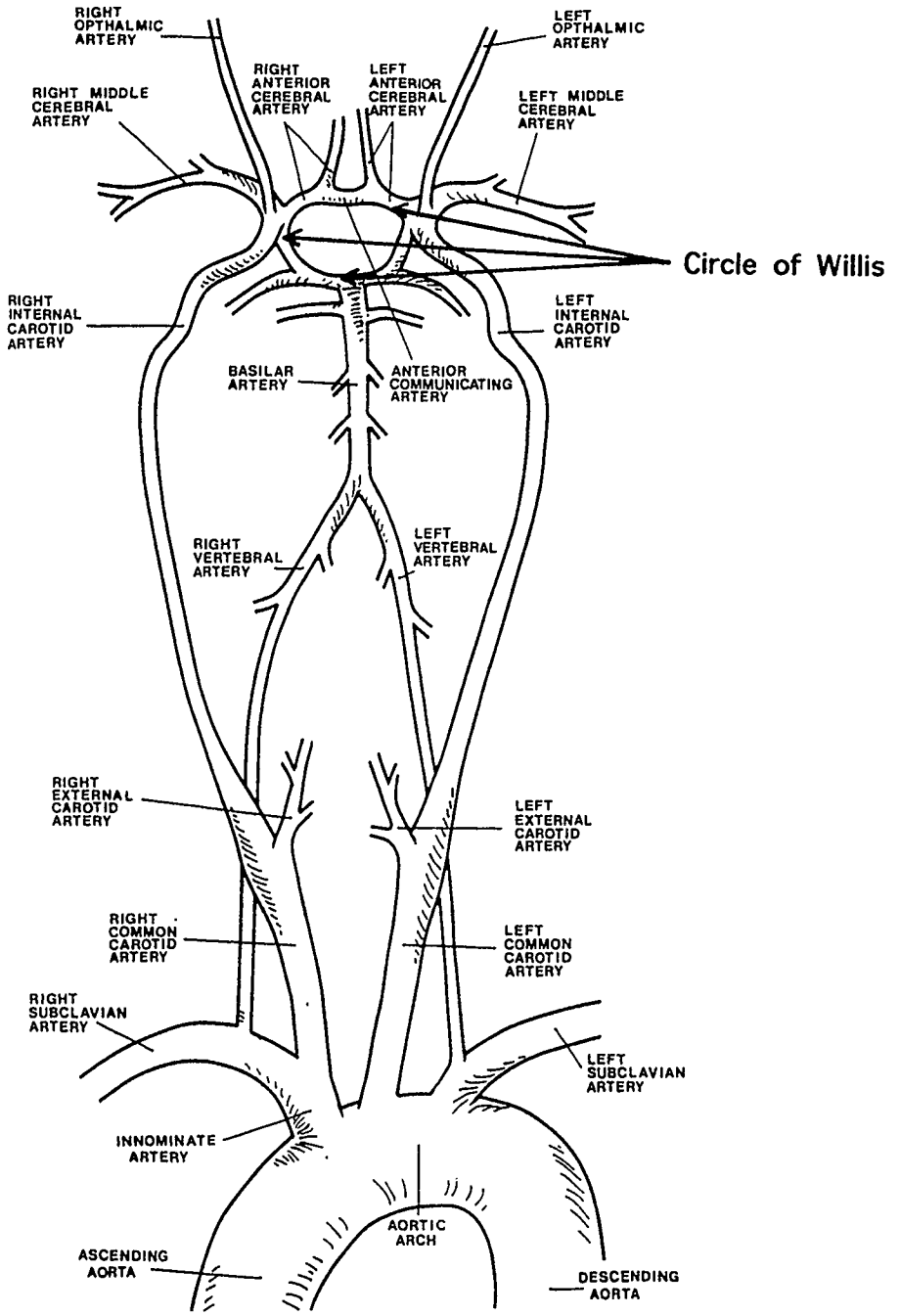

Figure 3.1 Cerebrovascular anatomy showing the vessels from the base of the brain to the aortic arch. The intracranial vessels are not shown here, but the main ones are a continuation of the vessels at the base of the brain, (taken from Zwiebel and Knighton, 1990 [48]).

1. complete vascular occlusion
2. severe flow reducing stenosis
3. low grade stenosis which does not impede flow drastically.

3.2 X-ray Angiography

This type of angiography is referred to as conventional angiography. It involves the use of a radio-opaque contrast medium introduced into the vessel, after which x-ray projections are taken [10, 25]. (A projection compresses 3D data or information into a 2D image. This is accomplished in x-ray angiography (XRA) by the intensity of exiting rays from the patient that registers on a screen or photographic film). The delineation of the vessel is observed via the interaction of the x-rays with the iodine atoms of the contrast medium. Projections taken at different times depict a dynamic demonstration of blood flow in the vessel. However there is no accurate quantification of the flow velocity.

The contrast agent is introduced into the vessel by injection and care is required to ensure that the rate of contrast introduction is close to that of blood flow to ensure mixing. Direct injection is applied in the veins for venography. This is also the preferred method in arteriography, where the injection is followed by a waiting interval until the bolus passes through the arteries that are being examined. Veins have slower flow, which combined with a wait time, allows better mixing of blood and contrast. Injections via catheter are used in arteries when the large volume of contrast medium that would be required intravenously to produce good SNR on the image, poses a problem for the patient. A smaller volume can be used if the study is "tailored" i.e. by injection of contrast close to the region under investigation.

XRA is an invasive technique that poses potential danger to the patient. Problems include adverse drug reactions to the contrast medium which can be mild to severe,

resulting in death. Placement of the catheter always has a danger of introducing clotting, which can result in new stenoses being formed with accompanying complications.

Contrast enhancement of the vessel can be obtained through subtraction angiography. This is accomplished by taking a projection prior to the arrival of the contrast and then subtracting this from subsequent projections. This is called masking as it removes distracting structures like bones from the picture. Digitization of the x-ray image allows digital subtraction angiography (DSA) to be accomplished. In DSA, contrast is increased by other image processing methods, such as edge enhancement, scatter and motion corrections so that decreased concentration of iodine can be used. Digitization results in decreased spatial resolution (11 lines/mm) compared to photographic film images (17 lines/mm), so films are also obtained.

Conventional angiography is the oldest technique in this field. It reveals most flow abnormalities, which are well documented in any medical XRA text such as reference 6, but it gives little information about the disease pathology involved. It is considered the gold standard in angiography against which the performances of the other modalities are usually measured.

3.3 Ultrasonography

Ultrasound uses the reflection of sound waves from different interfaces to image body tissue [44, 48]. The time for the return of the echo is converted to a depth measurement producing a real time brightness modulated or B-mode image.

Duplex ultrasonography (DUS) uses the time, amplitude and frequency of the returning echo to create an image. Doppler encoded velocity information is shown as a colour display superimposed on a B-mode image. The information obtained from this image includes the location and possible identification of the vessel, detection and

composition of plaque and assessment of the percentage of stenosis present in the vessel. The velocity information shown on the image is qualitative, but some quantitative information can be inferred from an analysis of the Doppler spectrum.

The primary problem with DUS is that it is very operator dependent. A high degree of competency is expected from the technologist, as a false positive diagnosis can result from operator handling (see fig. 3.2). There is also an inability of DUS to distinguish between a total occlusion and a pseudo-occlusion, due either to the instrument not being set to display slow rates, which can be corrected by the technologist, or the limitation of the receiver to detect a small Doppler shift. Other problems exists in the detection of ulceration, differentiation of thrombus from plaque and the possibility of calcified plaque generating acoustic shadows which obscure stenosis information.

Ultrasound is a non-invasive technique with zero risk factor. Since DUS uses a 5 - 10 MHz with an ~ 5 MHz Doppler window, it cannot penetrate bones hence it is restricted to the neck area. However analysis of the common carotid waveform can infer the presence of obstructions at locations in the carotid system outside of the DUS window, such as in the carotid siphon.

3.4 Magnetic Resonance Angiography

MRA is possible because of the effect of moving spins on the resultant signal [5, 38, 41]. Two effects that are considered are :

1. Motion between the rf pulse repetition, which is referred to as the time-of-flight (TOF) effect, is the basis for one class of MRA imaging technique.
2. Phase effect, due to motion in the presence of the imaging gradients which

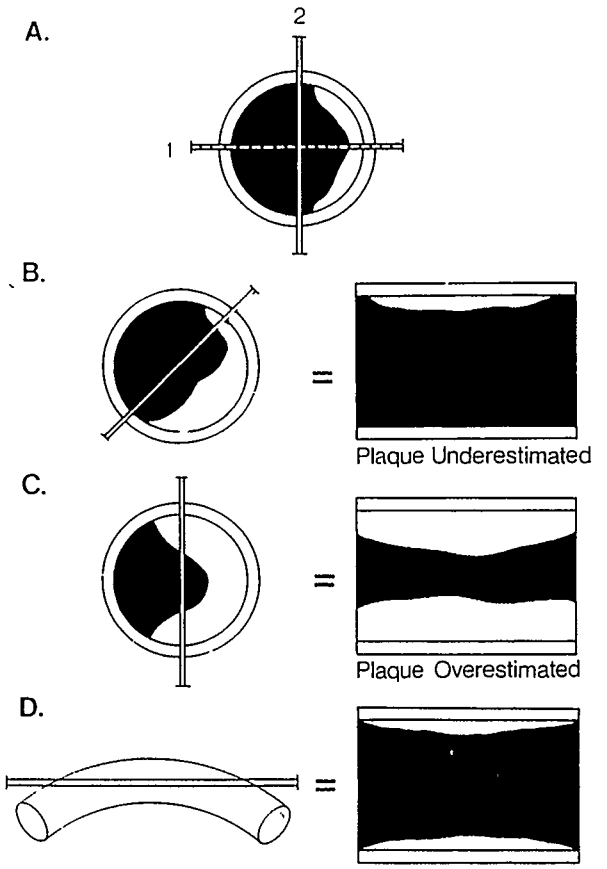

Sources of error in plaque and stenosis measurement. (A) Plaque will be visualized in a longitudinal section corresponding to line 1 but will be overlooked in a longitudinal section along line 2. (B) The thickness of plaque and the degree of lumenal narrowing will be underestimated in a longitudinal section along the line shown. (C) The severity of plaque and lumenal narrowing will be overestimated in the illustrated longitudinal section. (D) A longitudinal section through a curved vessel may suggest plaque when none is present.

Figure 3.2 Some sources of error that can arise in DUS, most of which are clinician dependent, diagram taken from Zwiebel and Knighton, 1990 [48].

imparts an additional phase to the nuclei, is the basis for the phase contrast (PC) imaging techniques.

Vascular imaging using MR is a fast growing field with new proposals of scanning techniques and image processing methods. Current clinical implementation of MRA has not attained its full potential as each method has to be evaluated with respect to its clinical performance.

On an MR image, depending on the pulse sequence used, flow can have a bright or dark appearance compared to the surrounding tissue. This gives rise to the classification of MRA into bright blood and black blood angiography.

3.4.1 Bright Blood MRA

A bright blood image results from the increased signal of flowing spins relative to stationary ones. This effect is observed on TOF and PC imaging techniques, each of which has its own advantages and drawbacks.

3.4.1.1 Time-Of-Flight Methods

TOF based angiograms can be categorized into three approaches, the 2D TOF, single volume 3D TOF and multislab 3D TOF [45]. The single volume 3D TOF approach, while having the advantage of increased spatial resolution, shows a drop off in vessel signal in slices distant from the first or entry slice (see fig. 3.3), due to increasing spin saturation. The 2D TOF method has the advantage of having unsaturated inflowing spins, hence it is most sensitive to slow flow. Multislab 3D TOF imaging is a compromise between 2D and single volume 3D; it takes advantage of the smaller voxel size available by using 3DFT imaging and maximizes the TOF effect by the use of thinner slabs.

There are a number of pulse sequences, based on the GRE, that use the TOF effect to image flow [38]. One category of sequences uses a spoiled GRE with flow compensating

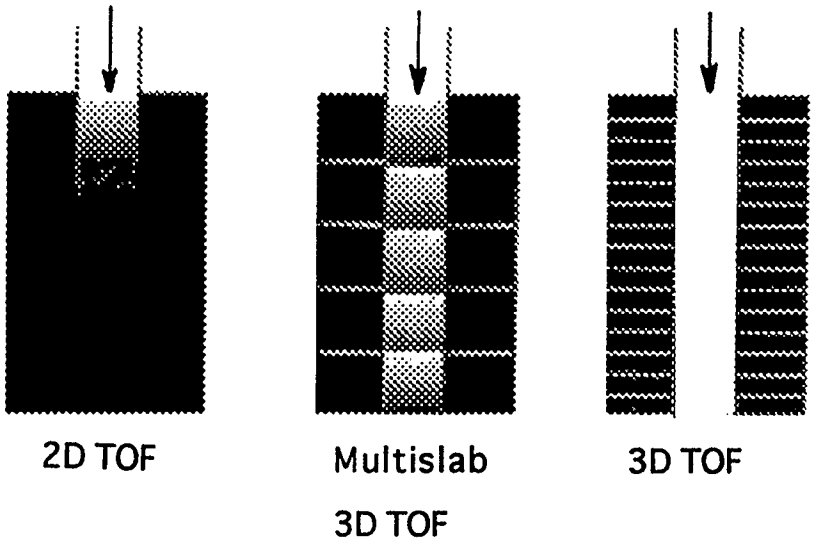

Figure 3.3 The contrast behaviour of three TOF methods, in the figure the darker the area the lower the signal, and the arrows indicate the flow direction. The 2D TOF shows no drop in signal as a function of slice position, whereas the 3D TOF techniques do. The 3D multislab technique is seen as the best compromise between single volume 3D and the 2D techniques. The 3D multislab shows a lessser saturation effect in downstream slices compared to the 3D single volume, but has the advantages of 3 DFT imaging (see section 2.5) over 2D TOF.

gradient. A spoiled GRE is used to eliminate T_2 dependence by dephasing the steady state transverse magnetization that results from the use of a GRE. Therefore only the longitudinal magnetization affects the signal. This can be accomplished by successively incrementing the phase of the rf pulse.

If a flow compensated spoiled GRE is used, contrast is obtained by choosing the combination of TR and flip angle so that the signal generated by the stationary tissue is low, while using the TOF effect to increase the signal from flowing spins. Overlapping venous and arterial vessels can be selected by the use of a spatial pre-saturation pulse applied prior to the pulse sequence, either proximal or distal to the slice or slab being imaged. This involves the use of a 90^0 slice selective pulse applied outside of the region of interest. In arteriography for example, the pre-saturation pulse is applied on the venous supply side of the slice or slab. Hence spins entering the slice from the venous side have no longitudinal magnetization to be tipped into the transverse plane by the succeeding rf excitation pulse.

The contrast of TOF images would be improved if the static tissue signal could be removed or suppressed totally from the image. A few methods have been proposed to accomplish this [38, 49], one of which is the use of an α- 180^0- α flow compensated GRE sequence [49]. The application of the first α pulse tips the magnetization towards the y direction, the 180^0 pulse applied along the y axis rotates the magnetization to an equivalent position under the transverse plane, and the application of the next α pulse aligns the magnetization with the -z axis. Therefore when the refocused echo is formed, the static tissue magnetization is aligned along the -z axis, so no static tissue signal is generated. The disadvantage of this method is the increase in imaging time due to the long TR required to allow the flowing spins to recover. Also, the application of the increased rephasing and dephasing gradient lobes requires a longer TE. The consequences of this in regions of complex flow is an increase in signal loss from increased intravoxel

dephasing. This dephasing is explained in the next chapter.

TOF subtraction angiography has also been proposed [19, 34, 38, 43, 45, 46]. Utilizing sequences based on the method of selective inversion recovery (SIR) is one way to accomplish this. This method acquires two cardiac gated projection angiograms obtained on alternating heartbeats in an interleaved fashion. In arterial imaging, for example, one image is acquired with a slice selective pre-inversion pulse applied to the slab and the venous supply side. A non-selective pre-inversion pulse is used for the second image. The static signal and the venous flow signal are subtracted out in the resultant difference image.

3.4.1.2 Phase-Contrast Methods

PC angiography has the advantage of being sensitive to slow flow, since it relies on the accrued phase shift of moving spins. PC pulse sequences can also be broadly classified into 2D PC and 3D PC [45], however 3D PC methods are more commonly used.

The PC technique uses a bipolar flow encoding gradient together with a GRE sequence [12, 21, 36, 38]. The resultant image is obtained from the subtraction of two data sets, with the second set acquired using the bipolar gradient of opposite polarity, as will be explained in the next chapter.

When the flow velocity has components in all three orthogonal directions, then flow encoding in the three directions is required, thereby tripling imaging time. This results in the accumulation of six data sets, i.e. three pairs. Each pair is processed and the resulting data is transformed via a 3D-DFT to a volume image. The final magnitude image is calculated using vectorial addition on the set of signals for each pixel to yield a flow speed angiogram. If direction of the flow is known (from knowledge of the anatomy of the region to be imaged), use of this method gains nothing in terms of CNR (eq. 2.25) with the additional disadvantage of increased imaging time.

Alternatively a reference data set can be made using a flow compensated GRE sequence (explained in section 4.2.1) with no bipolar gradient, and then encoding in each of the three orthogonal directions, i.e. creating four data sets. Processing is done in the same manner as for the six data sets, with the reference set being subtracted from each direction. This unbalanced four point method has the advantage of lower imaging time, but the error in the signal from each voxel is correlated since a common reference set is used.

The balanced four point method uses four data acquisition sets as well, but the bipolar gradient is altered in pairs (see chapter 4). Subsequent image processing for each direction includes addition and subtraction of two phase measurements, hence the phase shift common to the four data sets is subtracted out. This also results in no noise correlation in the velocity components.

Reconstruction of a magnitude image from one of the PC data sets, will yield a T1-weighted image. However the presence of the bipolar gradient produces an image that is more sensitive to aliasing and to turbulent or complex flow pattern compared to an image obtained without the bipolar. The resultant image appears "degraded" and is currently not considered to be satisfactory as a standard T1-weighted study for clinical analysis [38]. The reference data set from the unbalanced four point method can be processed to generate a standard T1-weighted image as it is collected with the bipolar gradient turned off. This is an advantage, since standard T1-weighted images are required with the MRA images, which would otherwise necessitate additional scans. Therefore the use of the unbalanced four point method would decrease the total scan time for the examination compared to the six point or the balanced four point method.

2D PC projection angiograms are not extensively used in MRA because both the TOF and 3D PC methods can be used to produce projections in any desired direction [4]. The advantage of 2D PC is that it can be used to visualize flow in a large anatomical

region, needing little acquisition time and no additional image processing to create a projection image. This can be used for rapid evaluation and as a localizer to position additional MRA sequences. Additionally PC sequences have the advantage of directly encoding velocity information.

3.4.2 Black Blood MRA

Black blood angiography is generally accomplished by the use of a SE (90^0-180^0) pulse sequence [41, 42]. When flow is present in the slice, some of the spins that have been excited by the 90^0 pulse exit the slice in time TE/2, so there is no contribution from this portion of spins in the echo. The inflowing spins have not seen the 90^0 pulse, and will therefore have no transverse magnetization component. This results in signal loss within the vessel lumen and flow can appear as a total signal void.

Since black blood angiography relies on the absence of signal from flowing spins, any intraluminal signal is undesirable. Methods for additional signal suppression include application of pre-saturation bands outside of the volume of interest [16, 38], resulting in no longitudinal magnetization present in inflowing spins and hence no signal contribution. Residual signal due to slow moving spins maybe decreased by using additional gradients and/or increasing TE to increase spin dephasing.

The problem with SE sequences is the increased imaging time required, and their inability to separate arterial and venous flow. A rapid scan method using either a 2D or 3D GRE sequence with a pre-saturation pulse has been suggested to overcome the first of these problems. A variation on this method uses the application of a 180^0 non-selective pulse, immediately followed by a 180^0 slice selective pulse which inverts the magnetization of all the spins outside imaged region. A wait time TI prior to the 2D or 3D fast GRE sequence allows the flowing unsaturated spins within the slice to exit, to be replaced with inflowing saturated spins. If the TI used nulls the vascular signal when the

zero phase encode is on, the differentiation between flow and static tissue will be maximized [16]. This pulse sequence is less sensitive to motion artifacts and will differentiate the venous from the arterial flow. Use of pre-inversion instead of pre-saturation removes the dependence on flow direction, as well the generation of flow voids is facilitated by the employing thin slices. However slow flow, as always, would be a problem.

3.5 Image Display

The ability of MRA to depict the vascular system in a projective format similar to XRA, as well as being able to use any arbitrary angle of projection through the same data set is a great advantage [26, 41, 42]. The projected image is made by using a ray tracing program. The ray paths are projected through the stack of image slices that make up the original volume data set (see fig 3.4). A rotating cine display, set around any axis, can be obtained if projections from different angles are calculated.

There are several ray tracing packages available, based either on the maximum intensity projection (MIP) algorithms or on summation projection [38]. The MIP is most commonly used since the CNR that can be attained is greater than that obtained from summation projection algorithms, if the vessel width is shorter than the number of image slices being used [8].

MIP is used with bright blood angiography. The algorithm evaluates the signal intensity along the projected path. The largest signal encountered by each ray is assigned to the corresponding pixel in the projected image.

However there are some major disadvantages to the MIP algorithm [3]. Since the vessel boundaries and regions of slow flow have low signal, these areas may be falsely displayed using MIP. This results in over-estimation of stenoses and possible loss of

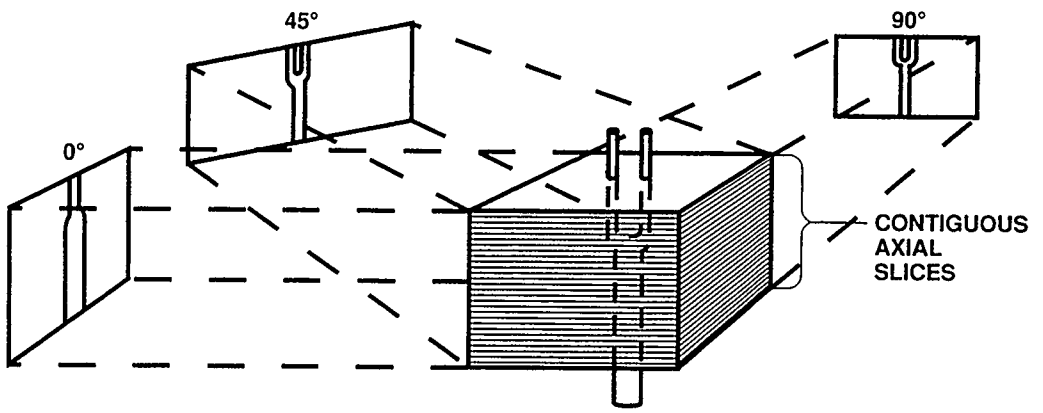

Figure 3.4 Projection images obtained from a 3D volume image set. The MIP selects the highest pixel values along the chosen ray path. Here three projections from the same data set are shown, taken from three different angles. (Taken from Keller et al, 1989 [26]).

visualization of small vessels or slow flowing blood. Attempts to solve this problem is made by suppressing background tissue signal, which can be accomplished via the pulse sequence or by additional image processing methods [29, 38, 40]. Targeted or clipped MIP can be used to improve the MIP results [38]. This looks at a small volume of interest, hence decreasing the probability of loss of vessel information by elimination of overlapping features and reduction of background projection effects.

Connected voxel algorithms [40] are also used in which a threshold intensity is set, and all voxels with lower values are eliminated. The remaining voxels are grouped separately, with group membership determined by whether that voxel is connected as a nearest neighbour to other members within the group. This results in voxels from blood vessels being differentiated from the rest, after which additional processing such as MIP is performed.

In black blood angiography a similar algorithm to MIP is used, except in this case it is a minimum intensity projection [42]. Here the major problem encountered is the overlapping of veins and arteries since they cannot be differentiated.

3.6 Comparison of DUS, MRA and XRA

The availability of multiple imaging modalities that can be used in the diagnosis of vascular diseases means that clinical comparison studies have to be performed to assess their efficiency and risk. These studies can be divided into two areas, the extracranial and the intracranial vascular systems. Currently only MRA and XRA can be performed in both areas, as DUS is restricted to the neck area, i.e. the extracranial vascular system. Of the three only XRA is invasive, hence posing the greatest risk to the patient.

3.6.1 Extracranial Comparison

The North American Symptomatic Carotid Endarterectomy Trial (NASCET) has proposed, based on clinical studies, that identifying and operating on carotid bifurcation stenoses of 70% to 99% can lead to substantial risk reduction for stroke [2, 33]. This indicates that sensitivity as well specificity for stenosis detection is important.

In most hospitals DUS is currently the chosen method for the screening of atherosclerotic disease in the carotid arteries [38]. Comparison studies of DUS vs. XRA show that DUS has a high sensitivity for clinically relevant stenoses but tends to over-estimate stenoses at the carotid bifurcation [23, 33, 37, 38, 44, 47, 48]. It cannot always differentiate total occlusion from a severe stenosis. DUS on its own cannot assess tandem intracranial stenoses that may preclude direct intervention. Economically, however, the cost of DUS is only 6% of the cost of XRA.

To date, MRA has shown high sensitivity but variable specificity, dependent on the pulse sequence, in detecting diseases of the bifurcation [23, 31, 33, 37, 38, 41, 47]. Currently 3D TOF has shown a better correlation (r ranging from .94 to .97) than 2D TOF with XRA in carotid stenosis assessment. In this respect 3D TOF performs better than 2D TOF due to its better spatial resolution. However 2D TOF is far more sensitive to slow flow, and it is used to differentiate an occlusion from a critical stenosis. Some comparison studies conclude that 2D and 3D TOF are both necessary for optimal evaluation [38]. The use of subtraction TOF methods would increase static tissue suppression and result in fewer pitfalls in the use of MIP.

3D PC has the advantage of quantifying flow directly, complete static tissue suppression, and no pitfalls from bright stationary tissue in the use of MIP, but it has a major disadvantage of increased imaging time [4, 38]. The unbalanced four point method can generate a standard T1-weighted contrast image as well as the 3D TOF. A current study suggests that MRA together with standard MR images is a better indicator of the

presences of dissection in the artery. Flow void narrowing is a less useful indicator than is external arterial diameter because it is less specific, especially as elastic vessels compensate for plaque build-up by stretching to maintain lumen diameter. However TOF is currently preferred over PC as the TOF images allows direct visualization of hematoma. On TOF images hematoma appears bright simulating flow since it has a short T_1 [38]. This is a double-edged sword as it can pose a problem if the TOF data is analyzed on its own using MIP. In PC images the possibility of the flow encoding gradient not being sensitive enough to distinguish slow flow from thrombus is high, and the hematoma can be missed. A SE image is sometimes acquired to resolve the question of artery dissection.

Bright blood angiography has a tendency to over-estimate the stenosis due to signal loss. Black blood angiography does not suffer from this degradation and it shows good flow sensitivity. However it requires long imaging times, and it cannot be applied to any portion of the vascular system that passes through bone or air, as both air and bone produce no signal, hence mimicking flow. As well, any intraluminal signal is problematic [18, 38].

Comparison of TOF MRA to DUS shows that there is little statistical difference in their specificity, but MRA appears to be more sensitive [33, 38]. Economically, DUS is preferred to MRA which is 10 times more expensive, but without the use of additional tests, DUS does not give much intracranial information [2]. XRA remains the conclusive study for determination of endarterectomy.

3.6.2 Intracranial Comparison

MRA of the intracranial vascular system is performed primarily using 3D sequences, which routinely shows stenoses in the primary branches of the circle of Willis. Determination of collateral flow patterns with TOF methods requires several

data acquisitions and the use of pre-saturation pulses to produce complete information. Using 3D PC, only one complete data acquisition set (six point or four point) is needed.

Due to the decreased spatial resolution available, MRA is less reliable in the evaluation of small vessels. In the venous system 2D TOF is much more sensitive compared to 3D PC, which is better than 3D TOF [22, 24, 28, 38].

Use of MRA in screening for aneurysms is controversial, since MRA shows a 95% accuracy of detection, but it fails to depict small aneurysms (< 5 mm). The complications from small aneurysms are low, but the jury is out as to whether MRA is acceptable on its own without the use of XRA [38, 47].

MRA is sensitive for AVM and other vascular malformations, and recent studies suggest that it has a higher sensitivity than XRA [38]. However, although the location of the nidus can be determined, it is difficult to define feeding vessels and shunting. It has been proposed that high flow feeding vessels can be detected on multiple phase-sensitive MRA images with different flow sensitivity. To date however XRA is the only definitive method that can be used.

MRA has replaced XRA for detection of thrombosis involving the major venous sinuses, and for depiction of tumor encasement of major venous structures [38]. However XRA remains the conclusive study performed for determination of endarterectomy.

3.7 Future developments

Low frequency transcranial color coded Doppler ultrasound (a 2.25 MHz window with 2 MHz pulsed Doppler) uses the temporal bone window for intracranial vascular imaging [7]. This has the disadvantage of lower spatial resolution compared to the other modalities, but its use with conventional DUS accompanied by other indirect tests, can

provide a totally non-invasive screening procedure for vascular disease, at a lower cost.

Three dimensional sonographic reconstruction [39], facilitated by the use of a 3D probe, provides an image display format similar to that achieved by the other two modalities, overcoming a big disadvantage of DUS. However, the problem of a noisy or "mottled" image still remains. The use of the 3D probe can make DUS even more attractive as the sole screening procedure of choice since it is currently the least expensive and conversion of current ultrasonic imaging units to 3D capabilities is relatively inexpensive. The 3D probe also makes examinations less clinician dependent, so results will be more reproducible. The use of a sonographic contrast agent, that is of practical use and potentially harmless, has recently been developed [39] and its use will enhance DUS performance. The clinical performance of these developments, is currently being evaluated.

The implementation of helical computer tomography (CT) for angiography is also a possibility on the horizon [32]. Although CT is invasive, it has a lower potential risk than XRA since a lower volume of contrast agent is required, which is not administered via a catheter. CT is also less expensive than MR, but its clinical performance is yet to be determined.

The technology of MR has several ongoing new developments [14, 38, 47, 42]. Some of these are a major advantage to MRA, such as rapid scan techniques (spiral scanning, echo planar imaging) and the use of 1/2 rf pulses and 1/2 echo data collection. Research is also ongoing in the development of "fluoroscopic" imaging for use with interactive real time imaging to facilitate patient positioning [38], as well as to image dynamic phenomena such as flow communication in the nidus.

Improvements in XRA include the area of catheter material (to try to lower the chances of blood clotting), the development of newer radio-opaque dyes that have fewer side effects, and better methods of catheter guidance to decrease the probabilities of

unwanted vessel puncture.

3.8 Conclusion

MRA is less expensive than XRA and most importantly poses no known potential danger to the patient. Compared to DUS, it can be used in any area of the body, has better resolution, more reproducible results and its image display format yields more information.

However, with any of the current pulse sequences used in MRA the problem of signal loss at the boundary of the vessel, makes measuring stenoses unreliable, and signal loss from slow flow due to abnormalities, can mean loss of crucial information. Optimization of the boundary signal, in effect optimization of the signal from slow flow, is a factor in solving this problem. Optimization of the boundary signal for the PC techniques includes a consideration of velocity dispersion effects, which are more commonly associated with complex flow patterns such as those found in the carotid bulb.

CHAPTER 4

COMPUTER SIMULATIONS

Described in this chapter are the computer simulation theory and algorithms used in the comparison of the TOF and PC techniques.

4.1 Flow Type

Computer simulations and experiments were used to compare the performance of the TOF and PC techniques at the vessel boundary. This required the choice of a flow profile that would reflect the in-vivo situation and would easily be generated for the experiments.

The flow type chosen was a laminar flow distribution having a parabolic velocity profile across the vessel. If the mean velocity is v_m then the distribution is given by

$$v(x,y) = 2\, v_m \left(1 - \frac{(x - x_c)^2}{r^2} - \frac{(y - y_c)^2}{r^2} \right) \qquad 4.1$$

where r is the radius and (x_c, y_c) are the center co-ordinates of the vessel.

An accurate mathematical description of in-vivo blood flow is very complicated due to the presence of a number of unknown factors, such as variable heart rates, vessel walls not being rigid, blood being a non-Newtonian fluid, and variable vessel diameter creating additional pressure gradients. What is known in MR, however, is that angiograms show signal loss at vessel boundaries due to slow moving spins and to the presence of large velocity gradients [38].

A parabolic velocity profile has both large velocity gradients at the boundary of the vessel and slow moving sins. Investigation of signal loss at the vessel boundary for this profile, while simplistic, is not however unrealistic in its approximation to in-vivo boundary flow behaviour.

4.2 Time-of-Flight effect

TOF refers to the movement of spins into and out of the selected slice. This migration of spins alters the resultant MR signal [5]. The simplest case to examine is the use of a GRE sequence to image plug flow perpendicular to the imaging plane (see fig. 4.1a).

Spins located anywhere within the bore of the magnet are magnetized, but the signal is acquired only from the selected slice. Between acquisitions, blood containing fully magnetized spins (i.e. fresh or unsaturated spins) enters the selected region. Simultaneously, flow containing partially saturated spins (i.e. spins that have experienced at least one previous rf pulse) are transported out of the slice. Hence the resultant signal from the next acquisition will have a strong signal contribution from the fresh spins, in addition to a weak signal from the partially saturated spins. Also, depending on the timing parameters chosen, the static tissue is likely to be partially saturated (i.e. it never fully recovers between acquisitions) and will produce a relatively weak signal. The result is an increased signal from the blood coupled with a decreased signal from the tissue, i.e. an overall increase in contrast. Hence, flowing blood appears as a relatively bright signal in the image.

If the velocity v_0 of the blood flow is within the range $\Delta z/TR$, where Δz is the slice thickness, then all the spins within the slice will be replaced by fresh spins. This condition produces the largest achievable signal for this particular pulse sequence.

If the flow is laminar (fig. 4.1b), the signal contributions of slow moving spins at the vessel boundary would be weak as the spins become partially saturated. Under-estimation of the vessel width results, or conversely stenoses will be over-estimated, as it becomes difficult to differentiate between tissue and blood signal at the vessel boundary.

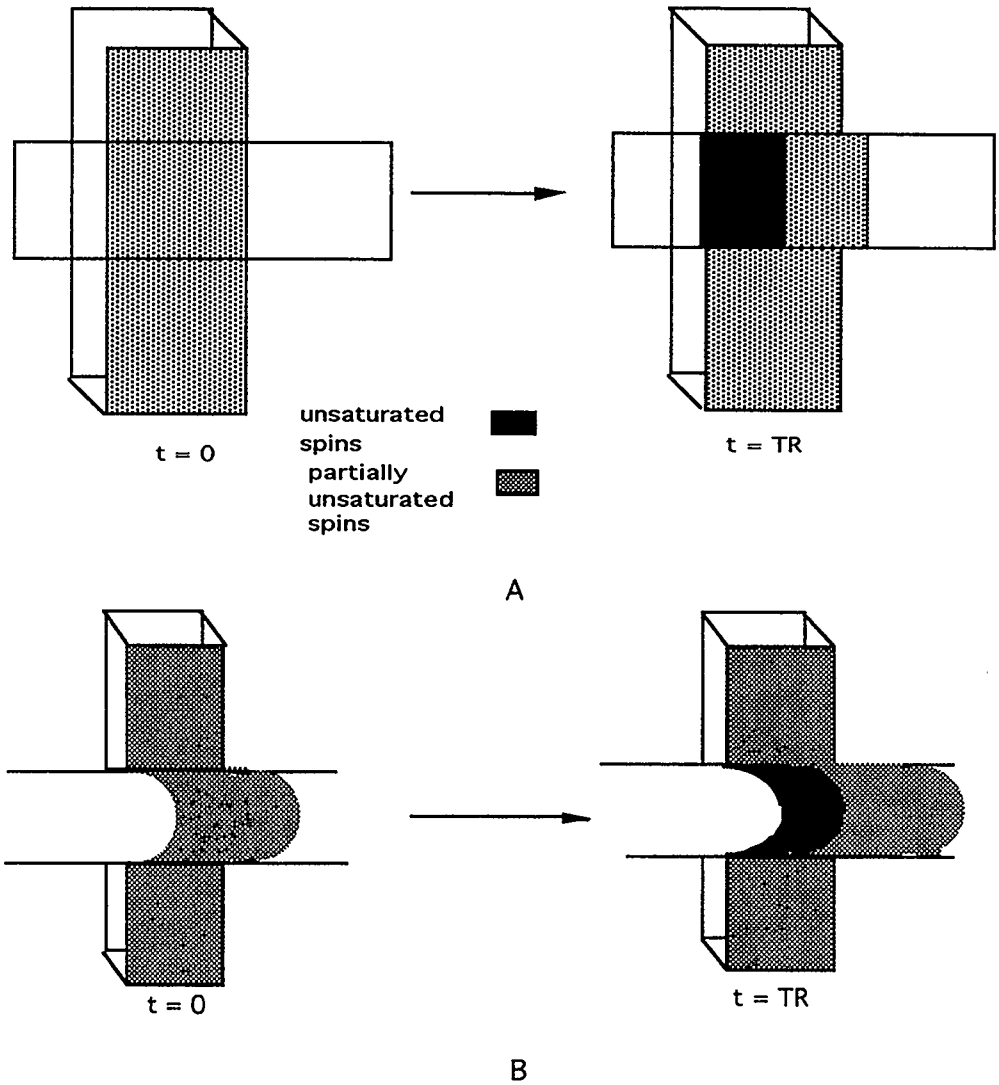

Figure 4.1 The TOF effect: at t = 0, the slice is selected and the spins are tagged. At t = TR when the next line of data is being collected - there is a migration of spins that have been tagged by the previous rf out of the slice.

A. This shows the TOF effect for plug flow, which does not have slow moving boundary spins.

B. This shows the TOF effect for laminar flow which will have decreased signal at the boundary.

4.2.1 Simulation of the TOF effect

Simulations were performed for a GRE, since clinical MRA utilizes fast GRE techniques. GRE sequences are preferred because they do not require a refocusing 180^0 pulse. The GRE sequence uses low tip angles and short TR, which promotes saturation of the static spins in the slice. The angiogram is obtained using the images acquired from a number of consecutive slices, and a MIP algorithm is performed to build the 3D picture of the blood vessels. Hence to decrease the total scan time involved in acquiring a large number of slices, the GRE is the best choice.

In a GRE, the signal is directly proportional to the xy-component of the magnetization, which on application of an rf pulse, of tip angle α is

$$M_{xy}(t) = M_z^- \sin\alpha \, e^{-t/T_2^*} \qquad 4.2$$

where t = 0 is the time of application of the rf, and M_z^- represents the magnetization vector before the application of the rf pulse. Solutions to the Bloch system of equations show that

$$M_z(t) = M_0 - (M_0 - M_z^- \cos\alpha) \, e^{-t/T_1} \qquad 4.3$$

where M_0 represents the initial magnetization of the system, prior to any rf pulses.

If flow is present within the slice, then any voxel within the region of flow will contain a variety of spins that have experienced differing numbers of rf pulses. The signal from the voxel can then be calculated by categorizing the spins into groups depending on the number of rf pulses experienced, and obtaining their contributions to the resultant voxel signal.

Consider the signal in a voxel after application of the first pulse sequence, i.e. at time t = TR. The magnetization present is given by

$$M_1 = M_0 - (M_0 - M_0 \cos\alpha) \, E \qquad 4.4$$

where $E = e^{-TR/T_1}$. After the jth rf pulse, the steady state magnetization from eq. 4.3 is

$$M_j = M_0 - (M_0 - M_{j-1} \cos\alpha) \, E = M_0 (1 - E) + M_{j-1} E \cos\alpha \qquad 4.5$$

On repeated application of eq. 4.3 this can be rewritten as

$$M_j = M_0 \left((1 - E) \sum_{i=0}^{j-1} \varepsilon^i + \varepsilon^j \right) \qquad 4.6$$

which can be simplified to

$$M_j = M_0 \left(\frac{1 - E}{1 - \varepsilon} + \frac{E - \varepsilon}{1 - \varepsilon} \varepsilon^j \right) \qquad 4.7$$

where $\varepsilon = E \cos \alpha$.

If the argument is extended to a voxel containing flow, then the magnetization of the fraction of spins that have seen j rf pulses is represented by the above equation. Hence the total magnetization in the voxel can be written as [35];

$$M_{voxel} = A + B \sum_{j=0}^{N} \omega_j \varepsilon^j \qquad 4.8$$

where

$$A = \frac{M_0 (1 - E)}{1 - \varepsilon} \qquad B = \frac{M_0 (E - \varepsilon)}{1 - \varepsilon}$$

and ω_j represents the fraction of the spins present that have experienced j pulses.

After N rf pulses have been applied to the system a steady state situation is achieved where the magnetization prior to each rf is equal to that at t = TR. The velocity distribution, TR and the slice thickness dictate the number of rf pulses required to attain steady state for this system. The TE used must be short to minimize signal decay due to T_2^*.

The signal acquired from a voxel, normalized with respect to the factor $M_0 e^{-TE/T_2^*}$ can be written as

$$S_{blood} = \left[A + B \sum_{j=0}^{N} \omega_j \varepsilon^j \right] \sin \alpha \qquad 4.9$$

As $N \rightarrow \infty$, the blood signal approaches steady state.

From eq. 4.9, it can be seen that the un-normalized resultant blood signal from a given voxel is a function of the flip angle α, T_1, T_2^*, TR and TE used as well as the velocity distribution, and the slice thickness. The geometry of the blood vessel within the

slice is important. However here only a perpendicular geometry is considered.

If the signal from a bolus of blood is plotted as a function of the number of rf pulses it experiences (see fig. 4.2) for a given α, an asymptote towards the steady state signal is observed, which corresponds to the A term in eq. 4.8. Since muscle and blood have similar relaxation properties and proton densities, then A also corresponds to the signal contribution from tissue. The TOF contrast is determined by

$$C = S_{blood} - S_{tissue} = B \sum_{j=0}^{N} \omega_j \varepsilon^j \sin \alpha \qquad 4.10$$

The above equation shows that maximization of the contrast over the boundary will depend on optimizing the imaging parameters.

4.2.2 Boundary Signal Simulation for TOF

Since the topic of interest is the contrast at the vessel boundary, the simulations have to be done for all the voxels that are so designated. We have chosen to define a boundary voxel as one that includes the vessel circumference. The signal is calculated for a chosen TR and T_1 (obtained from an estimate of the typical value for blood).

The simulation categorizes the inflowing boli of blood within a voxel depending on the number of rf pulses they have experienced. The fraction of blood within a boundary voxel will depend on how much of the voxel is within the vessel. For a typical situation such as that shown in fig. 4.3 the fraction of blood that has experienced j or fewer rf pulses is given by

$$\rho_j = \int_{y_1}^{y_2} \int_{x_1}^{\sqrt{r^2 - y^2}} z(x,y)\, dx\, dy \qquad 4.11$$

where $z(x,y) = 2\, v_m\, (j + 1)\, TR\, (1 - \frac{(x - x_c)^2}{r^2} - \frac{(y - y_c)^2}{r^2})$.

Therefore the fraction of spins that have seen j pulses is

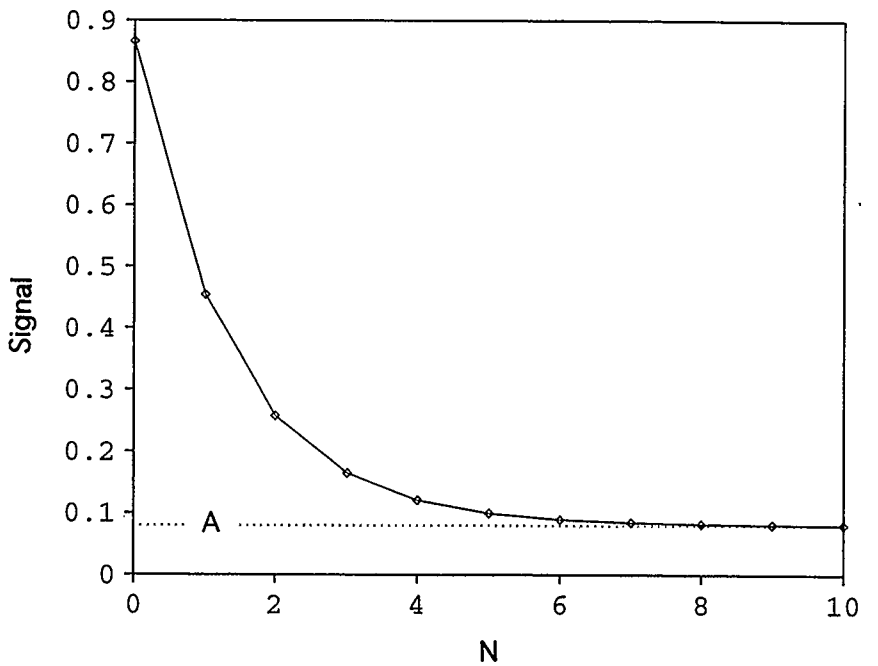

Figure 4.2 A plot of signal vs. the number (N) of rf pulses ($\alpha = 60^0$) a bolus of blood experiences. As N increases the blood becomes progressively more saturated, therefore the blood signal is asymptotic to a steady state value which corresponds to the A term of eq. 4.8.

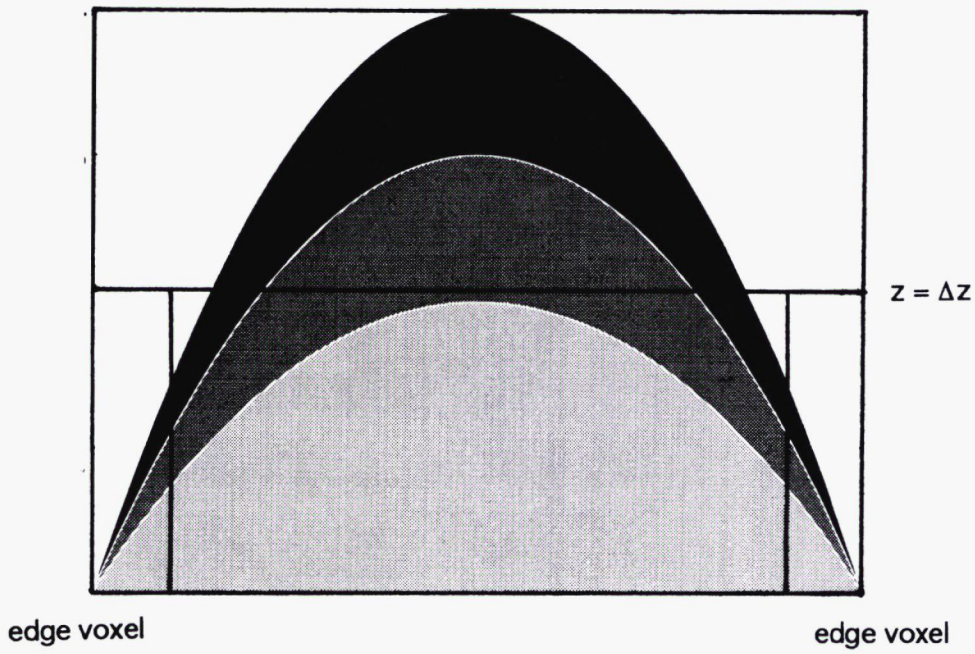

Figure 4.3 Cross-section of the vessel taken in the xz plane:

fraction of spins in the edge voxels that have experienced N+1 rf pulses

those that have experienced N rf pulses

those that have experienced N-1 or less rf pulses.

$$\omega_j = \rho_j - \rho_{j-1} \qquad 4.12$$

where the sum of ω_j approaches the volume of the voxel as $j \rightarrow \infty$.

To calculate the boundary signal the simulation requires the vessel radius (see fig. 4.4), the vessel centre co-ordinates (to obtain the co-ordinates of all the boundary voxels $\{voxels_1\}$), a given average velocity and the imaging parameters. If the slice thickness is denoted by Δz, and a section of the paraboloid from $z = 0$ to $z = \Delta z$ is removed, the resultant new paraboloid represents the spins that have left the slice. The circle at the base of this paraboloid of radius r' in the $z = \Delta z$ plane can be used to calculate a new set of voxel co-ordinates $\{voxels_2\}$. For each voxel co-ordinate in the set $\{voxels_2\}$, the set $\{voxels_1\}$ is checked to find a match. If a match is found then the fraction of the spins within that boundary voxel that have seen j or fewer pulses is given by

$$\rho_j = \int_{y_1}^{y_2} \int_{x_1}^{\sqrt{r^2 - y^2}} z(x,y)\, dx\, dy - \int_{y_1'}^{y_2'} \int_{x_1'}^{\sqrt{r^2 - y^2}} z'(x,y)\, dx\, dy \qquad 4.13$$

where the primed system belongs to the $\{voxels_2\}$, and

$$z'(x,y) = (2\, v_m\, (j + 1)\, TR - \Delta z)\, (1 - \frac{(x - x_c)^2}{r^2} - \frac{(y - y_c)^2}{r^2}) \qquad 4.14$$

The resultant contrast for each voxel is given by substituting eqs. 4.11 to 4.14 into eq. 4.10. The simulation is performed for the range $\alpha = 0^0$ to 180^0 in order to find the optimal value of α.

4.3 Phase-Contrast Angiography

PC techniques use the additional phase shift accrued by moving spins through an applied gradient to image flow. PC techniques also result in under-estimation of the vessel width if a velocity gradient is present at the vessel boundary such as that seen in

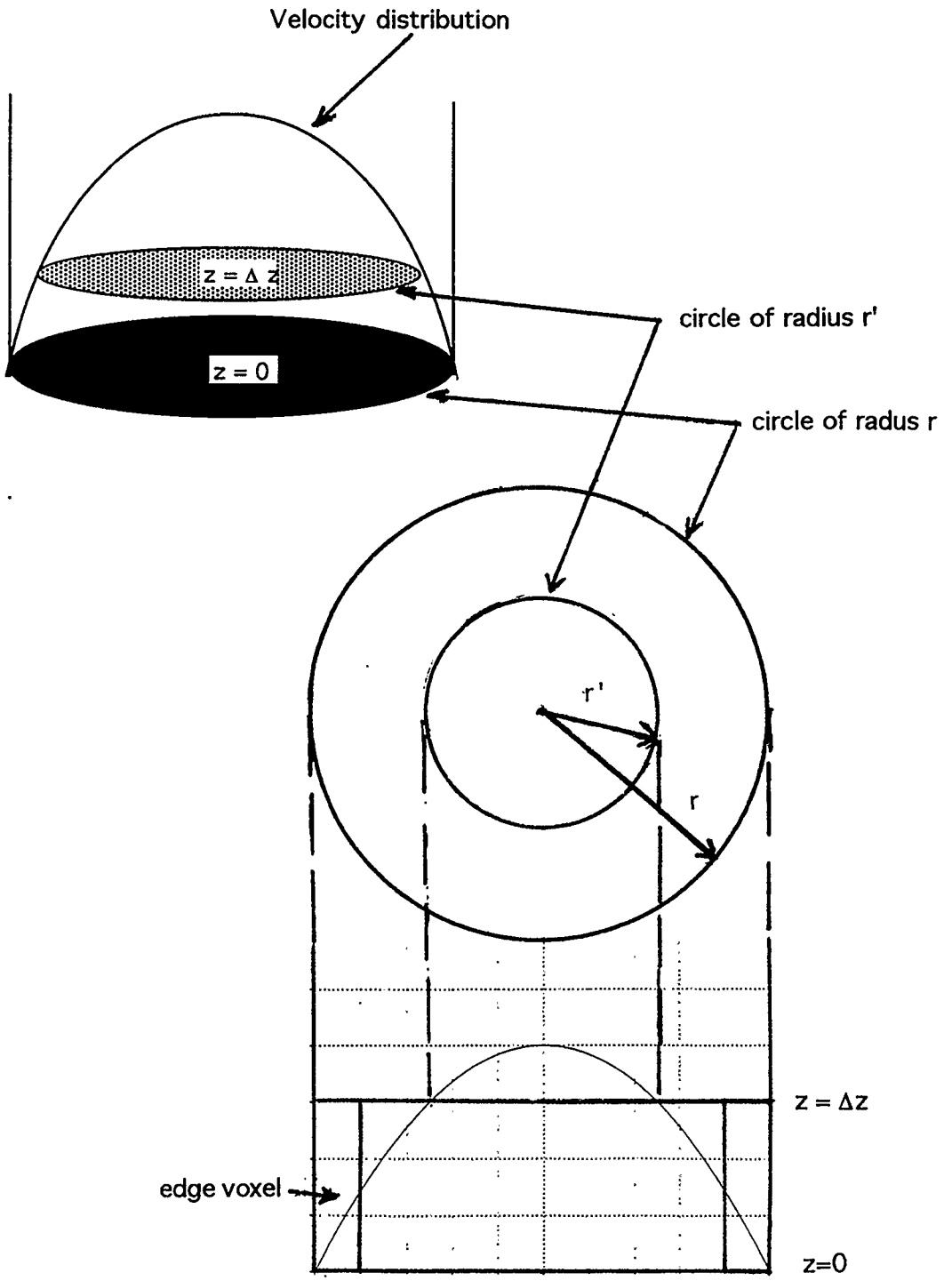

Figure 4.4 Cross-section taken in the xy plane at z=0 and z=Δz of the paraboloid, showing the circles of radius, r and r'.

laminar flow (fig. 4.1b). Application of a magnetic gradient on spins of varying velocities results in phase dispersion of the spins within the voxel, referred to as intravoxel dephasing. The signal from the voxel is a function of the vectorial addition of the spin phases, therefore the signal decreases with increasing intravoxel dephasing. The TOF effect is inherent to motion and is present in PC angiography, so that both slow flow and the velocity gradient present at the vessel boundary result in under-estimation of the vessel width.

PC methods require that the amount of phase imparted to a spin be readily controlled, which is accomplished by adding more gradients, i.e. flow encoding gradients, to the pulse sequence [42]. Flow compensating gradients are also added to the pulse sequence to cancel the phase shift accrued by moving spins during the application of the other imaging gradients. Flow compensation is explained in the following section and flow encoding is explained in section 4.3.2.

4.3.1 Effect of Gradients on Flowing Spins

As noted in the preceding section the application of the field gradients causes phase incoherence of the spins, in addition to that caused by T_2 relaxation. This effect is exploited to obtain spatial information from the sample. A spoiled GRE (fig. 2.5) is used to illustrate the phase incoherence of moving and stationary spins.

The effect of the read gradient on stationary spins (section 2.3.1) is examined in more depth here. It is seen from fig. 4.5 that gradient dephasing occurs during the time $t = -2\tau$ to $t = -\tau$ when the negative lobe of the gradient is applied. The phase acquired due to this gradient, by a spin at position at time $t = -\tau$ is given by

$$\varphi_d = - \gamma G_x x \tau \qquad 4.15$$

During the application of the positive lobe of the gradient the spins rotate in the opposite direction, therefore spin rephasing occurs from $t = -\tau$ to $t = 0$. The phase acquired by

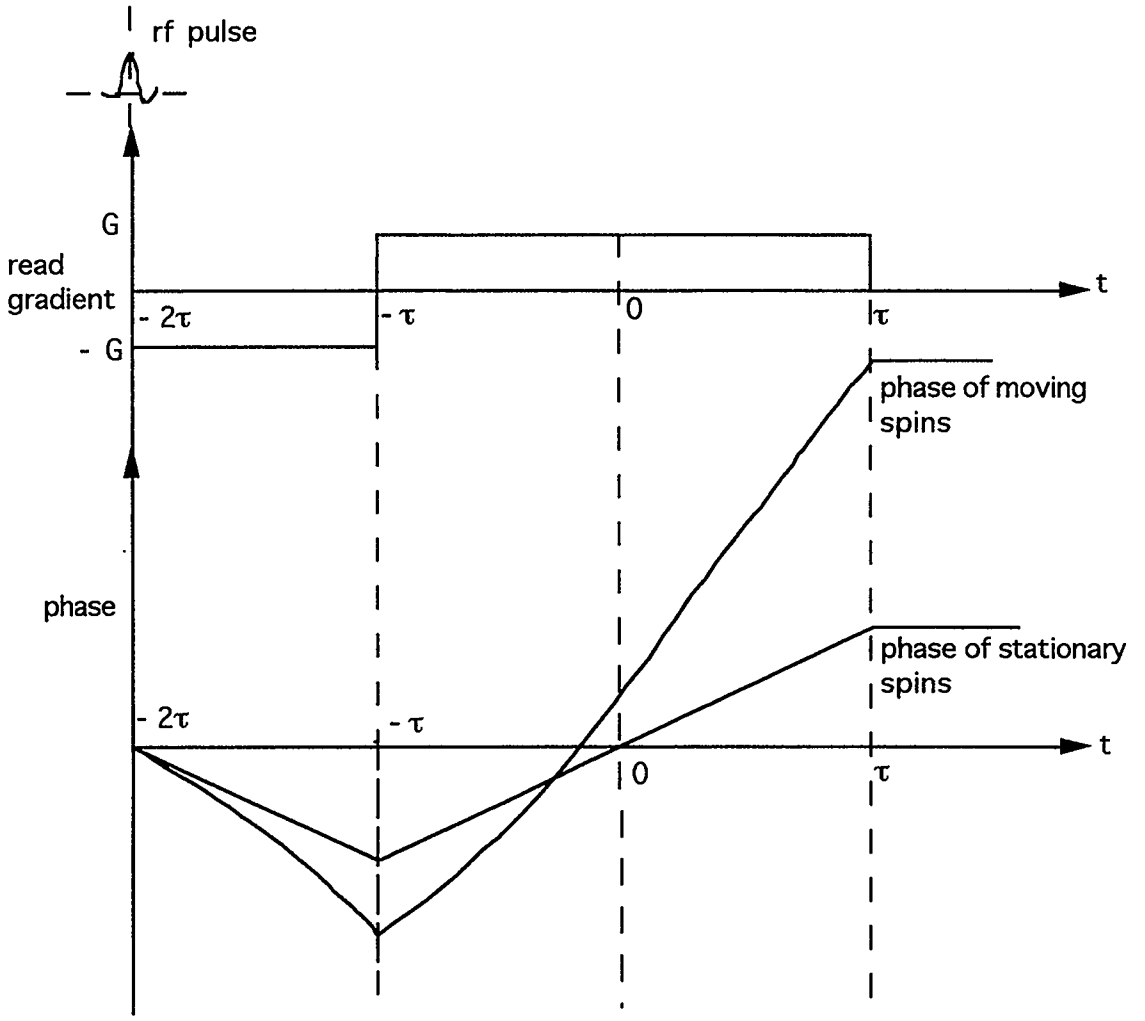

Figure 4.5 Plot of the phase of stationary and moving spins (v= constant), depicting the dephasing rephasing action of the read gradient. At t = 0 all the stationary spins are refocused at the echo centre, but the moving spins show a velocity dependent phase shift.

the spin at t = 0 due to this rephasing gradient is

$$\varphi_r = \gamma G_x x \tau \qquad 4.16$$

Hence the total phase acquired at this time is

$$\varphi_d + \varphi_r = -\gamma G_x x \tau + \gamma G_x x \tau = 0 \qquad 4.17$$

therefore the spins are completely refocused at the echo centre.

Moving spins present a more complicated problem since the position of the spins is now changing in time. The gradient induced phase shift is

$$\varphi(t) = \gamma \int_{t_1}^{t} G_x(\tau)\ x(\tau)\, d\tau \qquad 4.18$$

If the flow is assumed to be in the x direction only, where $x(t) = s + vt + 1/2\ at^2 + \ldots$, then phase can be written as

$$\varphi(t) = \varphi_s(t) + \varphi_v(t) + \varphi_a(t) + \cdots \qquad 4.19$$

To further simplify the situation, assume that the flow is of constant velocity v. Let t = 0 be defined as the time at the echo centre then at some time t, the position of the spin is s + vt. The effect of the read gradient on such a spin is derived as

$$\varphi(t) = \gamma G_x \left(s t + v \tau^2 + \frac{1}{2} v t^2 \right) \qquad 4.20$$

The velocity dependent terms in the above equation each have their own separate effects on the moving spins. The term $v\tau^2$ causes a phase deviation at the echo centre and the last term $1/2\ vt^2$ leads to spatial frequency filtering [38]. The $v\tau^2$ results in signal loss due to intravoxel dephasing, since the flowing spins present in the slice will not be completely refocused at the echo centre.

The solution to this problem is to introduce flow compensation gradients [13] into the GRE (fig. 4.6). Flow compensation requires the use of additional gradients placed either in the slice select direction or the frequency encoding direction or both, according to the direction of flow. No such gradients are placed in the phase encoding direction because the effect of this gradient on the moving spins simply results in a shift in

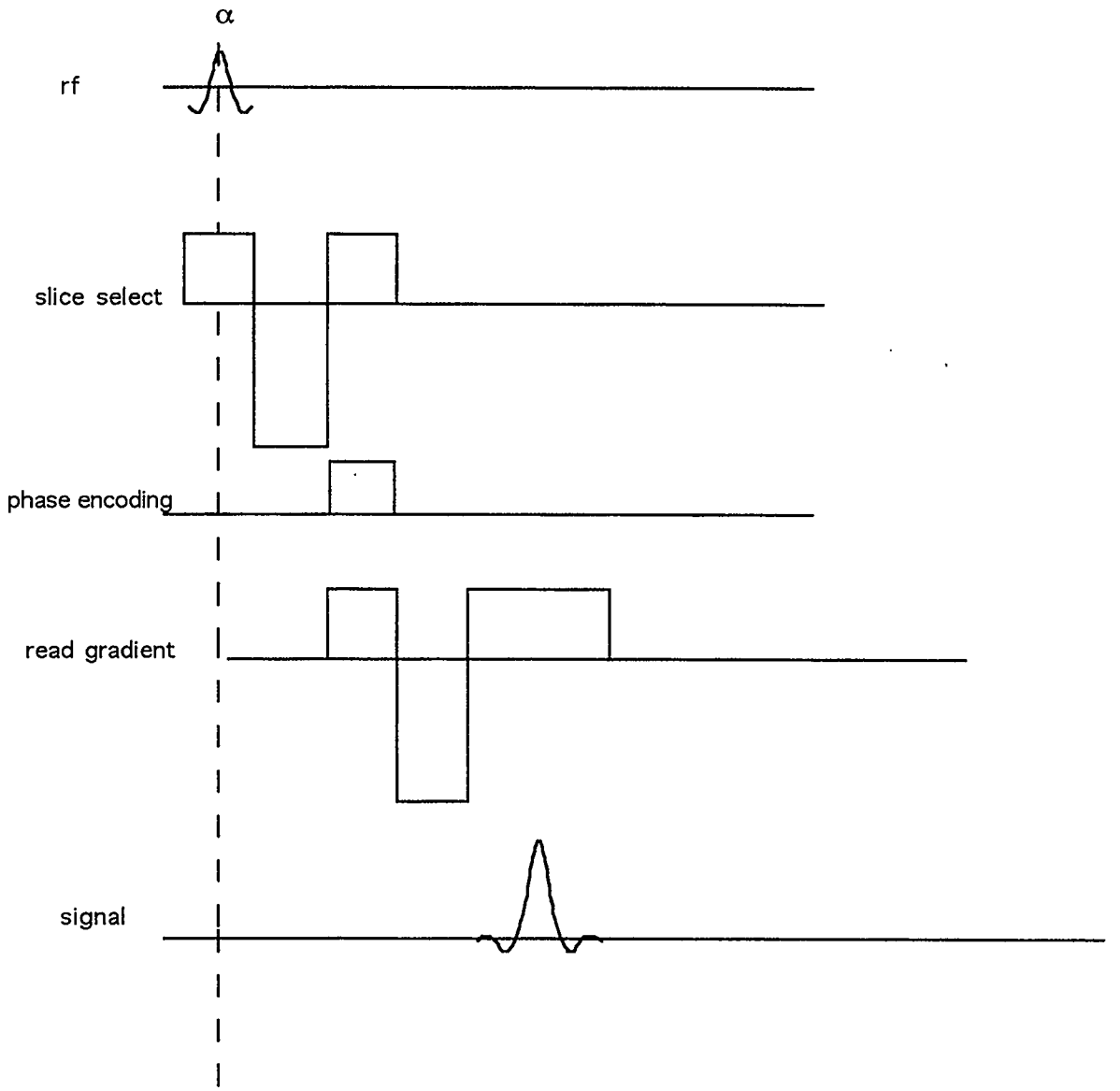

Figure 4.6 Schematic timing diagram of a flow compensated GRE sequence. Flow compensation gradients have been added in the read and slice select directions. The pulse is first moment nulled or velocity compensated.

apparent position.

Flow compensated pulses are designed to null the orders of the gradient moment greater than the zeroth order, which in eq. 4.19 are represented by the term φ_v (t) and any higher order terms present in the series. A particular moment is said to be nulled if it satisfies

$$\int_{o}^{TE} G_x(t) \; t^n \, dt = 0 \qquad 4.21$$

where n is the corresponding order of the Taylor series. If the flow is one of constant velocity, as in the preceding example, then only first moment nulling is required and the GRE that accomplishes this is said to be velocity compensated. A common solution is to use a gradient waveform, whose lobes have the same duration but with amplitudes in the ratio 1:-2:1.

If higher order terms such as acceleration are present, and the sequence is velocity compensated, then there is an increase in the phase shift accrued due to the acceleration, compared to that accrued if the compensating gradients were not present.

Compensation of higher order terms requires additional gradient lobes, whose area ratios can be obtained from the coefficients of the binomial series $(1 - a)^{n+1}$, where n is the order of the term. In actual practice, compensation is only possible for a small number of terms.

A vicious cycle develops as the higher order terms become more significant in the Taylor series expansion. As more gradient lobes are added to null to higher orders, the echo time TE has to increase to accommodate them. As the TE is increased, more of the higher order terms in the Taylor expansion become significant, creating the need for even higher order nulling.

Flow compensation is utilized to decrease the intravoxel dephasing caused by motion during the application of the slice select and read gradients. Therefore flow

compensated sequences are used in the TOF as well as the PC techniques.

4.3.2 Flow Encoding

Whereas the TOF technique relies on longitudinal magnetization for velocity signal enhancement, the PC technique uses the transverse magnetization since it relies on the phase shift accrued due to motion along a field gradient. As mentioned before, to control the amount of velocity induced phase shift, flow encoding gradients are added to the pulse sequence. These gradients are added in the direction of flow and are bipolar, with zero total summed area [42]. In the case where the flow occurs only along the z direction, the gradient waveform is added to the slice select gradient. The total phase accrued for a spin moving with constant velocity, during application of a square lobed bipolar gradient of amplitude G_z (amplitude ratio 1:-1) and period 2τ, is $\gamma G_z v \tau^2$. The phase shift is directly proportional to the velocity as required. Phase proportionality can be achieved for any term in the Taylor series. This obviously requires the use of additional gradient lobes.

If a velocity shear is present, as in the case of laminar flow, an increase in the flow encoding gradient results in a proportional increase in the phase distribution across a voxel, and consequently an increase in intravoxel dephasing.

4.3.3 Complex Subtraction

The complex subtraction (CS) processing method requires two data sets (or two images), with the bipolar flow encoding gradient inverted in the pulse sequence for the second acquisition. Therefore the phase shift accrued by the moving spins in the two images will have opposite signs, while those of the stationary spins will be unchanged. The signal from the first acquisition can be written as $S_1 = S_{tissue} + S_{blood}\, e^{i\phi}$ and that of the second acquisition as $S_2 = S_{tissue} + S_{blood}\, e^{-i\phi}$. The complex difference of the

signal is given by

$$\Delta S = 2\ i\ S_{blood} \sin \phi \qquad 4.22$$

where it is seen that the static tissue signal has been subtracted out (see fig. 4.8). The contrast for the CS method is calculated directly from eq. 4.22 where S_{blood} is computed from eq. 4.9, and represents the inherent TOF effect present in the CS technique.

As the CS method uses two acquisitions compared to the one acquisition needed for the TOF method, the contrast obtained must be divided by 2 if a fair comparison between the two methods is to be made.

4.3.4 Boundary Signal Simulation for CS

Computer simulation for the CS method is very similar to the TOF simulation, except that now there is the additional phase shift from the velocity encoding gradients. The phase distribution for laminar flow is given by

$$\phi(x,y) = 2\ \phi_0\ \left(1 - \frac{(x - x_c)^2}{r^2} - \frac{(y - y_c)^2}{r^2}\right) \qquad 4.25$$

where ϕ_0 is the phase accrued by spins at the average velocity due to the velocity encoding gradients.

Referring to eq. 4.9 and 4 .10 the contrast is given by

$$C = \iint \left[A + B \sum_{j=0}^{N} \Delta z_j\ (x,y)\ \varepsilon^j \right] \sin \phi(x,y)\ \sin \alpha\ dx\ dy \qquad 4.24$$

Recall that in the TOF technique, the steady state term A also corresponds to the signal from stationary tissue and must therefore be subtracted out in eq. 4.10. However the contribution of this steady state term appears here because in the CS technique the static tissue signal is zero.

Since ΔS is purely imaginary in eq. 4.22 the signal is given by the y-component of the xy magnetization summed over the whole voxel. Eqs. 4.11 to 4.14 are now modified to include both the $\sin(\phi(x,y))$ term and the steady state term. So eq. 4.11

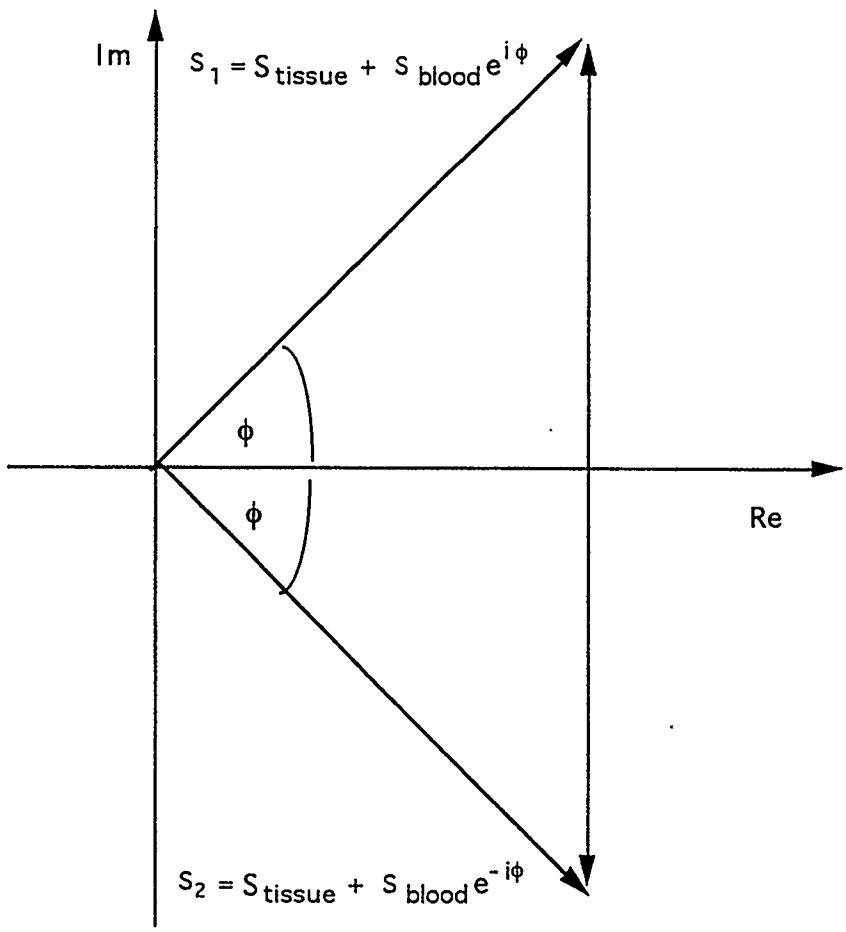

Figure 4.7 The graphical representation of CS in the complex plane. Here it is obvious that the signal contribution from the static tissue is subtracted out in the complex difference image.

becomes

$$\rho_j = \int_{y_1}^{y_2} \int_{x_1}^{\sqrt{r^2 - y^2}} \sin \phi(x,y)\ z(x,y)\ dx\ dy \qquad 4.25$$

The above integral has to be calculated numerically as it has no analytic solution .

As the flow encoding gradient and hence ϕ_0 is increased, the contrast must reach a maximum, after which intravoxel dephasing becomes the dominant effect. There is therefore an optimal net phase shift that can be accrued by a voxel corresponding to the maximum signal attainable from that voxel. Hence both the tip angle and the phase imparted by the flow encoding bipolar gradients have to be optimized for a given average velocity for the CS method. Optimization of these parameters is performed for the total boundary contrast.

4.3.5 Phase Subtraction

In this method two data sets are acquired in the same manner as that of the CS method, and a phase subtraction (PS) is performed. The pixel signal on the resultant phase difference image is given by

$$\Delta\varphi = \arg S_1 - \arg S_2 = \arg \frac{S_1}{S_2} \qquad 4.26$$

where S_1 and S_2 are the respective complex signals from the two data sets. Here arg S_1 and arg S_2 are calculated from the signal received from the in-phase and out-of-phase receiver channels.

$$\arg S = \tan^{-1} \frac{S_{im}}{S_{re}} \qquad 4.27$$

If the real and imaginary data sets are assumed to have equal and uncorrelated noise of standard deviation σ, then the standard deviation in the phase is

$$\sigma_\phi = \frac{\sigma}{|S|} \qquad 4.28$$

the derivation of which is found in Conturo and Smith, 1990 [9] (see fig. 4.9). The SNR

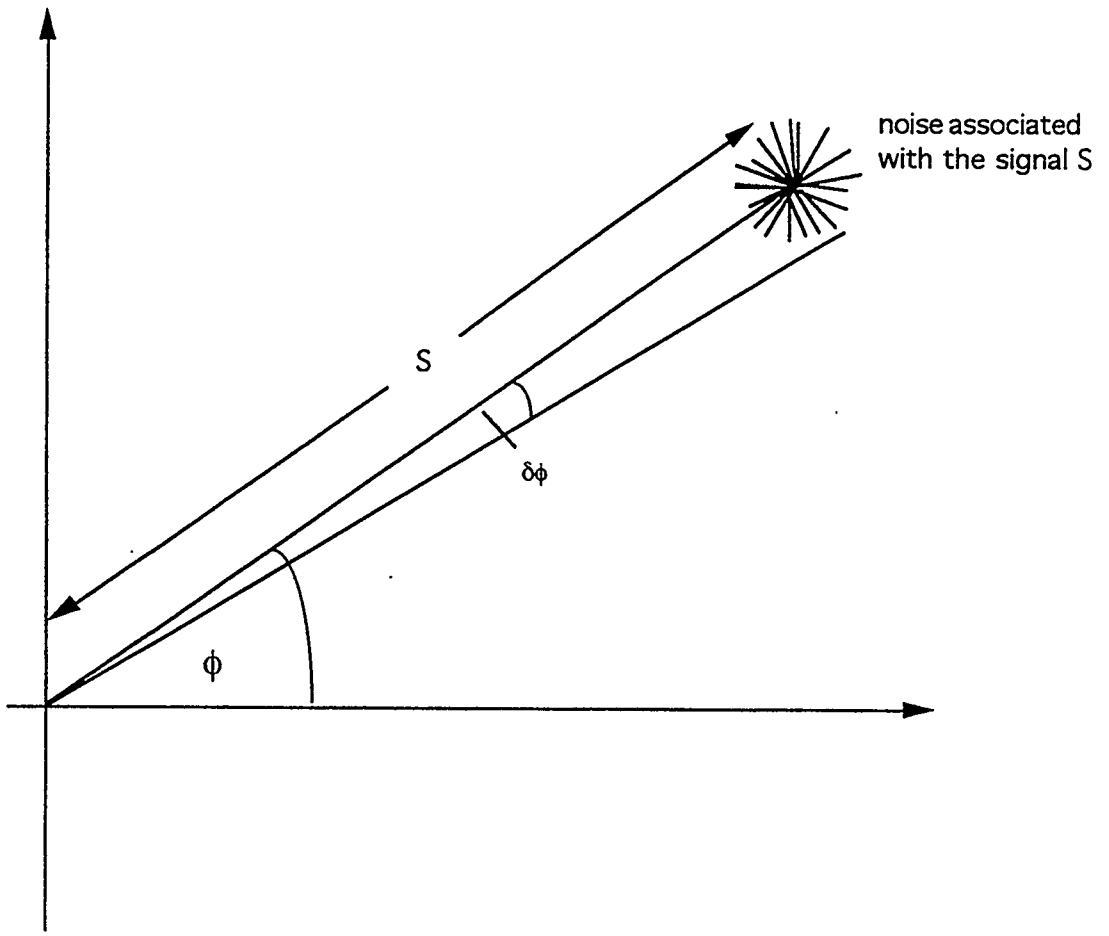

Figure 4.8 A graphical view of the signal from one of the two images in the PS data set, which shows that the noise in the phase is given by eq. 4.28.

for a phase image is

$$\mathrm{SNR} = \frac{\Delta\phi}{\sigma_\phi} = \frac{\Delta\phi\,|S|}{\sigma} \qquad 4.29$$

If the PS image signal is divided by 2 in order to normalize to a single acquisition and as the static tissue directly subtracts out, then the CNR is given by

$$\mathrm{CNR} = \frac{\Delta\phi\,|S|}{2\sigma} \qquad 4.30$$

and the contrast is calculated in the PS simulation as $\Delta\phi|S|/2$.

4.3.6 Simulation of Boundary Signal for PS

The simulation of PS is similar to that of CS except in this case both the x and y components of the xy magnetization are used to calculate the phase of the resultant magnetization. The x component is calculated using modified versions of eqs. 4.24 and 4.25, i.e. a substitution of the cosine term for a sine term. The magnitude and phase of the resultant magnetization within the pixel is obtained using trigonometry.

CHAPTER 5

COMPARISON OF THE CNR BETWEEN THE TOF AND PC METHODS

The aim of this work is to compare the CNR of the TOF, CS and PS methods at the vessel boundary, and in so doing provide a guideline of the best tip angle and flow phase encode gradient to use. Computer simulations were performed, as was explained in the last chapter, to find theoretically the optimal tip angle and the flow induced phase as a function of velocity and to predict the behaviour of the contrast. A comparison of the simulated data to that obtained from experiments was done to assess the validity of the theory. This required a flow phantom, a means of generating laminar flow and a choice of fluid. Imaging was performed on a 1.5 T magnet, the GE Signa Advantage Imager (GE Medical Systems, Milwaukee), using the standard head coil.

5.1 Experimental Setup

The fluid used was a mixture of glycerol and water in a ratio of 1:8 by volume. Copper sulfate ($CuSO_4$), 0.3539 mg per litre mixture, was added as a dopant to lower the T_1 value to mimic that of blood. The viscosity of the mixture was chosen on the basis of its performance in minimizing the problem encountered with air bubbles, while attempting to keep the amount of glycerol and $CuSO_4$ required low. These separate from the solution readily. The measured T_1 was 1155 ± 76 ms compared to 1000 ms used in the simulations.

The flow phantom consisted of a flexible polyethylene tube in which was inter-spliced a 3.5 m length of inflexible tubing which allowed lamina flow to develop. The inner diameters of both tubes were approximately 0.953 cm. A sketch of the phantom's placement in the magnet is shown in fig. 5.1. The diagram shows a bottle filled with

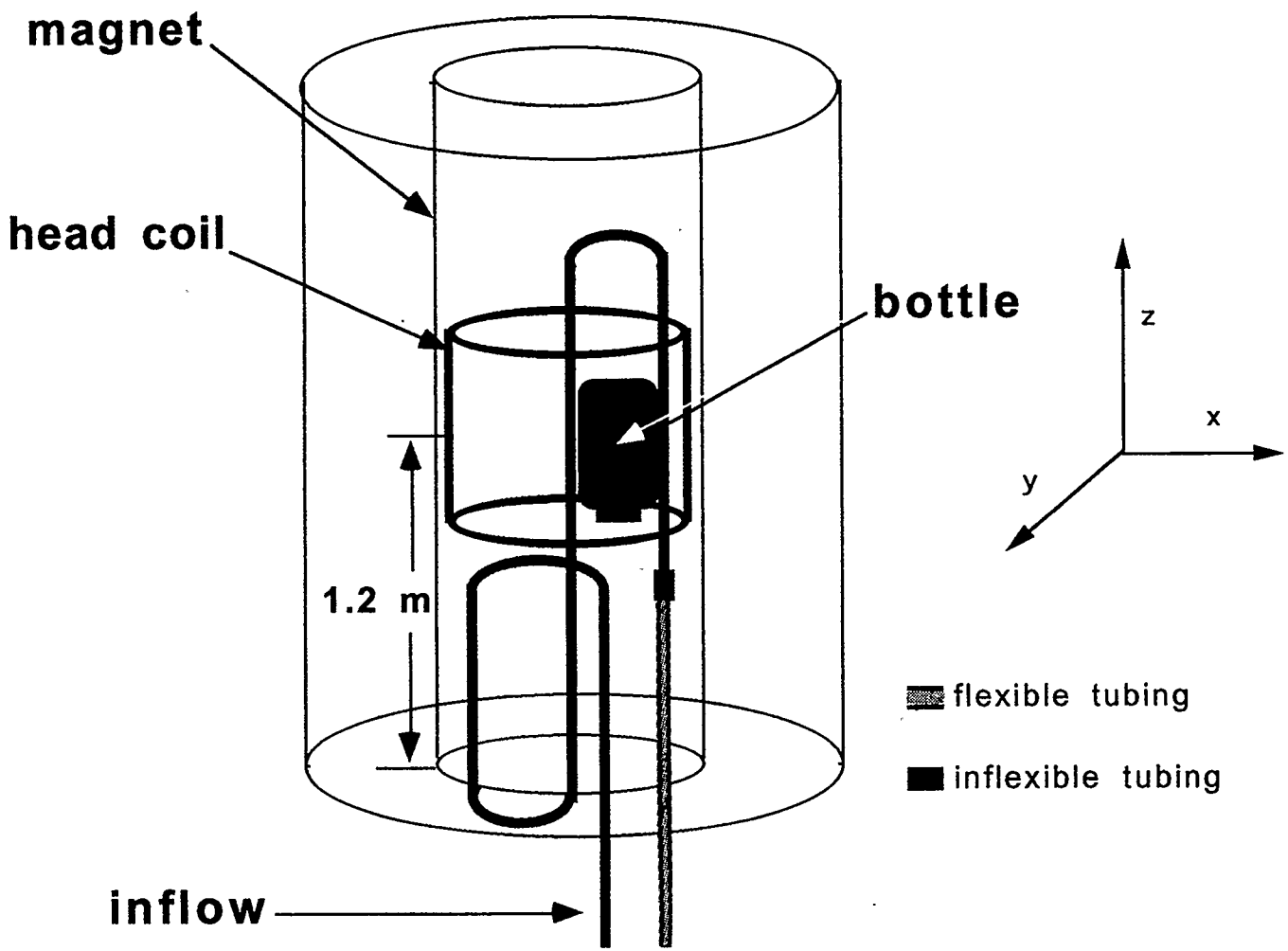

Figure 5.1 The arrangement of the tubes in the magnet. The imaged site is located at the centre of the head coil.

doped water which was secured between the U shaped curve of the tube in the head coil.

The bottle was used to set the resonance frequency and flip angle for the rf pulse, and was also used as a reference signal for phase correction. The imaging plane is in the xy direction (z is along the bore of the magnet), so the resulting axial image is a transverse cross-section of the set-up, as shown in fig. 5.2. The tube on the left in the image contained the inflow to the magnet and was the one on which the analysis was performed. This arm of the tube is referred to here as the inflow tube. Its position in the head coil, was kept within 1 mm for all experimental runs.

The inflow tube was looped once within the bore of the magnet (fig 5.1), so that inflowing spins spend at least 3 s (approximately equal to 3 T_1) in the field, prior to imaging. This was to allow the magnetization to reach equilibrium. The distance traveled to accomplish this was approximately 3 m.

Gravity feed was utilized to generate the flow. The expected flow profile at the imaged site was parabolic. This was developed by having the flow move through a straight length of 1.2 m of the inflexible tubing just upstream from the selected slice (fig 5.1). To confirm the shape of the flow profile, imaging was performed using a modified SE sequence (see fig. 5.3). This gradient pulse sequence was written by Dr. A. P. Crawley.

In this sequence the slice select gradient was placed in the same direction as the read out gradient, i.e. along the flow direction, and a selective 180^0 gradient pulse was applied orthogonal to the slice and phase encode direction. As a result, the tagged spins are the only ones that register a signal. A long TE was used to increase the height of the parabola, by allowing the tagged spins enough time to exit the slice.

The time taken to collect a volume of 1 litre of fluid was measured using a stopwatch in order to calculate the flow rate. Readings were taken both before and after image acquisition.

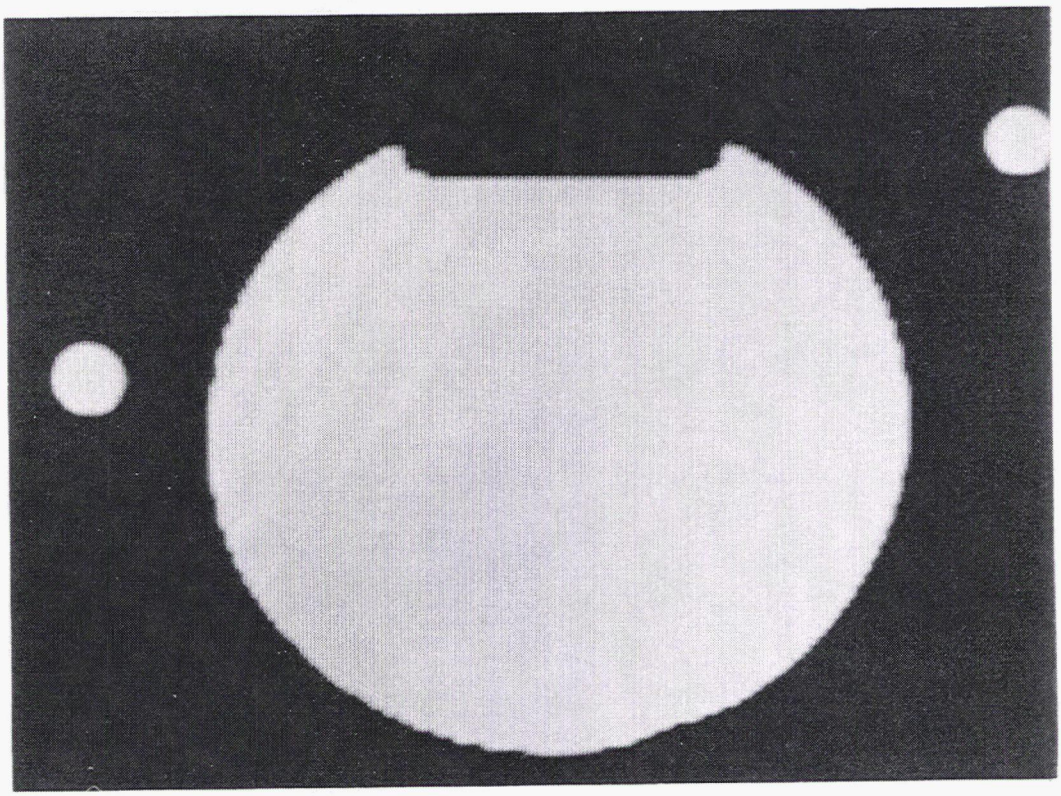

Figure 5.2 Axial image of the tube and bottle. The tube shown on the left is the one used in image analysis.

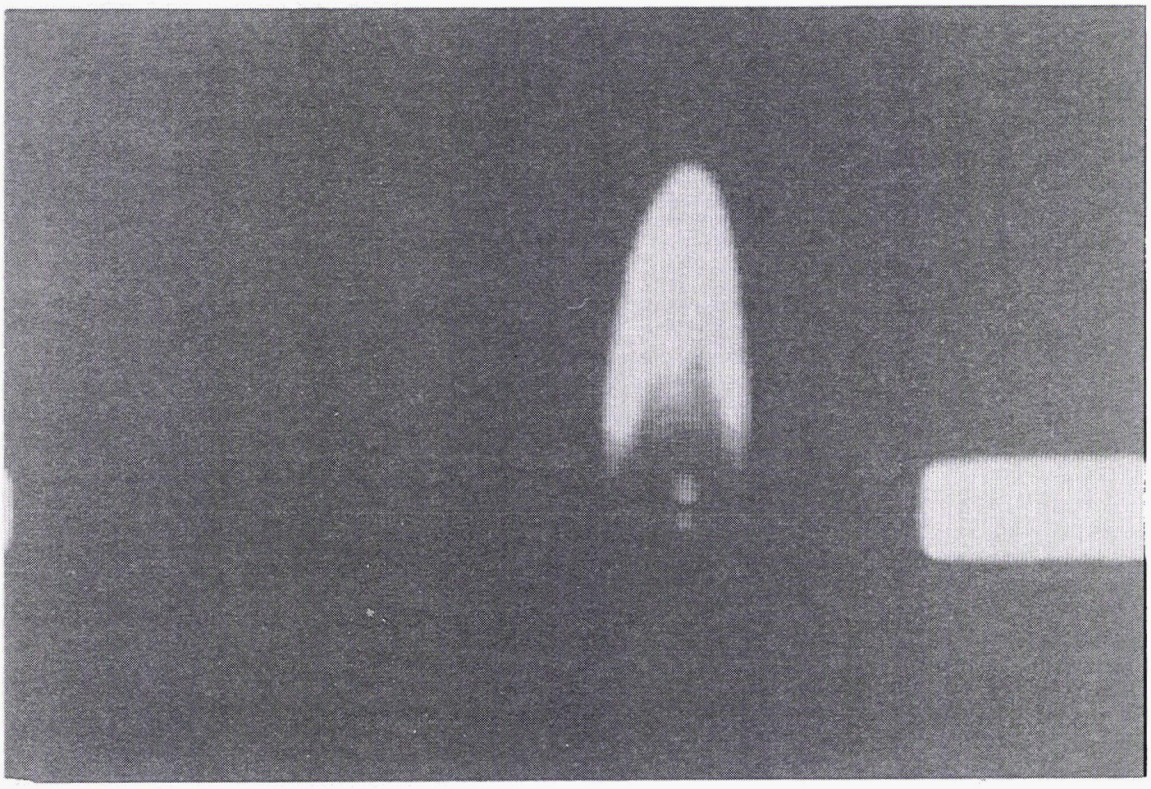

Figure 5.3 Parabolic flow profile obtained using the modified SE sequence.

5.2 Pulse sequences

The TOF images were obtained using a standard flow compensated spoiled GRE sequence, with a FOV of 26 cm, a 256 X 256 imaging matrix, slice thickness of 5 mm, 8 NEX (where NEX refers to the number of excitations or number of averages), a TR of 50 ms and a TE of 25 ms. The time per acquisition was 1.43 s. The choice of 8 NEX produced adequate SNR in a reasonable scan time. With a FOV of 26 cm the vessel diameter was 10 voxels across. This is typical for blood vessels in-vivo, and corresponds to the simulated data. Reconstruction of the images was performed simultaneously with acquisition using the software available on the Signa.

The PC images were obtained using a modified flow compensated GRE sequence (modification of the pulse sequence program was written by Dr. A. P. Crawley), in which a bipolar velocity encoding gradient was applied along the z direction. The resultant raw data, composed of the pixel signal components from the in-phase and out-of-phase receiver channel, can be processed using either PS or CS (see sections 4.3.3 and 4.3.5). Both of these methods produce a different resultant image. As two images are needed for subtraction, fair comparison of the CNR at the boundary obtained from PC to that from the TOF technique requires that two 4 NEX images be used. The final subtracted image would be the equivalent of an 8 NEX image. The two 4 NEX images were obtained in an interleaved fashion, where one line of data was collected for the first image, the bipolar gradient inverted and the equivalent line for the second image acquired. Therefore the two images were obtained simultaneously from one acquisition of 1.43 s. Image reconstruction of the PC data was performed on a Sun Sparc 2 (Sun Microsystems Inc.), as the Signa does not have a software package available for reconstruction of PS images.

The base algorithm that was used in the reconstruction of the PC images was supplied by Dr. A. P. Crawley. This algorithm separated the interleaved data into two

images and performed a 2D-DFT on the data to convert the raw data into an image.

The bipolar gradient used was one cycle of a sine wave, so from eq. 4.18 , the phase imparted to the peak velocity is given by

$$\phi = 2\, v_m \gamma A \int_0^T t \sin(2\pi t/T)\, dt \qquad 5.1$$

where A and T are the operator selected amplitude and period of the sine wave. The amplitude ranges from 0 - 1 Gauss/cm, limited by the system's hardware. Because the flow phase encoding gradient is applied in the time available between the end of the flow compensated slice select gradient and the start of data acquisition, there is also a limit to the period of the gradient.

5.3 Image Analysis

The position of the tube centre in the image needed to be ascertained in order to locate the edge pixels. This was accomplished by evaluating the weighted mean of the pixel co-ordinates with the weighting factor being the pixel signal. An image of the tube with no flow, i.e. a static image, was used since the signal is expected to be evenly distributed within the tube. Following is a description of the algorithm used to locate the tube centre.

First, an estimate of the centre was determined on the first pass of the program, using the co-ordinates of a 20X20 pixel square in the area of the image containing the inflow tube but excluding the reference bottle. The means were calculated in the x and y directions, to obtain an estimate of the centre co-ordinates. This centre was used to evaluate the weighted mean of pixels located along a series of radial lines passing through the first estimate of the tube centre. The radial lines were chosen to be 14 pixels in length and at 10^0 intervals from each other. These estimates were averaged and used as

the input for a final pass through the algorithm.

Static images were taken at the beginning and end of a run. The centre co-ordinates from these static images were also averaged to produce a final estimate of the centre used in the analysis the flow images from the run. On fig. 5.4 the edge pixels for a typical value of the tube centre are highlighted. It can be seen that there are a lot of partial edge pixels present.

5.3.1 CNR Measurements

Using the assumption that blood and its surrounding tissues have the same T_1 (~ 1 s), an experimental measurement of the TOF contrast was obtained by subtracting the static ROI from the flow ROI. It can be argued using the definition of the CNR from chapter 2, that an equivalent subtracted ROI could be taken from the static reference bottle in the flow image. This was not done as the fluid within the bottle does not have the same T_1. Additional errors would also have been added when normalizing the signal to correspond to the contrast for a the single pixel. Therefore the contrast for the TOF is calculated as

$$C_{pixel} = \sum_{i=1}^{N} S_{vi} - \sum_{i=1}^{N} S_i \qquad 5.2$$

where N is the number of edge pixels, S_i is the static signal, and S_{vi} is the corresponding flow signal from the ith pixel in the image.

In the PC methods the static tissue signal is explicitly subtracted out, so the contrast can be directly measured experimentally from the flow signal obtained. It should be noted that this method does not include any measurement of imperfect subtraction of the static signal due to possible phase instability. Phase instabilities can occur in the images due to eddy currents or to phase instability in the quadrature channels. The CS contrast from the complex difference image is given by

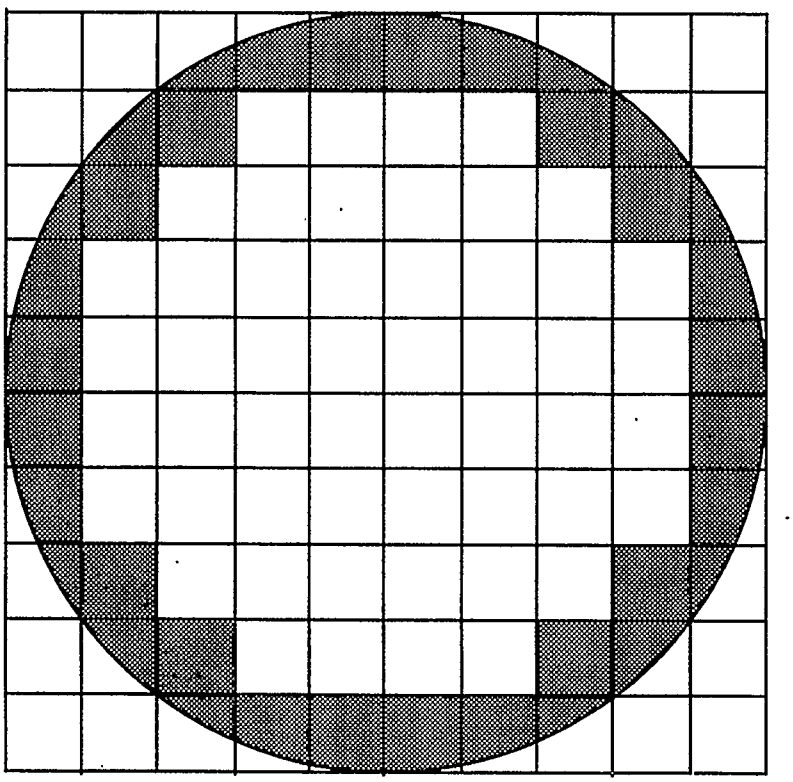

Figure 5.4 A cross-sectional view of the tube with the edge pixels highlighted.

$$C_{pixel} = \sum_{i=1}^{N} S_{vi} \qquad 5.3$$

where S_{vi} represents the pixel magnitude from the ith pixel. In the case of PS, the contrast is

$$C_{pixel} = \sum_{i=1}^{N} S_{vi}\,\phi_{vi} \qquad 5.4$$

where $S_{vi}\ \phi_{vi}$ is the magnitude weighted phase from the phase difference image.

An evaluation of the contrast in these images says little on its own without some knowledge of the background noise. Therefore to compare the experimental performance of the PC and TOF methods, the CNR is evaluated.

The noise for the TOF and CS methods can be measured directly from any background ROI in a flow or static image [42]. However in order to make the measurements similar to that required for the PS the edge ROI was again chosen, as noise in the background of a phase image is meaningless, since it is random over the range (0 - 2π). Measurements of the noise were obtained using a set of 15 static images, all taken from the same experimental run and have the same imaging parameters. It is expected that the standard deviation in the signal per pixel would be a measure of the noise in the image. The noise for the TOF and the CS methods was calculated using

$$\sigma_0 = \sum_{i=1}^{N} S_i\,\sigma_i \qquad 5.5$$

where S_i is the mean and σ_i is the unbiased estimate of the standard deviation in the signal of the ith edge pixel obtained from the 15 static images.

The noise evaluation for the PS method requires the reconstruction of magnitude weighted phase images as well as magnitude images. In this case the noise was calculated using

$$\sigma_0 = \sum_{i=1}^{N} S_i\,\sigma_{\phi i} \qquad 5.6$$

where S_i is the mean obtained from magnitude images, and $\sigma_{\phi i}$ is the standard deviation of

the magnitude weighted phase of the ith pixel.

The CNR is defined as

$$CNR = \frac{C_{pixel}}{\sigma_0} \qquad 5.7$$

5.4 Results

The theoretical results were obtained over a range of average velocities between 0 - 100 cm/s. The experimental velocity range examined was from 2 - 81 cm/s, which was dictated by the limits of the gravity feed set-up.

5.4.1 Optimal Tip Angle

Since all the methods rely on flow signal enhancement due to the TOF effect, the optimal CNR of the vessel boundary is dependent on α. An initial investigation of the behaviour of α was made by calculating the Ernst angle. This is the angle at which the signal is the maximum attainable for static tissue and it is expected to be ~17^0 i.e. $\cos^{-1}(e^{-TR/T_1})$ [38] for a TR of 50 ms and a T_1 of 1155 ms. Experimentally this angle was obtained from a plot of the boundary signal vs. α for a static image (see fig 5.5). This plot shows a maximum at 40^0, which was significantly higher than expected.

The discrepancy between the theoretically expected and the experimentally obtained Ernst angle can be explained from the behaviour of the steady state magnetization. The rf pulse is a truncated sinc function containing a bandwidth of exciting frequencies which if $TR << T_1$ results in the signal from the slice edge attaining a steady state magnetization that is different from that at the slice centre [38, 42]. Spins at the centre of the slice see the nominal α, whereas spins located outward from the centre experience a lower angle. When $\alpha > \alpha_{Ernst}$, spins at the slice edge

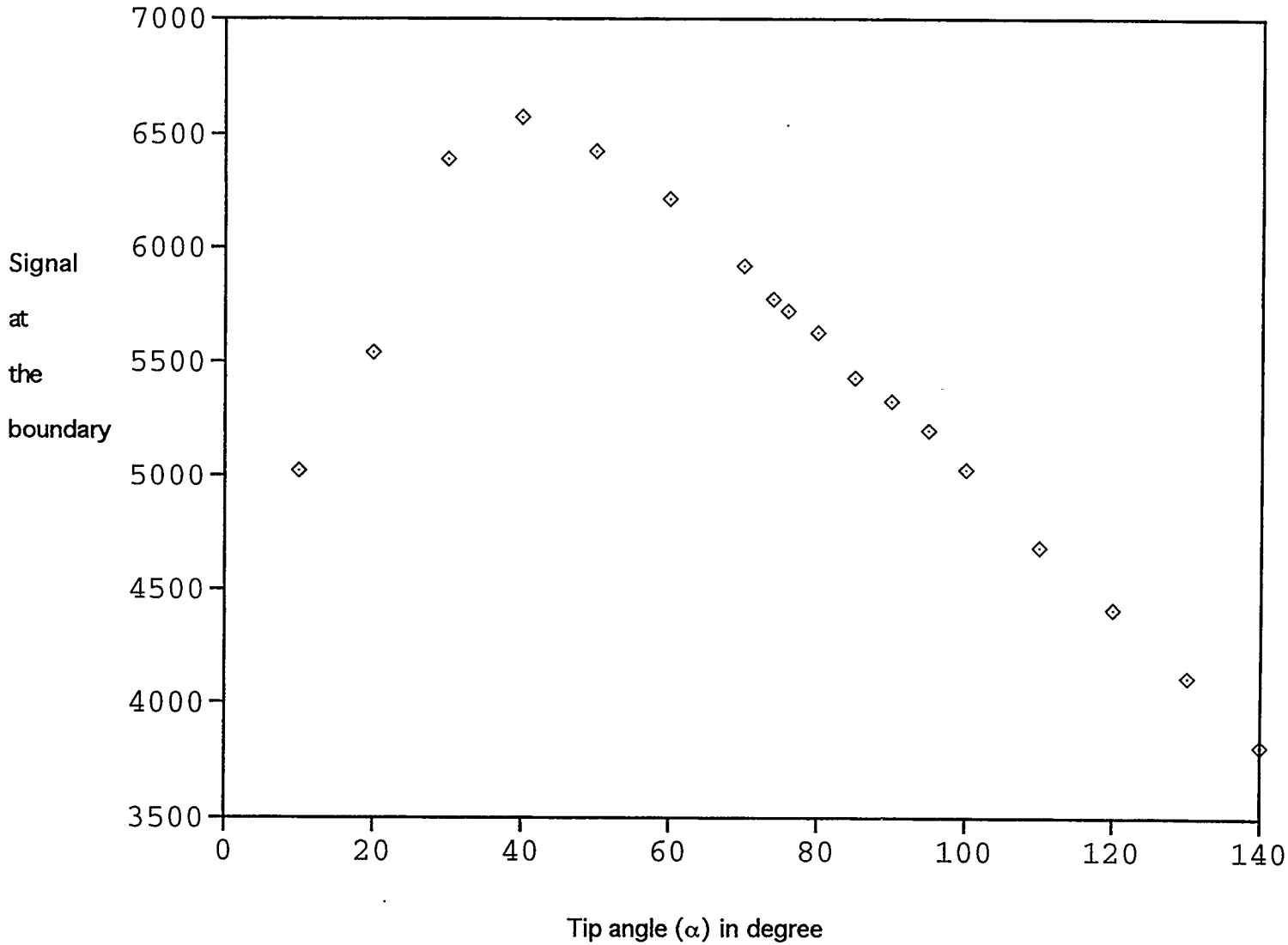

Figure 5.5 The static edge ROI signal vs. Tip angle from experimental data.

experience the Ernst angle therefore contributing most of the slice signal (see fig. 5.6).

Shown on fig. 5.7 are the computer simulated plots of the optimal tip angle (α_{opt}) vs. average velocity. As $v \rightarrow 0$ the PC plots tend to the Ernst angle, which is as expected, since the largest contribution to the contrast is obtained from the saturated blood signal, i.e. the A term of eq. 4.9 which also corresponds to the static tissue signal (section 4.2.1). In the region ($0 < v < 4$ cm/s) TOF required the largest angle as the contrast relies on a compromise between the desire to saturate the static tissue signal which requires a large tip angle and the need to minimize the saturation of slowly moving blood. As the velocity increased, α_{opt} also increased for all three methods indicative of the increasing TOF effect. The α_{opt} plot shows asymptotic behaviour as the velocity increases, since the TOF effect approaches maximum spin refreshment. Overall at low velocities CS has the lowest α_{opt}, whereas at high velocities TOF has the lowest relative to the other methods. PS required the largest α_{opt} for all velocities except in the range of 0-4 cm/s. The difference in α_{opt} between TOF and CS decreased as v increased to with a 3^0 range, while that for PS was generally about 10^0 higher than that for TOF. The tendency of α_{opt} towards a tip angle of approximately 90^0 as velocity increased was expected as the largest signal occurs if most of the magnetization is in the xy plane.

The experimental α_{opt} obtained is a poor quantitative fit to the simulated data. The poorest fit occurred in the low velocity region, while a better fit was observed in the upper range of the velocity ($v > 30$ cm/s). In this region the optimal experimental tip angle was determined to be around 112^0 for TOF, 115^0 for CS and 118^0 for PS. The disagreement between experimental and theoretical results can be accounted for by the steady state effect on the slice profile. Since an "anomalously" high nominal tip angle can produce an overall effect (averaged across the slice) similar to that of the Ernst angle, it is not surprising that this discrepancy in these results is found to have a negligible effect on the CNR results themselves.

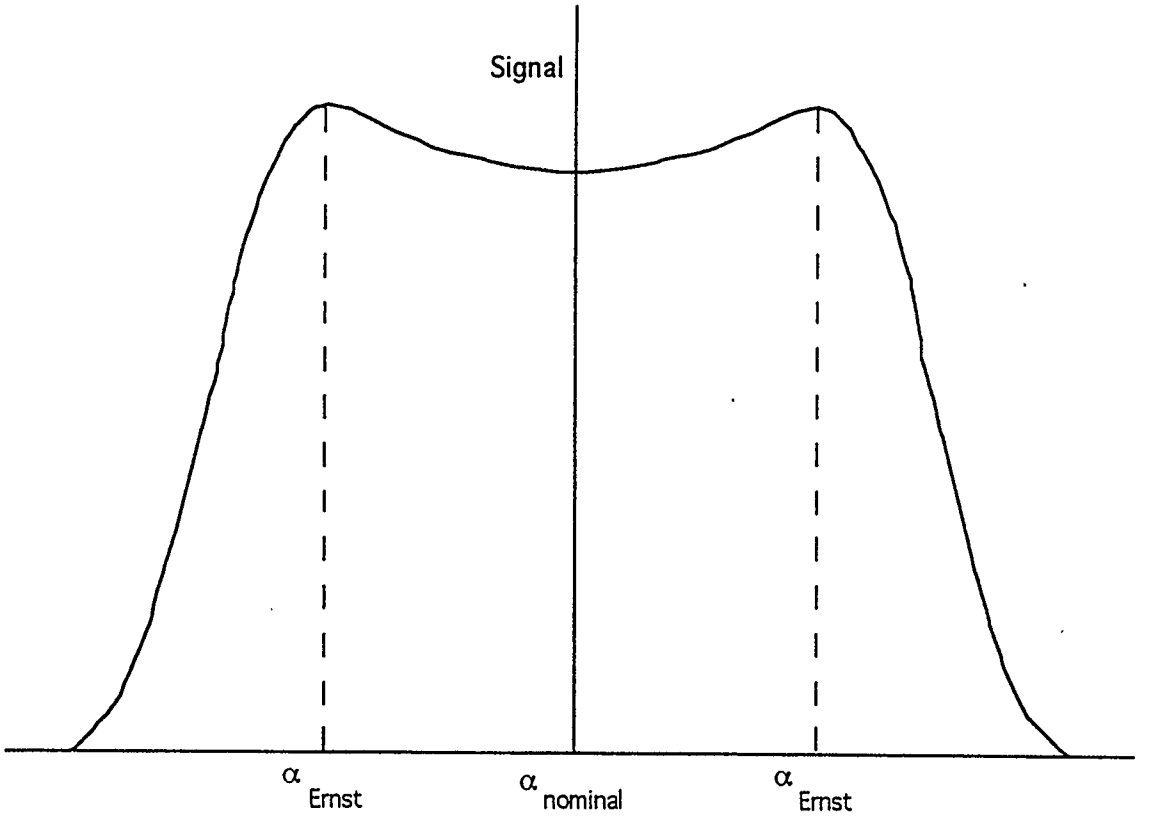

Figure 5.6 Effect of the tip angle on the slice profile. The effective α that spins at the slice edge experience is different from those at the centre. This results in the spins at the edges attaining a steady state magnetization that is different from those at the centre. When the nominal tip angle is greater than the Ernst angle, some spins near the edges experience the Ernst angle. At that time the largest signal contributions will be obtained from spins that are experiencing the Ernst angle.

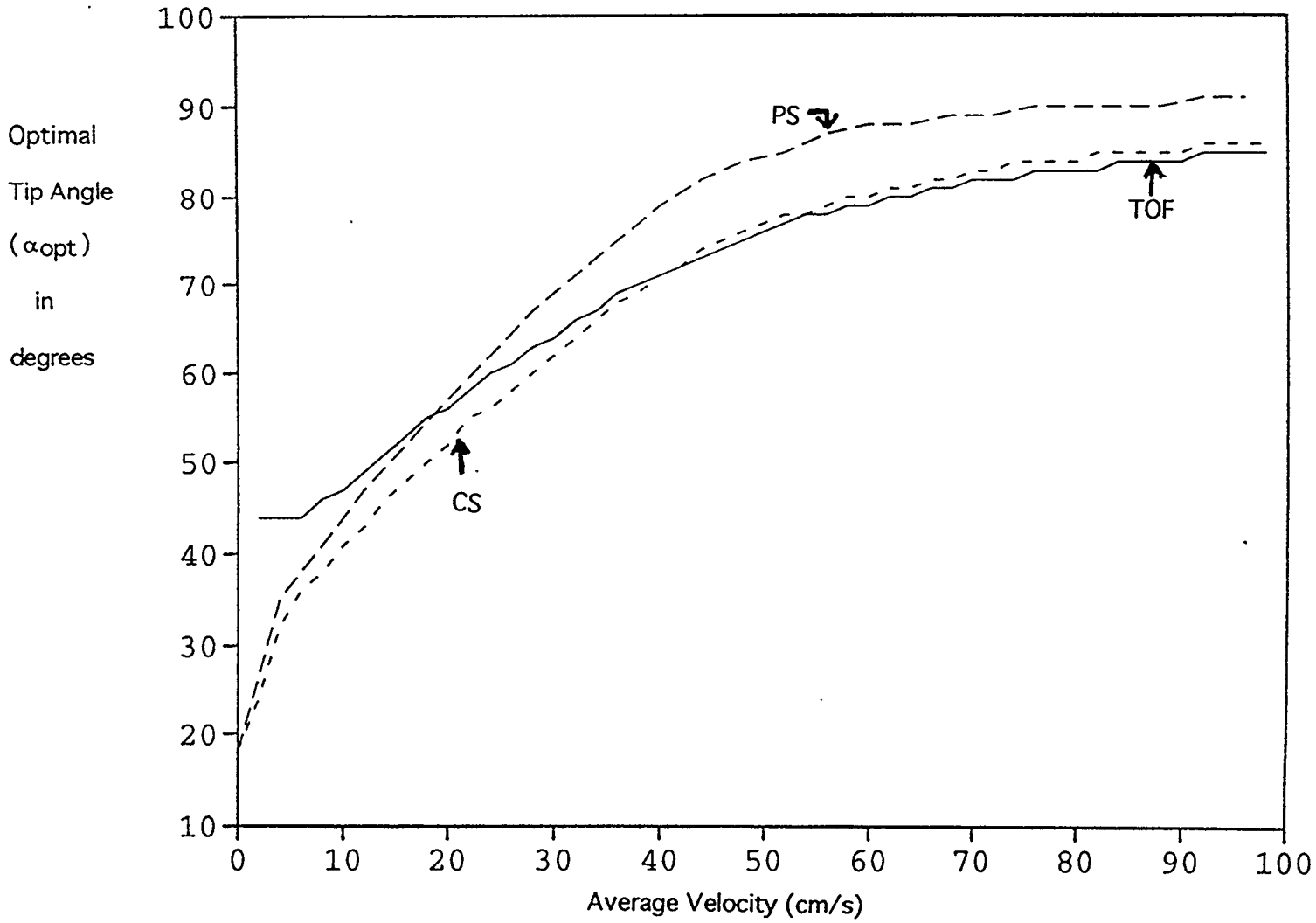

Figure 5.7 The plot shows the behaviour of α_{opt} vs. average velocity for the computer simulations.

The error in α due to random noise in the contrast measurements of fig. 5.8 was estimated to be $\pm 5^0$. However due to the steady state effect this error estimate does not reflect the actual error present. It was observed that for PS the peak becomes wider as velocity decreased. Though less noticeable a similar trend is seen for the other two methods with the peaks on the TOF being the most defined. The presence of the broad peaks implied that an error in the tip angle would contribute a relatively small error to the CNR.

Experimentally PS required the largest α_{opt} of the three techniques in concurrence with the simulated data. As the velocity increased the difference in α_{opt} among the three techniques decreased, again in agreement with simulations.

5.4.2 Optimal Flow Encoding Gradient

In the optimization of the flow encoding gradient, only the range of flow phase from 0^0 to 360^0 was investigated, where the phase quoted corresponds to that imparted to the peak flow velocity (see eq. 5.1). For a peak velocity phase of 360^0 the maximum flow phase that can be accrued by a spin in an edge voxel is approximately 130^0. It is expected that before this flow phase is attained, the dominant effect of the flow encoding gradient would be intravoxel dephasing causing a decrease in the signal. Additionally the contrast for CS is proportional to sin ϕ which reaches a maximum at 90^0. For the PS, an imparted velocity phase shift exceeding $\pm 180^0$ would cause phase wraps in the image. For example, a phase shift of 370^0 becomes indistinguishable form that produced by a shift of 10^0. This results in an apparent loss of the linear relationship between the phase and the velocity and makes image reconstruction difficult due to the need for phase unwrapping.

In the range of 0^0 - 360^0, no phase wraps in the edge voxels were expected in the phase image. However, phase wraps were present due to spatially varying phase offsets

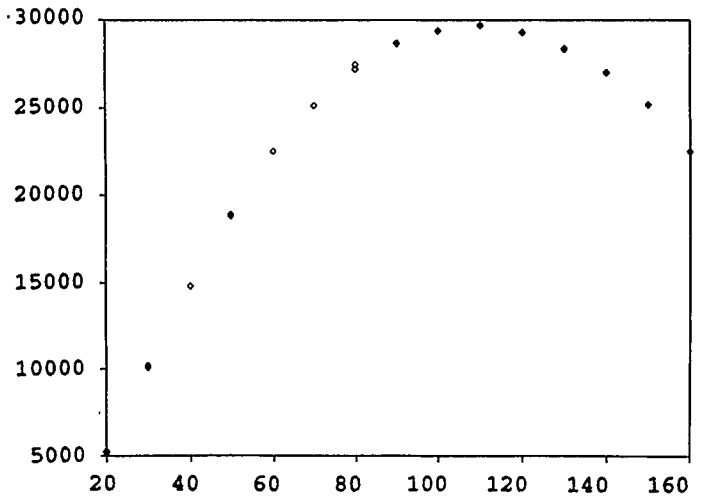

Figure 5.8

Plots of Contrast vs. Tip angle (α) in degrees for the experimental data for three average velocities.

A. TOF v = 44cm/s

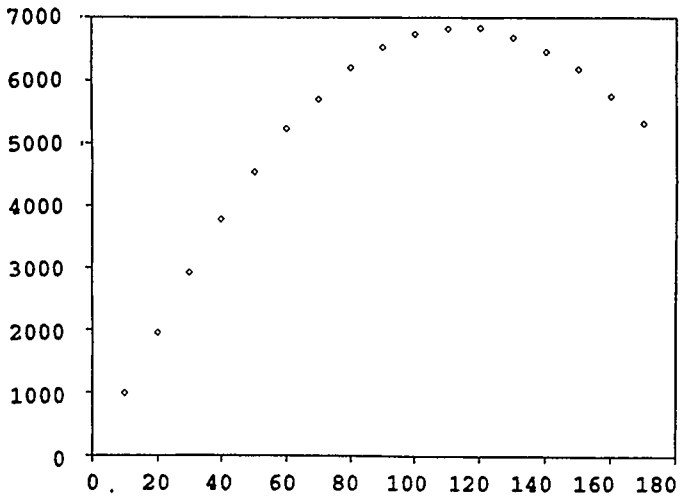

B. CS v = 26 cm/s

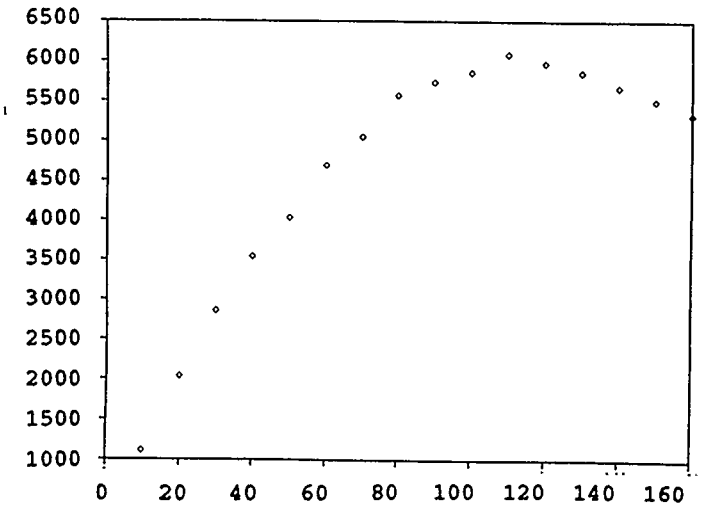

C. PS v = 12 cm/s

caused by field inhomogeneity effects and to the echo not being perfectly centered. This is very apparent on a static object in the image. In the flow images, this offset phase was added to that imparted by the flow encode gradient, which caused phase wrapping, producing erroneous results when subtraction was performed. This phase function varies smoothly across objects in the image, but was temporally unpredictable as the phase drifted in consecutive acquisitions.

To cancel the effect of the drift, the phase in each pixel from a flow and static data set was calculated. A portion of the imaged bottle was chosen that did not contain any phase wraps and a subtraction of corresponding pixel angles was done. The results were averaged and this average angle was then used to rotate the data in the static image, so that the phase of the bottle matched in both data sets after reconstruction. At this point the phase offset of the inflow tube on both images was approximately equal.

To remove the phase offset in the edge voxels, each pixel in the flow data is rotated, using an angle or rotation obtained from the phase of the corresponding pixel in the static image. The magnitude weighted phase difference image was then obtained.

The plot of optimal flow-encoded phase ϕ_{opt} vs. average velocity for the simulated data is shown in fig. 5.9. Here it is seen that PS requires a significantly larger ϕ_{opt} than does the CS method. The mean ϕ_{opt} from the simulated data was ~338^0 for PS and ~205^0 for CS. Experimentally for CS the mean ϕ_{opt} over the velocity range was 150^0 ± 17^0 and for PS it was found to be 310^0 ±18^0, where 17^0 and 18^0 degrees is the spread in ϕ_{opt} obtained over the velocity range. As the trend in the experimental data is consistent with the simulated data but the values are lower, the presence of systematic errors in the experiment is suspected.

Systematic errors can be attributed to the decreased ROI used to overcome phase instability at the edge of the tube. This would not affect the overall results because the phase was observed to be parabolic across the rest of the tube.

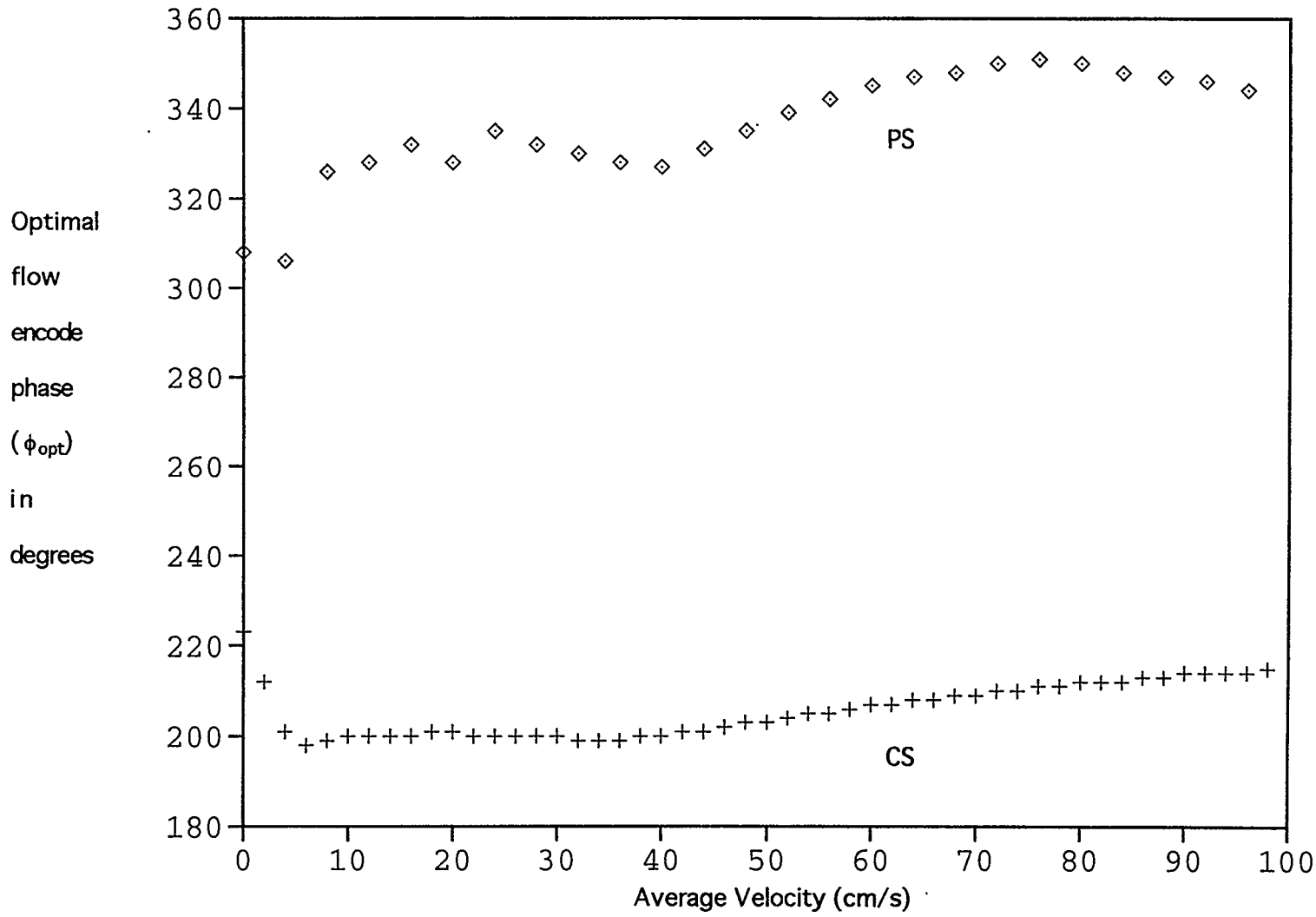

Figure 5.9 The plot shows the optimal flow encode phase ϕ_{opt} for optimal boundary contrast, for the computer simulations.

Fig 5.10a shows how the contrast varies with ϕ for an average velocity of 81 cm/s and $\alpha = 115^0$ for CS. This plot shows a relatively broad peak around $\phi = 150^0$. Fig. 10b shows a similar plot for PS which has a rise to a definable peak at $\phi = 310^0$, after which the graph appears to flatten out. The shapes of these graphs suggest that an error in ϕ would contribute a relatively small error in the CNR.

5.4.3 CNR

The simulated data shows that the contrast vs. average velocity for all three methods is fairly well behaved, i.e. varies smoothly over the velocity range (see fig. 5.11). CS performs better at low velocities ($0 < v < 15$ cm/s) compared to TOF. This is expected because the TOF method fails due to decreasing inflow effects as v->0. The CS method does not rely on inflow effects since it depends on flow phase encoding and the direct subtraction of the static tissue signal. A cross-over occurs at v=15 cm/s after which the TOF performs better than CS. As the velocity and hence the inflow of unsaturated spins increases, the CNR of the TOF method begins to improve. As the TOF effect approaches its maximum, the contrast approaches an asymptotic value. The PC methods also exhibit asymptotic behaviour, for the same reason Optimal contrast for CS, and for PS, occurs when the best compromise between intravoxel dephasing and maximal flow phase encoding is attained. The lower value of the asymptote for CS compared to TOF is due to intravoxel dephasing present in CS but not in TOF.

The best CNR at all velocities is achieved by PS. At v=98 cm/s the CNR attained by PS is 23% higher than TOF and 39% higher than CS. In an intermediate range ($v = 50$ cm/s) the difference is closer to 30% and 40% respectively, and this is the range of velocities for which the difference is the greatest. In the very important low velocity range ($5 < v < 10$ cm/s) PS out performs CS by 12% at $v = 5$ cm/s and closer to 20% at $v = 10$ cm/s.

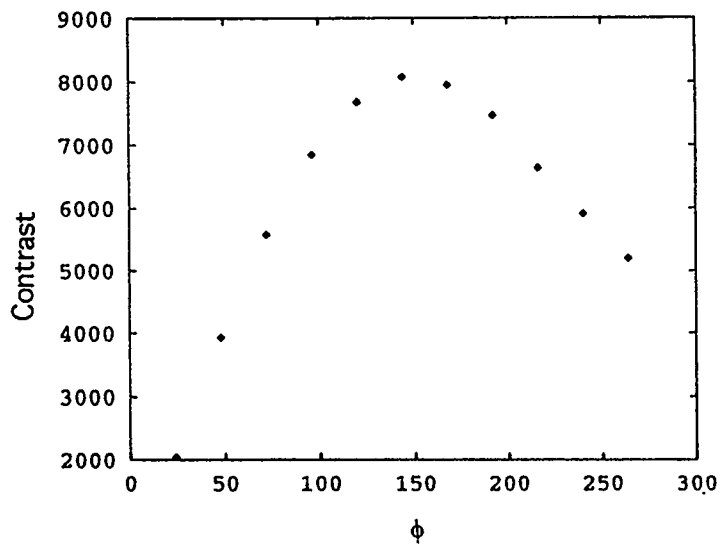

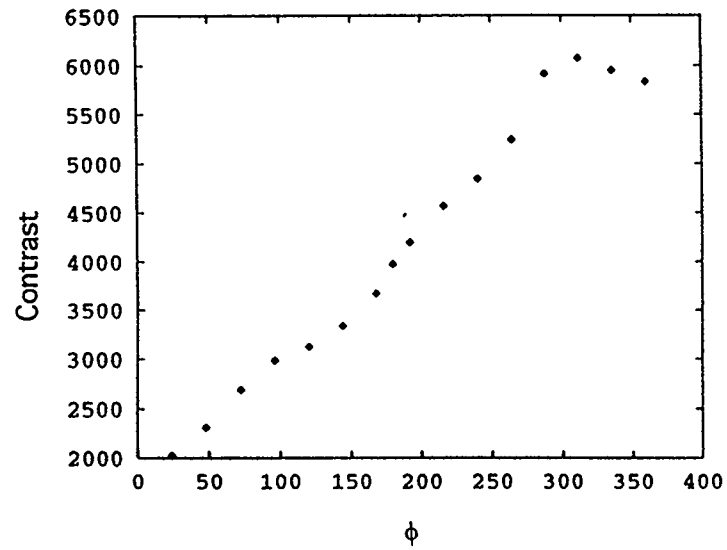

Figure 5.10a

Plot of contrast vs. flow encoded phase (ϕ) for $\alpha = 115^0$ and average velocity = 81 cm/s for CS. Plot obtained from experimental data.

Figure 5.10b

Plot of contrast vs. flow encoded phase (ϕ) for $\alpha = 118^0$ and average velocity = 12 cm/s for PS. Plot obtained from experimental data.

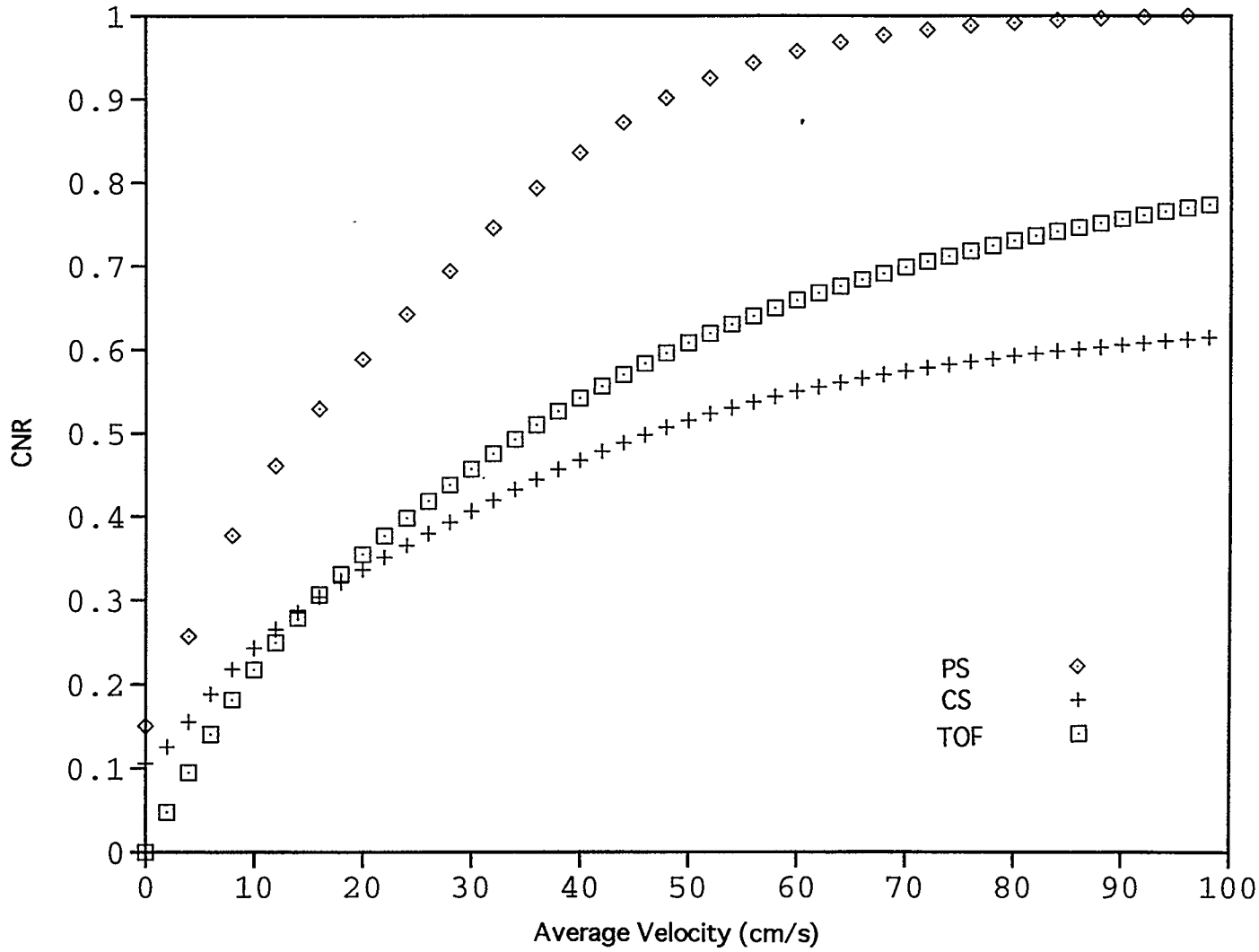

Figure 5.11 The simulated optimal CNR vs. average velocity.

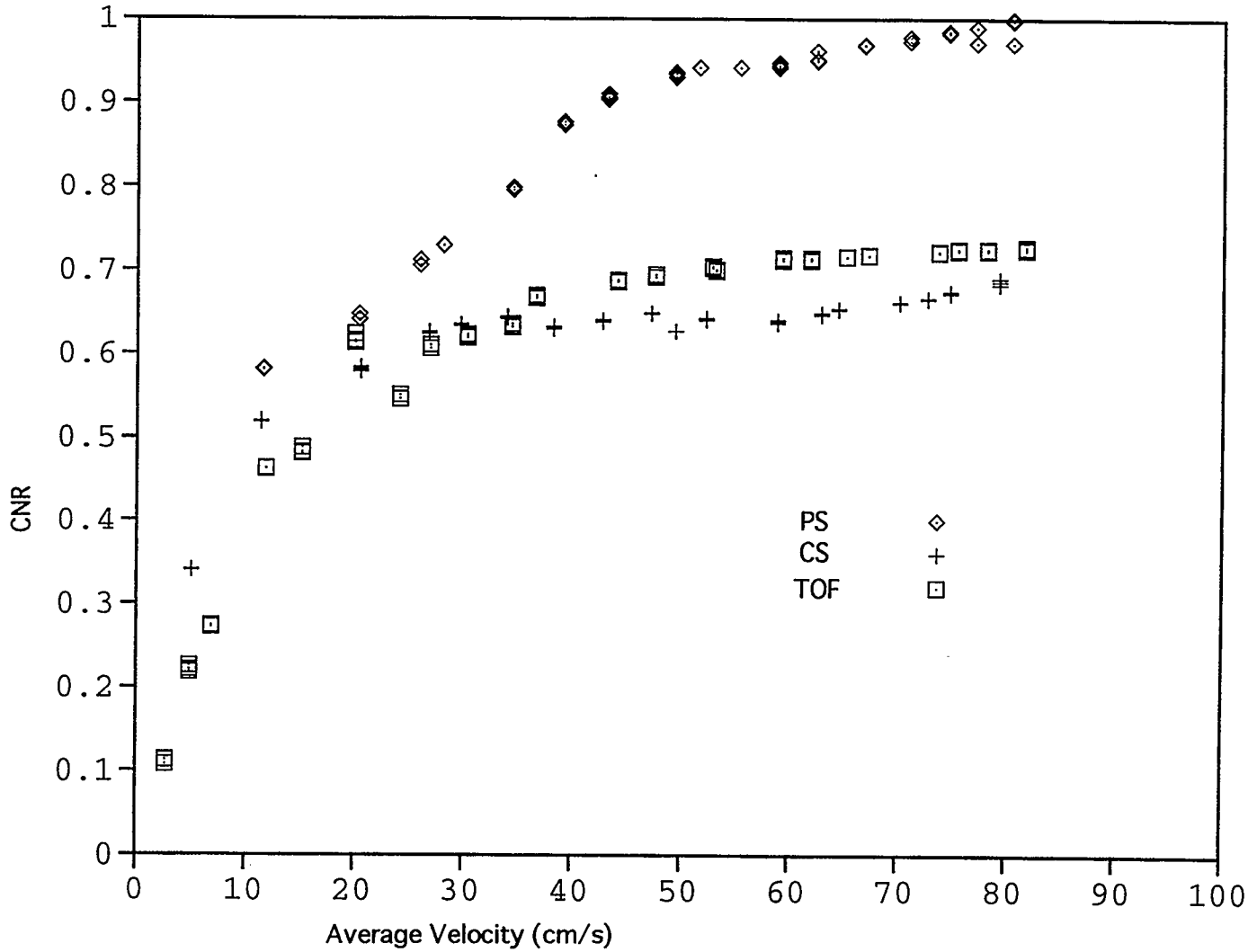

Figure 5.12 Plot of experimental CNR vs. average velocity.

The same trends were observed in the experimental results. On fig 5.12 a plot of CNR vs. average velocity for the three techniques is shown. CS performs better at low velocities with the cross over point occurring in the region $15 < v < 30$ cm/s. The points of the TOF graphs around this region appear very scattered, attributed to the presence of air bubbles (section 5.5). The lowest average velocity that could be examined for CS was $v \sim 5$ cm/s and for PS ~ 11 cm/s for the TE chosen (section 5.2) which was considered sufficient for the comparison of experimental data to the simulated data.

Overall agreement between the experimental and simulated data for the CNR is quite good despite the systematic error in the experimental ϕ_{opt} used, and the disagreement between the α_{opt} calculated in the simulations to those values obtained experimentally. Given the nature of the systematic errors, the use of the experimentally determined values of α_{opt} and ϕ_{opt} to obtain the optimal CNR vs. velocity data ensured good agreement with these results and the simulation.

5.5 Problems in Experimental Procedure

The major experimental problem was the presences of air bubbles that tended to cling to the sides of the tube in the ROI. If they were present at the imaged site, they caused susceptibility artifacts which were sometimes visible on the image. Bubbles were less of a problem for TOF as the run could be canceled as soon as they were observed, since the images were viewed immediately after acquisition. This was not so for the PC images because reconstruction of the images was done on the Sun after the experimental run was finished. Bubbles present in the length of tubing used to develop laminar flow meant that the resultant flow profile was not precisely parabolic. Bubbles so placed were fairly stable making the results reproducible in the experimental run. From observations of the phase and SE images the resultant profile was one that was close to

parabolic with a skewed peak. Such a profile would fulfill the requirement of the flow at the vessel edge (section 4.1), resulting in data that match the expected trends but would likely be a poor fit to the simulated data. These problems were in addition to the obvious one of air bubbles moving through the imaged slice during scanning. Bubbles were found to be more of an issue during slow flow.

Unfortunately the use of gravity feed for these experiments readily allowed the introduction of air bubbles into the system. The reservoir contained about 6 litres of fluid, which meant that flow was stopped after each scan and the fluid manually replaced in the upper reservoir. It was found that bubbles could be introduced during this process. The use of a pump to move the fluid back to the upper reservoir was found to add air bubbles into the system.

The miscibility of the fluid was also an issue during slow/medium flow and PC imaging. If separation occurred in the fluid, the T_1 changed and this would affect the steady state attained. During PC imaging there were long stops to allow for data transfer to the Sun, during which separation could occur.

A solution to these problems is to have a closed system consisting of a pump and a fluid having the required relaxation rates but with no miscibility problems, and a means to accurately measuring the velocity. A computer controlled flow simulator (UHDC flow simulator; University Hospital Development Corporation, London, Ont.) produced for MR studies is a very promising solution. The first marketed prototype was tried for these experiments but it was found to have some mechanical problems. These were solved by the manufacturers. However continued trials with it showed another problem. Magnetic particles (the source of which is unknown) were found in the blood mimicking fluid supplied. The simulator was at that point rejected in favour of gravity flow.

It should be noted that the flow simulator has much to recommend it and would be a good solution for MR flow studies when the source of the particles is eliminated.

CHAPTER 6

CONCLUSIONS

The object of this thesis was to find the optimal CNR at the vessel boundary that can be achieved by the TOF and PC techniques. Results were obtained for a parabolic flow profile with flow perpendicular to the slice. It was found from computer simulations and confirmed by experiments that at high velocities TOF performed better than CS whereas at low velocities, the reverse was true. Overall the best contrast was obtained with PS. These results were as expected from the theory of the three methods, and have been quoted in the literature [38].

The optimal experimental tip angle was determined to be around 112^0 for TOF, 115^0 for CS and 118^0 for PS for the upper range of the velocity. A large optimal tip angle was expected because the maximum signal occurs when the component of the macroscopic magnetization in the xy plane is greatest. The mean optimal flow encoding phase for CS obtained from the experiments was $150^0 \pm 17^0$, while for PS it was $310^0 \pm 18^0$ for the peak velocity range of $2 < v < 81$ cm/s . The phase required by CS was also expected to be lower than that of PS from the theory. The experimental data were a poor fit to the simulated data although they kept the general trend. This is attributed to the steady state effect at the slice edge when $TR << T_1$.

The contribution of this study is a quantitative assessment of the performance of the three techniques when the CNR at the vessel boundary is optimized, as well as the phase and tip angle required to accomplish this. Although the results pertain to laminar flow, these values can be used as a guideline for in-vivo studies as the requirement of slow flow and a large velocity gradient at the boundary voxel have been met. A criticism of this study is that it was not performed for voxels that included both static and flow tissue. However studies done by Bernstein and Ikezaki, 1991 [6] compared the

performance of CS to that of PS suggest that PS is still the superior technique. More importantly however, the agreement of the computer simulation CNR results to that obtained experimentally implies that the computer simulations can be used to theoretically assess other pulse sequences or flow profiles with the expectation that the results would be confirmed experimentally.

The PC techniques require a prior knowledge of the velocity distribution. If this is not known, PS is the most heavily penalized and performs badly. This is seen on fig. 6.1 where plots of the CNR generated from the computer simulations are shown for a 50% over-estimation (fig. 6.1a) and a 50% under-estimation (fig. 6.1b) of the average velocity. It is noted from the plots that PS performs worse if the velocity is under-estimated. The best choice if the velocity is not known appears to be the TOF.

The general implications of the results obtained in this study may be applied to any vessel geometry including a tortuous vessel in the imaging plane. For such vessels the TOF effect would depend on the total time spent in the imaged slice which would be very similar to that for slow flow in the perpendicular geometry. In PC methods the flow encoding gradients are usually placed along the direction of the orthogonal components of the velocity.

6.1 3D Comparison

The results obtained are for a 2D slice. The comparison for 3D acquisitions can be inferred directly from these results by considering the "scaling" of the slice thickness. Consider a 3D study of 20 slices (each of 1 mm thickness) with an average velocity of 40 cm/s, this could be viewed as similar to a 5 mm thick 2D slice with a 10 cm/s average velocity. Looked at in this manner the 2D results would give the average CNR over the 3D slab.

It is expected that 3D PC would perform better than 3D TOF as the inflow effects

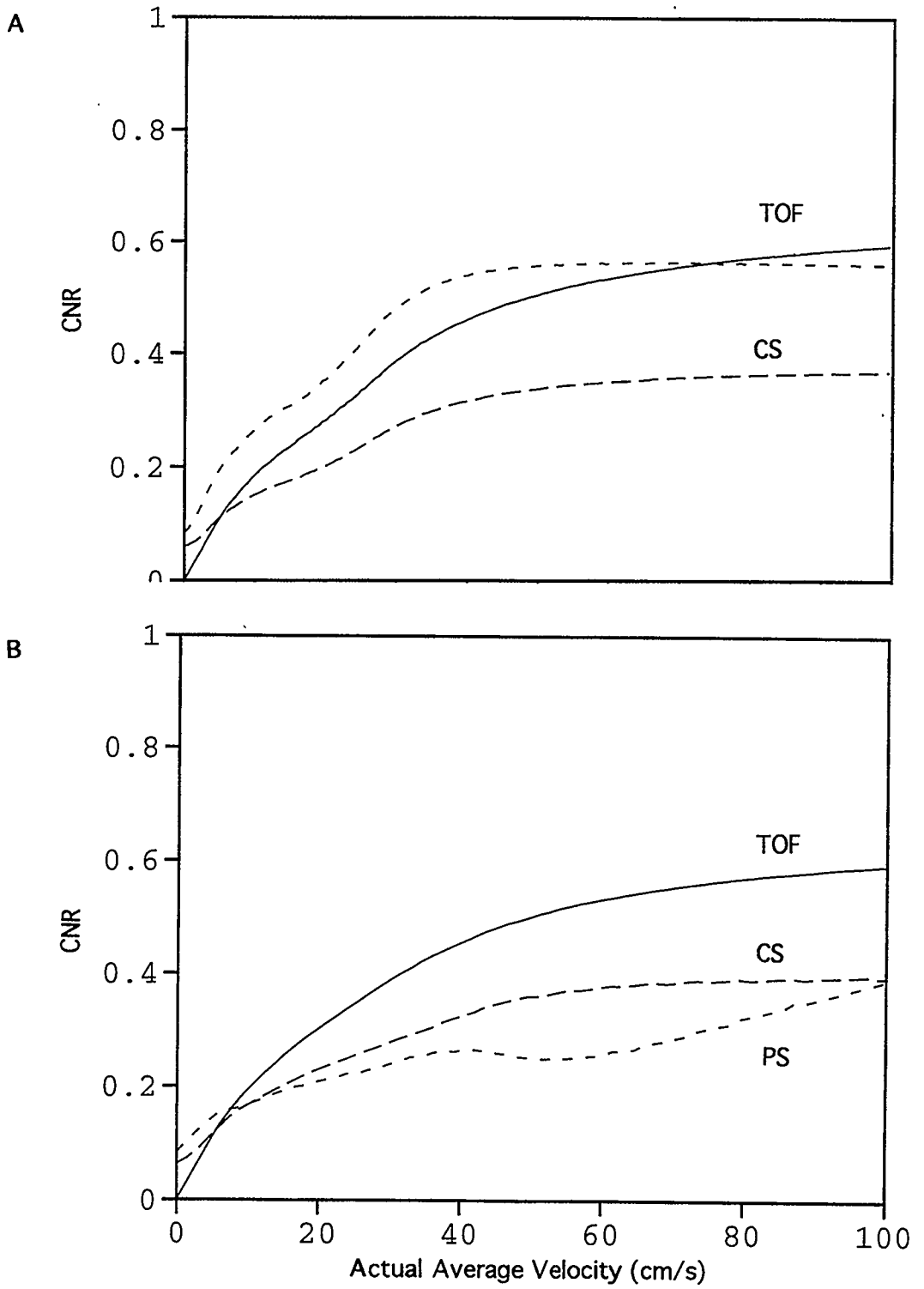

Figure 6.1 A. This plot show the simulated CNR obtained for TOF, CS and PS if the peak velocity is over-estimated by 50% vs. the actual velocity present.

B. This shows the CNR results if the velocity was 50% under-estimated.

decrease for slices further away from the first. PS would still perform best if the velocity distribution was known. Extension of the 2D computer simulations to 3D have confirmed these results.

6.2 Magnetization Transfer

The performance of TOF can be improved by the utilization of magnetization transfer contrast (MTC) [15, 30, 38, 42]. Any heterogeneous system possessing macromolecules in aqueous solution has two pools of protons, one that is free or mobile (H_f) while the other is bound (H_b). The T_2 of these two pools varies greatly (see fig. 2. 4); the intrinsic T_2 of H_f is relatively long (> 10 ms) while that of H_b is very short (<< 1 ms). Hence the resonance peak of H_f is relatively sharp in contrast to the very broad peak of H_b. This means that on a standard GRE sequence H_b is not directly visible on the image, however interactions between the two pools occur via chemical exchange and coupled relaxation. If the magnetization of H_b is saturated, prior to the GRE, by the application of an off resonance pulse with a frequency offset greater than 2 kHz, there is a decrease in the signal from H_f.

Blood contains a lower concentration of macromolecules compared to tissue, therefore it is less affected by magnetization transfer (MT) in comparison to brain tissue. Hence, the addition of a MTC pulse applied with the TOF sequence will result in an overall increase in the CNR even at low velocities as the signal suppression from the static tissue is improved. The contrast increases with the strength of the off resonance rf, which for in-vivo imaging is limited by safety regulations on the deposited power to the tissue. Edelman et al, 1993 [15] showed an improvement of about 12% in the CNR between arterial vessels and brain tissue.

6.3 Hybrid MRA technique

The results suggest that a combination of the TOF and the PC methods would be best suited for in-vivo imaging where the flow velocity may vary over a wide range in the image. This would take advantage of the PC effect in regions of slow flow while exploiting the TOF effect in regions where intravoxel dephasing due to the flow phase encoding gradient would be severe.

Another look at the unbalanced four point method for PC [21, 36] discussed in chapter 3 shows that this method with its on/off flow encoding gradients is an example of a hybrid sequence. The reference acquisition obtained when the bipolar is off is simply a TOF method, while the other three acquisitions have the bipolar gradient on, during which flow phase encoding occurs. The images can be processed to obtain the PS image, the CS image, a magnitude image equivalent to TOF or any combination of the three.

As the velocity varies between blood vessels and a knowledge of the velocity distribution is generally not known, the PC method would have to be implemented with a range of flow-encoding gradient strength to maximize the contrast between blood and tissue. However the efficiency of this method still has to be determined. Incrementing the flow encode gradient strength to Fourier encode the velocity spectrum is one way of obtaining the contrast between flow and static tissue, however this is not designed to maximize the CNR efficiency.

6.4 Summary

PS has the best CNR at all velocities at the vessel boundary, hence it is the optimal technique for vessel detection. The images are quantitative as the phase shift accrued is directly proportional to the velocity, with the possibility of obtaining directional information which can improve the knowledge of the physiology involved. Its

disadvantages include the increased scan time required (relative to TOF), and the necessity of prior knowledge of the velocity distribution as well as the need for robust phase unwrapping. The large gradient power required to flow encode slow flow in the PC method presents a problem as the maximum gradient amplitude is limited by the hardware, while the time duration of the gradient is restricted by the TE used in the pulse sequence. The TE is required to be as short as possible to minimize signal decay due to T_2^* (section 4.2.1). The presences of gradient eddy currents can affect the phase stability and complete subtraction of static tissue may not be achieved.

The static tissue is also directly subtracted out in CS and its requirement of a lower flow encoding phase compared to PS is an advantage if slow flow is present.

The TOF method has the advantage of lower scan times since it does not rely on flow encoding. There is also significantly less need for prior knowledge of the velocity distribution, hence of the three it is the most robust method. However the static tissue is not directly subtracted out and with slow flow the TOF effect is minimal. The addition of MTC can improve the contrast obtained, but slow flow will still be a problem.

6.5 Future work

This study has shown that the computer model used is good enough to assess the effect of the TOF and PC methods. The computer simulation will be improved by simulating the steady state effect on the slice profile. Magnetization transfer will then be added by incorporating the static tissue attenuation that has been measured experimentally [15]. The focus on future work would then be to utilize the simulations to examine some of the proposed sequences [38] in MRA for e.g. the hybrid MRA technique. A first step towards this would be to simulate the results for velocities with non-zero components in the three Cartesian directions, thereby quantitatively assessing a more general situation.

REFERENCES

1. Abragam, A., The Principles of Nuclear Magnetism, Oxford University Press, Oxford, 1961.
2. Ackerman, R., M. Candia, Identifying Clinically Relevant Carotid Disease, Stroke, Volume 25: 1-3, 1994.
3. Anderson, C.M., D. Saloner, J.S. Tsuruda, L.G. Shapeero, R.E. Lee, Artifacts in Maximum-Intensity-Projection Display of MR Angiograms, AJR., Volume 154: 623-629, 1990.
4. Applegate, G.R., S.L. Talagala, L.J. Applegate, MR Angiography of the Head and Neck: Value of Two-Dimensional Phase-Contrast Projection Technique, AJR., Volume 159: 159-374, 1992.
5. Axel, L., Blood Flow Effects in Magnetic Resonance Imaging, AJR., Volume 143: 1157-1165, 1984.
6. Bernstein, M.A., Y. Ikezaki, Comparison of Phase-Difference and Complex-Difference Processing in Phase-Contrast MR Angiography, JMRI., Volume 1: 725-729, 1991.
7. Bogdahn, U., G.Becker, J. Winkler, K. Greiner, J. Perez, B. Meurers, Transcranial Color-Coded Real-time Ultasonography in Adults, Stroke, Volume 21: 1680-1688, 1990.
8. Brown, D.G., S.J. Reiderer, Contrast-to-Noise Ratios in Maximum Intensity Projection Images, Magn. Reson. Med., Volume 23: 130-137, 1992.
9. Conturo, T.E., G.D. Smith, Signal-to-Noise in Angle Reconstruciton: Dynamic Range Extension Using Phase Reference Offsets, Magn. Reson. Med., Volume 15: 420-437, 1990.

10. Digital Subtraction Angiography in Clinical Practice, published by Philips Medical Systems, Best, The Netherlands, 1986.

11. Dixon, R.L., K.E. Ekstrand, The Physics of Proton NMR, Med. Phys., Volume 9: 807-818, 1982.

12. Dumoulin, C.L., S.P. Souza, R.D. Darrow, N.J. Pelc, W.T. Adams, S.A. Ash, Simultaneous Acquisition of Phase-Contrast Angiograms and Stationary-Tissue Images with Hadamard Encoding of Flow-Induced Phase Shifts, JMRI., Volume 1: 399-404, 1991.

13. Dumoulin, C.L., S.P. Souza, M.F. Walker, E. Yoshitome, Time-Resolved Magnetic Resonance Angiography, Magn. Reson. Med., Volume 6: 275-286, 1988.

14. Edelman, R.R., MR Angiography: Present and Future, AJR., Volume 161: 1-11, 1993.

15. Edelman, R.R., S.S. Ahn, D.Chein, W. Lei, A. Goldman, M. Mantello, J. Kramer, J. Kleefield, Improved Time-of-Flight MR Angiography of the Brain and Magnetization Transfer Contrast, Radiology, Volume 184: 395-399, 1993.

16. Edelman, R.R., D. Chein, D. Kim, Fast Selective Black Blood Imaging, Radiology, Volume 181: 655-660, 1991.

17. Edelman, R.R., J.R. Hessellink, MRI, Clinical Magnetic Resonance Imaging, W.B. Saunders Company, St. Louis, Missouri, 1990.

18. Edelman, R.R., H.P. Mattle, B. Wallner, R. Bajakian, J. Kleefield, C. Kent, J. Skillman, J. Mendel, D. Atkinson, Extracranial Carotid Arteries: Evalulation with "Black Blood" MR Angiography, Radiology, Volume 177: 45-50, 1990.

19. Edelman, R.R., B.Siewert, M. Adamis, J. Gaa, G. Laub, P. Wielopolski, Signal Targeting with Alternating Radiofrequency (STAR) Sequences: Application to MR Angiography, Magn. Reson. Med., Volume 31: 233-238, 1994.

20. Farrar, T.C., E.D. Becker, Pulse and Fourier Transform NMR, Academic Press, New York, San Francisco, London, 1971.

21. Hausmann, R., J.S. Lewin, G. Laub, Phase-Contrast MR Angiography with Reduced Acquisition Time: New Concepts in Sequence Design, JMRI., Volume 1: 415-422, 1991.

22. Heiserman, J.E., B.P. Drayer, P.J. Keller, E.K. Fram, Intracranial Vascular Stenosis and Occlusion: Evaluation with Three-dimensional Time-of-Flight MR Angiography, Radiology, Volume 181: 721-730, 1991.

23. Huston, J. III, B.D. Lewis, D.O. Wiebers, F.B. Meyer, S. Riederer, A. Weaver, Carotid Artery: Prospective Blinded Comparison of Two-dimensional Time-of-Flight MR Angiography with Conventional Angiography and Duplex US Radiology, Volume 186: 339-334, 1993.

24. Huston, J. III, D. Rufenacht, R.L. Ehman, D.O. Wiebers, Intracranial Aneurysms and Vascular Malformations: Comparison of Time-of-Flight and Phase-Contrast MR Angiography, Radiology, Volume 181: 721-730, 1991.

25. Johnsrude, I.S., D.C. Jackson, R.N. Dunnick, A Practical Approach to Angiography 2nd Ed., Little, Brown and Company (Inc.), Boston, Toronto1987.

26. Keller, P., B. Drayer, E. Fram, K. Williams, C.L. Dumoulin, S.P. Souza, MR Angiography with Two-Dimensional Acquisition and Three-Dimensional Display works-in-progress, Radiology, Volume 173: 527-532, 1989.

27. King, K.F., P.R. Moran, A Unified Description of NMR Imaging, Data-Collection Strategies and Reconstruction, Med. Phys., Volume 11: 1-12, 1984.

28. Lewin, J.S., G. Laub, Intracranial MR Angiography: A Direct Comparison of Three Time-of-Flight Techniques, AJNR., Volume 12: 1133-1139, 1992.

29. Lin, W., E.M. Haacke, T.J. Masaryk, A.S. Smith, Automated Local Maximum-Intensity Projection with Three-Dimensional Vessel Tracking, JMRI., Volume 2: 519-526, 1992.

30. Lin, W., J.A. Tkach, M.E. Haake, T.J. Masaryk, Intracranial MR Angiography: Application of Magnetization Transfer Contrast and Fat Saturation to Short Gradient Echo, Velocity-Compensated Sequences, Radiology, Volume 186: 753-761, 1993.

31. Litt, A.W., E.M. Eidelman, R.S. Pinto, T.S. Riles, S.J. McLachlan, S. Schwartzenberg, J. Weinreb, I.I. Kricheff, Diagnosis of Carotid Artery Stenosis: Comparison of 2DFT Time-of-Flight MR Angiography with Contrast Angiography in 50 Patients, AJNR., Volume 12, 1991.

32. Marks, M.P., S. Napel, J.E. Jordan, D.R. Enzmann, Diagnosis of Carotid Artery Disease: Preliminary Experience with Maximum-Intensity-Projection Spiral CT Angiography, AJR., Volume 160: 1267-1271, 1993.

33. Mittl, R.L. Jr., M.M. Brocerick, J.P. Carpenter, H.I. Goldberg, J. Listerud, M. Mishkin, H. Berkowitz, S. Atlas, Blinded-Reader Comparison of Magnetic Resonance Angiography and Duplex Ultrasonography for Carotid Artery Bifurcation Stenosis, Stroke, Volume 25: 4-10, 1994.

34. Nishimura, D.G., A. Macovski, J.M. Pauly, S.M. Conolly, MR Angiography by Selective Inversion Recovery, Magn. Reson. Med., Volume 4: 193-202, 1987.

35. Parker, D.L., C. Yuan, D.D. Blatter, MR Angiography by Multiple Thin Slab 3D Acquisition, Magn. Reson. Med., Volume 17: 434-444, 1991.

36. Pelc, N.P., M.A. Berstein, A. Shimakawa, G.H. Glover, Encoding Strategies for Three-Direction Phase-Contrast MR Imaging of Flow, JMRI., Volume 1: 404-413, 1991.

37. Polak, J., R. Bajakian, D. O'Leary, M. Anderson, M. Donaldson, F. Jolesz, Detection of Internal Carotid Artery Stenosis: Comparison of MR Angiography, Color Doppler Sonography, and Arteriography, Radiology, Volume 182: 35-40, 1992.

38. Potchen, J.E., E.M. Haacke, J.E. Siebert, A. Sottschalk, Magnetic Resonance Angiography, Concepts and Applications, Mosby Year Book, St. Louis, Missouri, 1993.

39. Rankin, R.N., A. Fenster, D.B. Downey, P.L. Munk, M. Levin, A. Vellet, Three-Dimensional Sonographic Reconstruction: Techniques and Diagnostic Applications, AJR., Volume 161: 695-702, 1993.

40. Saloner, D., W.A. Hanson, J.S. Tsuruda, R. van Tyen, C.A. Anderson, R.E. Lee, Application of a Connected Voxel Algorithm to MR. Angiographic Data, JMRI., Volume 1: 423-430, 1991.

41. Spritzer, C.E., R.A. Binder, Vascular Applications of Magnetic Resonance Imaging, Magnetic Resonance Quarterly, Volume 5: 205-227, 1989.

42. Stark, D.D., W.J. Bradley JR., Magnetic Resonance Imaging Volume 1, Mosby Year Book, St. Louis, Missouri, 1992.

43. Talin, A.T., J.N. Lee, S.J. Reiderer, J.B. Decastro, L.W. Hedlund, R.J. Herfkens, C.E. Spritzer, Fast Limited Flip Angle MR Subtraction Angiography, Magn. Reson. Med., Volume 8: 261-274, 1988.

44. Taylor, K.J.W., P.N. Burns, P.N.T. Wells, Clinical Applications of Doppler Ultrasound, Raven Press, New York, 1988.

45. Vascular Magnetic Resonance Imaging, Signa Applications Guide Volumes 2 and 3, published by GE Medical Systems, Milwaukee, Wisconsin, U.S.A., 1990.

46. Wang, S., D. Mishimura, A. Macovski, Fast Angiography Using Selective Inversion Recovery, Magn. Reson. Med., Volume 23: 109-121, 1992.

47. Wolpert, S.M., L.R. Caplan, Current Role of Cerebral Angiography in the Diagnosis of Cerebrovascular Diseases, AJR., Volume 159: 191-197, 1992.

48. Zweibel, W.J., R. Knighton, Duplex Examination of the Carotid Arteries, Seminars in Ultrasound CT and MR, Volume 11: 97-135, 1990.

49. Zur, Y., X. Zou, L. Neuringer, MR Angiography without Subtraction, Mag. Reson. Med., Volume 19: 361-372, 1991.